Thesis for the degree of Doctor of Philosophy

Experimental characterization of respiratory droplet emission

Thesis in co-supervision between Sapienza Università di Roma and École Centrale de Lyon

Doctoral school of Ingegneria Idraulica e Ambientale and of Mécanique, Énergétique, Génie Civil, Acoustique

Thesis funded by Istituto nazionale Assicurazione Infortuni sul Lavoro (INAIL)

Candidate
Livia Grandoni

Supervisors
Paolo Monti
Pietro Salizzoni

INAIL Co-supervisor
Armando Pelliccioni

ECL Co-supervisor
Loïc Méès

Academic Year 2022-2023 (XXXV cycle)

"Of special importance is the following fact: the construction of models, like any genuine art, cannot be taught by reading books and/or journal articles. The reason is that in articles and especially in books the 'scaffolding' is removed, and the presentation of the results is shown not in the way that they were actually obtained but in a different, perhaps more elegant way. Therefore it is very difficult, if not impossible, to understand the real 'strings' of the work: how the author really came to certain results and how to learn to obtain results on your own" (Barenblatt, G., 2003, *Scaling*, Cambridge Texts in Applied Mathematics, Cambridge: Cambridge University Press)

Abstract

The droplet-laden air cloud exhaled by humans during different respiratory activities plays a major role in infectious disease transmission. That exhaled droplets contain pathogen is a well-known fact in the scientific community since the 19th Century. Unfortunately, pandemics as COVID-19, SARS, and MERS, have recently brought back the attention to this issue, which is rather complex since multiple-scale phenomena and different disciplines (epidemiology, biology, fluid mechanics) are involved. Fluid mechanics plays a major role in the comprehension of droplet-laden air cloud dynamics and mitigation of the related risks. Indeed, the pathogens interact with fluids from their encapsulation within the droplets in the airways to their inhalation by susceptible individuals. The prediction of the fate of the droplets after their emission have widely been improved, especially in the past three years, by means of experiments and models. However, a lack of knowledge of the air and droplet properties at the emission (mouth) emerges from the literature. Providing precise information on emission characteristics to numerical or theoretical models that predict droplet dispersion is of striking importance to obtain reliable results. The present thesis aims to contribute to this field by improving the characterization of droplet emission, namely, their size and velocity distribution. A series of laboratory experiments have been conducted considering different respiratory activities, namely, speaking, coughing and breathing. The Interferometric Laser Imaging for Droplet Sizing (ILIDS) technique has been used for data collection. Both the setup and the related data processing have been improved with respect to ILIDS standard applications in order to detect droplets with size down to 2 μm and to measure all their three velocity components. Two experimental campaigns involving twenty-three volunteers have been carried out. The effects of protection masks and the variability in the results obtained for the same volunteer repeating the tests are also assessed. Finally, droplet size and velocity distributions have been used as input data for Computational Fluid Dynamics simulations in order to analyse their role in the dispersion process following their emission.

Keywords: ILIDS, droplet sizing, droplet velocity, human emission, disease transmission, droplet dispersion, COVID-19.

Contents

List of Figures

List of Tables

Chapter 1

Introduction

The study of emission and dispersion of droplet-laden air cloud exhaled by humans during different respiratory activities is of major importance for the comprehension of infectious disease transmission (e.g., Qian et al. (2021)). Recent COVID-19 pandemic, along with the previous SARS and MERS pandemics, have brought back the attention of the scientific community on this problem with the aim to find risk mitigation strategies. It is worth to remember that other, unfortunately common, infectious diseases, such as seasonal influenza and tuberculosis, are also involved. Both of them highlighted the lack of knowledge that still exists on this theme, although discovered in the 19^{th} century.

In the second half of the 19^{th} century, the existence of microorganisms causing infectious diseases came to light thanks to the works of Pasteur and Koch. Only a few years later Flügge found out the presence of pathogens in the droplets exhaled by humans (Bourouiba, 2021). At the beginning, the droplets were only considered to either settle around the emitter person, contaminating surfaces and objects, or directly impinging susceptible individuals close to him. In the 1930s Wells (1934) stressed out the fact that the droplets undergo evaporation in addition to settling. Therefore, depending on their size, they could completely evaporate before settling, leaving in the air a solid residual possibly including pathogens, the so-called droplet-nuclei. Due to its small size, the droplet-nuclei is characterized by very low settling velocity, allowing for its transport at long distances from the emitter, even in the presence of weak ambient airflow. The possibility of airborne disease transmission is, then, enlightened. Only about eighty years later, the fundamental role of the dynamics of the airflow characterizing the region downward of the mouth/nose of a human was pointed out. The momentum and turbulence characteristics of the air cloud has been recognised to play a fundamental role in trapping droplets of all sizes and in transporting them at distances far greater than it would be predicted using Wells' approach (Bourouiba, 2020). An illustrative visualization of the complexity of the airflow produced by a sneeze is depicted in Figure 1.1 (Bourouiba, 2020). Droplet evaporation is also affected by the air cloud into which it is trapped, where higher temperature and relative humidity are present with respect to the ambient air. Furthermore, these quantities change while the air cloud disperses.

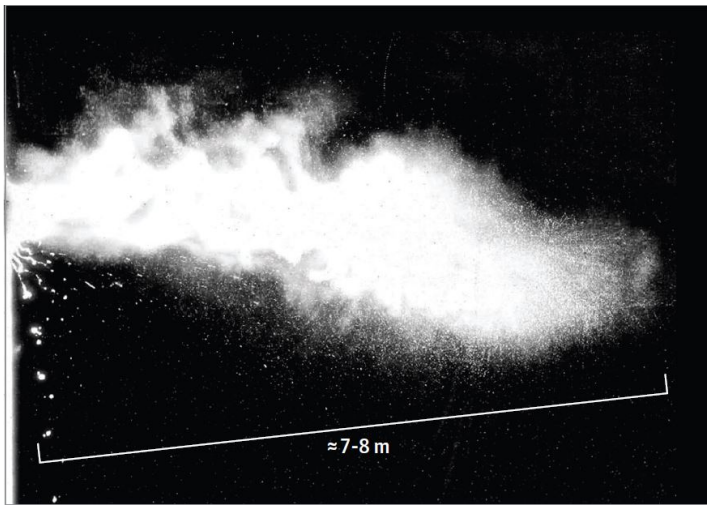

Figure 1.1: Visualization of a sneeze Bourouiba (2020).

Three infectious disease transmission mechanisms for which exhaled droplets are responsible can be identified, i.e., direct, airborne, or contact with fomites (WHO). Direct transmission is caused by ejected droplets that directly reach mucous membranes of a susceptible individual, which is in close contact with the emitter, e.g., at a conversational distance. Airborne transmission can be distinguished between close (or short-range) and distant (or long-range) airborne transmission (Seminara et al., 2020). In the case of close airborne transmission, the susceptible inhales droplets (partially or completely evaporated) present in the air. Note that this kind of transmission occurs close to the emitter where droplet concentrations are higher (Balachandar et al., 2020). The smallest droplets or the small droplet-nuclei formed after evaporation of larger droplets cause the distant airborne transmission. As mentioned earlier, due to the small sizes and low settling velocities, these droplets (or droplet-nuclei) are transported further by the ambient airflow potentially carrying pathogens with them. Thanks to dilution, the concentrations responsible for this kind of transmission are low. Furthermore, the risk is reduced in long-range airborne disease transmission due to possible virus inactivation. The probability of distant airborne transmission is higher in crowded and/or poorly ventilated indoor environments due to accumulation and poor dilution (e.g., Li et al. (2021)) . Therefore, considering airborne disease transmission in the more general evaluation of indoor air quality is of striking importance, especially since people spend most of their time in indoor settings (private houses, working and public places) (Pelliccioni et al., 2020). The authorities recognized the airborne – especially the distant airborne – as transmission mechanism of SARS-Cov-2 only lately (July 2020) (Bourouiba, 2021). This delay is ascribable to the difficulty in collecting and detecting pathogens in airborne droplets or droplet-nuclei (Lewis, 2020; Morawska and Cao, 2020). Pan et al. (2019) reviewed available sampling technologies for airborne respiratory viruses pointing out their limitations. Besides, epidemiological studies are not able to answer precisely to this question as large-scale data are considered where all the transmission mechanisms are possibly involved (Bourouiba, 2021). Finally, a susceptible individual can contract the infection by touching their mouth, nose or eyes after touching

fomites.

Note that direct and airborne transmission are also termed as "droplet" and "aerosol transmission" (WHO). However, in the present work the term droplet stands for liquid droplet, considering its general meaning.

The study of infectious disease transmission by exhaled droplets takes the form of a multidisciplinary problem (Asadi et al., 2020; Dbouk and Drikakis, 2020a). Epidemiologists are involved for the large-scale spread of the contagion. Physicians and biologists have the task of identifying viral load contained into the droplets coming from the respiratory tract, virus survival in the environment and the viral dose required to be infected. Fluid mechanics also plays an important role as pathogens interact with fluids, from the encapsulation and extraction from the airways to the emission and transport of the exhaled droplet-laden air cloud and, eventually, to the pathogen penetration into the respiratory apparatus of the susceptible individual (Bourouiba, 2021). Hence, the final goal of fluid mechanics in this field of study is generally twofold: to understand the characteristics of the emitted droplets in terms of size and velocity and to predict their trajectory.

1.1 Phenomenology and state of the art

Several real-scale and laboratory experiments, simple models and Computational Fluid Dynamics (CFD) simulations have been used to assess the fate of the droplets after the emission.

In his seminal work, Wells (1934) considered isolated droplets moving in still air. In particular, based on previous works about droplet evaporation and settling, he obtained an expression for the time taken by the droplets to settle at the ground and evaporate completely. The goal was to define a cut off size for droplets that remain airborne as droplet-nuclei. The square size of a water droplet evaporating at constant ambient temperature and relative humidity (RH) reduces linearly in time. For the settling, Newton's and Stokes' laws are considered. However, Wells (1934) did not take into account the fact that droplets are ejected into a cloud of moist warm air.

Xie et al. (2007) revised the work by Wells (1934) considering the air cloud surrounding the droplets. Namely, they modelled the exhaled airflow as a turbulent stationary jet and used well-known theories to determine the trajectory, the temperature, and both the axial and radial velocity of the air jet. The motion of droplets of various sizes is predicted by solving the momentum balance equation for each of them and considering the reduction of their size due to evaporation. In the model used by Xie et al. (2007) the evaporation rate depends on the salts dissolved in the droplets (other organic compounds were not considered). Different air ejection velocities and mouth aperture were set to simulate different expiratory activities (breathing, speaking, coughing and sneezing) and different RH ambient conditions. Xie et al. (2007) showed that the range of distances spanned by the droplets that settle at the ground increases due to the transport by the gaseous phase. Besides, droplets evaporate according to the local characteristics of the air jet rather than ambient conditions. In particular, a

strong dependency of the results on air ejection velocity was observed. Besides, the cut off size identifying the droplets that evaporate completely before settling resulted to vary with ambient RH, highlighting the difficulty in identifying one general cut off size between "large" droplets, responsible for direct of fomite transmission, and "small" droplets, responsible for airborne transmission.

The role played by the air cloud dynamics on droplet dispersion is analysed in Bourouiba et al. (2014) on the basis of high speed imaging used to visualize the droplets ejected by some volunteers while coughing and sneezing. The results showed that only the largest droplets follow ballistic trajectories and highlighted how they are weakly affected by the gaseous phase. In fact, most of the droplets were trapped within the air cloud and carried forwards. Visualizations of the gaseous phase were also performed by the previous authors by using a smoke generator. The latter provides insight on the air cloud dynamics in sneezing and coughing, which can be described as a two-stage phenomenon. It consists of a starting jet phase, corresponding to the ejection and lasting less than 1 s, and a puff phase, after the ejection has ended. The effect of buoyancy resulting from the higher temperature of the ejected air with respect to the ambient is also observed. The applicability of existing jet and puff models has been tested by water thank experiments reproducing the ejection. Bourouiba et al. (2014) proposed a simple dispersion model in which the droplets are treated globally instead of singularly as done by Xie et al. (2007). Existing model describing the dispersion of the gaseous phase as a puff are used by Bourouiba et al. (2014) (only puff phase is considered, i.e., an instantaneous ejection of buoyancy and momentum). The air cloud decelerates due to entrainment of ambient air. Droplets are considered to move jointly with the gaseous phase until the cloud velocity becomes smaller than their settling velocity. When this condition is reached, the droplet exits the cloud and starts to follow a ballistic trajectory resulting from its settling velocity and the horizontal velocity at the time of the fallout from the puff. Therefore, larger droplets fallout and settle closer both in time and space from the emission. Droplets continuously fallout so that their number within the cloud reduces in time proportionally to their settling velocity, the width of the cloud and their concentration. The continuous fallout of the droplets is more similar to that observed in the real case due to the turbulent nature of the air cloud. Analogue experiments carried out in the water thank using glass spheres of different sizes are used to validate the model. In the work by Bourouiba et al. (2014) evaporation is not taken into account.

Other works support the treatment of the air cloud dynamics by means of jet and puff models, such as VanSciver et al. (2011) and Wang et al. (2020b) (coughing) and Abkarian et al. (2020) (speaking and breathing). In these works real-scale experiments involving human volunteers are carried out and the cloud dynamics is studied by means of Particle Image Velocimetry technique.

Wei and Li (2015) conducted a work analogous to that by Xie et al. (2007), i.e., he considered a stationary turbulent jet to model the air cloud dispersion. The momentum balance equation was solved for each droplet, while the evaporation and the effect of dissolved

salts was taken into account. However, differently from Xie et al. (2007), the effect of the turbulence on droplet motion was included by means of a Discrete Random Walk (DRW) model. As already seen in Bourouiba et al. (2014), droplets that settle span a wide range of distances from the mouth due to turbulence and can travel further. The results in Wei and Li (2015) confirm the findings of Xie et al. (2007) concerning the effects of air ejection velocity and ambient RH.

Liu et al. (2017) focused on the droplet-nuclei formation for different ambient conditions, proposing a model to estimate its size and testing it by means of experiments. Then, the authors used the same model of Wei and Li (2015) to simulate droplet dispersion.

Chaudhuri et al. (2020), following an approach similar to that by Xie et al. (2007), improved the droplet evaporation modelling including the effect of solid crystallization on the evaporation rate. Furthermore, in the latter work a chemical reaction-like mechanism is suggested to model the spread of the pandemic between the infected individual to susceptible people in a given volume.

In the work by Balachandar et al. (2020) all the processes from droplet formation and ejection to droplet transport and evaporation and finally, to inhalation by a susceptible individual (including possibly effects of masks) are reviewed. In Balachandar et al. (2020) a model able to provide time variation of droplet size distribution within the droplet-laden air cloud was presented. The model can be considered as an improving of that by Bourouiba et al. (2014) in that droplets are considered globally and it includes droplet evaporation. The work provides information on what was only implicit in previous works, namely, the evaluation of the size and quantity of droplets that remain suspended and can be, therefore, responsible for short-range airborne transmission. On the other hand, previous works show the distances travelled by the droplets of different sizes before settling or before settling and/or evaporating (expressed as a unique value or associated to a probability, when turbulence effect on droplet motion is considered). In those works quantity and size of suspended droplets is only implicit in the difference between the exhaled and the removed ones. Balachandar et al. (2020) underlined the lack of accurate characterization of ejected droplets and of a precise calculation of evaporation rate of droplets with realistic composition.

In Wang et al. (2022) a model similar to that by Balachandar et al. (2020) was used. Given the initial droplet distribution expressed in terms of volume, the normalized viral load due to droplets that are neither settled nor evaporated at different horizontal distances from the emitter is computed. This result is, then, compared to the viral load responsible for infection. Note that in this case, only direct transmission is considered.

Together with simple models, real-scale and laboratory experiments and a large number of Computational Fluid Dynamics (CFD) simulations has been carried out. CFD simulations can reproduce in detail the airflow downstream of the mouth/nose. For this reason, CFD can be useful to reveal complex phenomena that cannot be taken into account using theoretical models or that cannot be detected experimentally. Besides, CFD is useful to perform sensitivity tests on the relevant quantities such as boundary and ambient conditions. Lastly,

it is useful to assess complex situations, such as the effect of ambient airflow affecting the exhalation and complex geometries, as occurring in indoor environments (Nishandar et al., 2023; Chillón et al., 2023). In fact, the latter can be analysed only with great simplification by means of analytical models, e.g., considering regular empty indoor spaces characterized by complete mixing conditions or rather simple thermal stratification (Burridge et al., 2022; Buonanno et al., 2020; Hunt and Kaye, 2006). Besides, real-scale experiments can cover only a point or at least a small portion of the entire indoor environment.

Some examples of CFD simulations reported in the literature are briefly described in what follows. In most of the cases, an Eulerian-Lagrangian approach is used to solve both the airflow and the droplet motion. The effects of the microenvironment surrounding the droplets on their evaporation has been analysed by by Wang et al. (2021) by means of a Large Eddy Simulation (LES). The results showed the mechanisms of droplet condensation due to super-saturation conditions within the air cloud. The effects of the turbulence on the humidity field - neglected in simpler models where only the mean quantities are considered, and hardly observable experimentally – is stressed out in the Direct Numerical Simulations (DNS) by Rosti et al. (2021), which evidenced the importance of a correct turbulence modelling in these phenomena. De Padova and Mossa (2021) used Smoothed Particle Hydrodynamics (SPH) - rarely considered in this context - to model respiratory activity. The effects of ambient RH and temperature have also been assessed by Wang et al. (2021) and Busco et al. (2020). In the latter the effect of PM2.5 and PM10 in the atmosphere on exhaled droplet dispersion is also analysed. Dbouk and Drikakis (2020a) in their Reynolds Averaged Navier-Stokes (RANS) simulations investigated the effect of ambient airflow moving in the same direction of the ejection. Singhal et al. (2022) analysed the interaction between the air jets produced by two people speaking one in front of the other, stressing out the relevance of the span distance, and not only of the streamwise one. In Li et al. (2022), Busco et al. (2020) and Rosti et al. (2020) sensitivity analysis on different boundary conditions were carried out. Namely, Li et al. (2021) found out from their real-scale experiments that the droplets are exhaled only at the early stage of the cough, with a velocity that slightly differs from the gaseous phase. Besides, the droplets depart from the mouth with a wide range of directions. Their DNS showed that the ejection angle of the droplet-laden air cloud has a relevant effect on droplet dispersion, namely, reducing the streamwise spread of settled droplets and increasing the spanwise spread. The analysis by Busco et al. (2020) is similar to the one on the ejection angle by Li et al. (2022). However, in this case the movement of the head of the emitter person causes a spread of the droplet-laden air cloud direction . Finally, Rosti et al. (2020) showed the effect of the initial droplet size distribution by considering different distributions provided by the literature as input for their DNS. The results were completely different among the cases considered.

Several works in the literature focused on the characterization of droplet-laden air clouds at the emission, both in terms of ejection velocity and droplet size. In fact, as seen earlier, those two quantities play a major role in defining the fate of the droplets downstream of the mouth.

The ejection velocity of the gaseous phase has been measured in real-scale experiments involving human volunteers for speaking, breathing, coughing and sneezing, e.g., in Abkarian et al. (2020), Chao et al. (2009), Kwon et al. (2012), Zhu et al. (2006), VanSciver et al. (2011), Nishimura et al. (2013), Tang et al. (2013). PIV and a shadowgraph imaging technique were used in these works to measure air velocity. Alternatively, spirometry is employed in Gupta et al. (2009) and Gupta et al. (2010), Mahajan et al. (1994), Singh et al. (1995) to determine the airflow rate at the mouth/nose.

Many efforts have been devoted by the scientific community to measure droplet size distribution as it is crucial for both droplet dispersion and for the viral load. The seminal work by Duguid (1946), still taken as a reference, has been followed by several authors, e.g., Asadi et al. (2019), Chao et al. (2009), Johnson et al. (2011), Morawska et al. (2009), Buckland and Tyrrell (1964), Loudon and Roberts (1967), Papineni and Rosenthal (1997), Xie et al. (2009), Almstrand et al. (2010), Edwards et al. (2005), Fabian et al. (2008), Haslbeck et al. (2010), Holmgren et al. (2010), Fang et al. (2008), Gerone et al. (1966), Hersen et al. (2008), Yang et al. (2007), Zayas et al. (2012), Han et al. (2013). All these studies involved healthy and/or infected people (only a few) which were asked to speak, breath, cough, sneeze and vocalize following various protocols. Different measurement tools have been employed including solid and liquid impaction, optical particle counter, aerodynamic particle sizer, electric low-pressure impactor, scanning mobility particle sizer, high-speed photography, and Interferometric Laser Imaging for Droplet Sizing (ILIDS). The exhaled droplets are found to span a wide range of sizes (o(0.1) o(100) μm) and, quite unexpectedly, they are ejected also during non-violent respiratory activities, such as speaking and breathing, even if in smaller quantity. However, the size distributions measured for the same respiratory activity differ significantly from each other in terms of number of droplets, most frequent sizes and overall size range (Seminara et al., 2020; Bourouiba, 2021; Mittal et al., 2020). This is due to several reasons (Gralton et al., 2011), firstly the intrinsic variability among human volunteers, which is not easy to take into account, and, secondly, the wide range of droplet sizes, which is hard to cover with one instrument only, so that measurements carried out by means of different tools provided droplets in different size ranges. Besides, the effectiveness of the tools often varies with droplet size. Thirdly, each tool is generally based on different assumptions on droplets properties, which are not always valid, and on different physical mechanisms, which involves the measure of diameters of different nature (e.g., aerodynamic, optical, mobility diameters). Finally, since for technical reasons the measure is taken at a finite distance from the emission, it can be affected by dilution and evaporation, the latter being complex to estimate. It is worth noting that dusts naturally present in the air could interfere with the measurement in that they could be confused with exhaled droplets.

Another quantity characterizing the emission is droplet velocity and direction. As pointed out by Bahl et al. (2021), ejected droplet dynamics have been experimentally assessed only rarely, even if they can be useful both for the comprehension of the phenomenon and to provide input data for numerical modelling. Nishimura et al. (2013) used high-speed imaging

with volumetric illumination and PIV technique to measure droplet velocity away from the mouth for the sneezing activity, but not for coughing due to lower droplet concentrations and smaller droplet sizes. As previously mentioned, Bourouiba et al. (2014) tracked the largest droplets ejected in a cough or a sneeze using volumetric illumination and high-speed imaging. Bahl et al. (2020) used high-speed imaging with LED light sheet illumination and Particle Tracking Velocimetry (PTV) technique to measure the velocity of droplets ejected during a sneeze between 0 and 25 cm from the mouth. Bahl et al. (2021) used the former experimental setup but here the results are compared to that obtained using a spirometer. The results evidenced a wide spread of departure directions of the droplets from the mouth. Based on high-speed imaging with volumetric illumination, Li et al. (2022) tracked droplets exhaled during a cough larger than $\sim$ 10 μm. It is shown how the droplets are ejected only at the beginning of the cough and that their spread angle at the mouth is larger than for the gaseous phase. To our knowledge, only two works assessed the correlation between droplet size and velocity, i.e., Wang et al. (2020b) and de Silva et al. (2021). In both cases, LED backlight illumination was used. Due to the compromise between Field of View size, high-speed of the recording and sensor resolution, only rather large droplets ($\geq$ 250 μm in Wang et al. (2020b) and $\geq$ 36 μm in de Silva et al. (2021)) were measured.

From the previous analysis emerges that one of the problems in droplet-laden modelling consists in the characterization of droplet size and velocity at the emission. The present work tries to make a contribution to the field by improving experimentally the emission characteristics in terms of both droplet size and velocity distributions.

1.2 Aim and structure of the thesis

This thesis tries to characterize droplet emission during different respiratory activities. Namely, droplet size and velocity are measured simultaneously close to the mouth for the activities of speaking, coughing and breathing. To this aim, two measurement campaigns have been carried out involving 23 volunteers. The Interferometric Laser Imaging for Droplet Sizing (ILDS) has been used as it requires a rather simple setup and makes it possible to overcome some of the problems encountered in previous works. An effort has been made to improve the technique (concerning both the setup and data processing) with respect to its classical applications, allowing us to measure droplets down to 2 μm and all the three components of the droplet velocity. Lastly, CFD simulations have been performed for the speaking activity using the experimental data collected during the experiments.

The thesis has been co-supervised by the Sapienza University of Rome, the École Centrale de Lyon and the Italian Workers' Compensation Authority, who founded the work.

The present thesis has been structured as a collection of journal papers, i.e., each chapter is independent of the others and has its own introduction and conclusions.

In Chapter 2 the basic principles of the ILIDS technique along with the main metrological aspects and problems are reported. Then, the setup and the in-house image processing

method developed to analyse the collected data are described. Attention here is focused to the detection of droplets down to 2 μm and to the measurements of all three velocity components of the droplet. Besides, the methodology allowing the estimation of the measurement volume – usually not considered in this kind of measurements – is presented. Lastly, some preliminary results are shown.

Chapter 3 shows droplet size and velocity distributions obtained using ILIDS for the activities of speaking, coughing and breathing. The results are compared to literature data. The effect of protection masks on both size and velocity of the exhaled droplets is also assessed. Lastly, the variability of the results for the same volunteer repeating the tests is evaluated.

In Chapter 4 the results of the CFD simulations regarding the speaking activity carried out using as input the experimental data are shown. The effect of initial droplet velocity is assessed.

The conclusions are reported in Chapter 5.

Chapter 2

Interferometric imaging for respiratory droplet sizing

2.1 Introduction

The particle-laden air cloud ejected by humans during different respiratory activities has drawn the attention of the scientific community since the first half of the 20^{th} century as it is involved in infectious disease transmission. This problem has become of major importance in the past two years due to the COVID-19 pandemic. Even though numerous experiments and numerical models have recently been carried out to assess the dynamics of dispersed cloud ejection (De Padova and Mossa, 2021; Dbouk and Drikakis, 2020a,b; Bourouiba et al., 2014; Busco et al., 2020; Wang et al., 2020a; Chaudhuri et al., 2020; Li et al., 2022; Wei and Li, 2015, 2017; Xie et al., 2007; Buonanno et al., 2020), a lack of knowledge regarding the way in which particles are ejected by humans is present yet (Rosti et al., 2020; Seminara et al., 2020; Mittal et al., 2020). Since model results often influence decision-making bodies in politics and public health, it is imperative for these dispersion models to be properly run with reliable initial data before their prediction may be used with a certain degree of confidence. In particular, experimental characterization of cloud ejection is useful to provide realistic data concerning air velocity as well as particle size and velocity distributions at the emission point. These quantities are important as ejected particle velocity and air velocity are expected to be different, particularly for the larger particles. Besides, particle velocity could vary with particle size. Particle size distribution and air velocity have been measured in several works, but only a few researches focused on the simultaneous measurements of particle size and velocity.

Size distribution of particles ejected during different respiratory activities, i.e., breathing, speaking, coughing, and sneezing has been analysed, among others, by Han et al. (2013), Johnson et al. (2011), Asadi et al. (2019) (see also the review by Gralton et al. (2011) and the references cited therein). Different experimental techniques have been used in the past to measure particle size distribution, i.e., solid and liquid impaction (Duguid, 1946; Loudon

and Roberts, 1967), optical particle counter (Han et al., 2013; Papineni and Rosenthal, 1997), aerodynamic particle sizer (Asadi et al., 2019; Morawska et al., 2009; Johnson et al., 2011), electric low pressure impactor (Hersen et al., 2008), scanning mobility particle sizer (Holmgren et al., 2010), high-speed photography (de Silva et al., 2021), and Interferometric Laser Imaging for Droplet Sizing (ILIDS) (Chao et al., 2009). Despite the large availability of data, the works show considerable differences in the results (Bourouiba, 2021; Johnson et al., 2011; Seminara et al., 2020; Mittal et al., 2020). This lack of agreement between different data sets enlighten the hurdles that have to be faced when characterising experimentally this complex phenomenon.

The velocity of the ejected air has been measured by means of Particle Image Velocimetry (Zhu et al., 2006; Chao et al., 2009; VanSciver et al., 2011; Nishimura et al., 2013) and real-time shadowgraph imaging (Tang et al., 2013). Alternatively, the airflow has been measured by means of spirometers (Mahajan et al., 1994; Singh et al., 1995; Gupta et al., 2009, 2010; de Silva et al., 2021). Only in a few cases experimental setups based on high-speed imaging techniques have been employed to measure the velocity of the ejected particles directly (Bahl et al., 2020; Nishimura et al., 2013; Scharfman et al., 2016; de Silva et al., 2021; Bahl et al., 2021). Even more rare are the simultaneous measures of particle size and velocity. This kind of measurement is not easy due to the small size of the particles and their low concentration. To our knowledge only two studies, i.e. Wang et al. (2020b) and de Silva et al. (2021), faced this problem, but only for large particles. In the former paper the authors carried out a joint pdf of particle size and velocity for particles larger than 250 µm using particle shadow tracking velocimetry technique. de Silva et al. (2021) measured simultaneously particle velocity and size down to 36 µm using a back illumination and a high-speed camera. In both cases, only the vertical and the streamwise (normal-to-the-mouth) velocity components of the particles were measured, while no information about the spanwise component was available.

To provide an experimental characterization of the particles ejected by humans during different respiratory activities - namely measuring the three velocity components and size of the particles - we adopt here the ILIDS technique, which has so far never been used for this purpose. ILIDS is an interferometric technique based on a laser sheet illumination and an out-of-focus image recording. It was originally developed for liquid spray by Glover et al. (1995) based on a previous work of Ragucci et al. (1990). The basic idea is to combine the high accuracy of interferometric techniques with the capability of image analysis techniques to separate and identify several objects individually. The technique has been applied in several configurations (Dehaeck and van Beeck, 2008; Porcheron et al., 2015; Rezaee and Kebriaee, 2019; Sahu et al., 2016; Yilmaz et al., 2021) and extended to velocity measurements (Maeda et al., 2000) and bubble size measurements (Kawaguchi et al., 2002; Mees et al., 2011). One of the strengths of ILIDS is that it permits the simultaneous measurement of particle size and velocity using a Particle Image Velocimetry setup (double cavity laser and double frame camera or high repetition rate pulsed laser and camera). Another advantage of ILIDS is that it allows liquid droplets to be distinguished from suspended irregular solid particles even in

a real environment, out of cleanroom conditions. Even though its applications are generally limited to diluted sprays, ILIDS is well suited to measure the low concentration of respiratory aerosols as well. A limitation of the ILIDS concerns the minimum size of the droplets that can be recognized, which depends on the aperture angle of the collection optic. In principle, a collection angle of about 40° is required to measure water droplet size down to 2 µm, which is far above the effective aperture of standard optics (note that contrary to the common usage in the literature concerning airborne disease transmission, the term *droplet* is used in the present paper to mean liquid particles in general, including small liquid particles). To apply ILIDS to respiratory droplets and recognize particles with very small diameter, a large aperture optic, free from spherical aberration, must be designed. Finally, the estimation of the measurement volume and the related particle concentration is not an easy task using ILIDS in that it is not possible to fix the size of the measurement volume a priori. For this reason, the measurement volume and its variation with the particle size has been estimated in the present work based on droplet location along the direction normal to the laser sheet.

The paper is organized as follows. Section 2 describes the principle of the standard ILIDS technique along with the improvements made to (i) detect droplets down to 2 µm, (ii) measure the three velocity components and size of the particles and (iii) determine the measurement volume for each size class and, hence, the droplet concentrations. Section 3 describes the experimental setup, the experimental protocol and the image processing procedure. The results are presented in Section 4, enlightening the potential of the ILIDS technique for respiratory droplets characterization. Conclusions are summarized in Section 4.

2.2 ILIDS technique

2.2.1 Basic principles

The ILIDS technique is based on the light scattering properties of transparent particles. As shown in Figure 2.1, the droplets are illuminated by a coherent light source (the laser sheet) and the light scattered by the droplets is collected by a lens (or a lens assembly) with collection angle α centred around the direction identified by angle θ. With a classical imaging system, the droplet images would form in the image plane at distance L_f. Conversely, with the ILIDS technique the sensor is placed on an out-of-focus plane at distance L_{out}. The light scattered by a single droplet gives rise to an interference pattern (fringes) produced by the superposition of reflected light, refracted light and light refracted after one or multiple internal reflections. At a given angle θ, the fringe spacing directly depends on the particle diameter. Incidentally, it is worth noting that while for a single drop an accurate measurement of the drop size could be obtained by placing a sensor (instead of the lenses) at the lens location able to record the interference pattern (see Figure 2.1), in the case of several droplets the interference patterns would be superimposed on each other, and the information from individual droplets would be lost. With ILIDS, out-of-focus particle images are recorded by means of a lens (or a lens

assembly) and a camera. In the out-of-focus plane, each droplet image takes the form of a circle containing the corresponding interference pattern. The circle location corresponds to the droplet location in the object plane (plane coinciding with the laser sheet where the observable objects, i.e., the particles, lay). Different droplets generate separated circles on the sensor, allowing the analysis of individual interference patterns and droplet size measurement. Note that, in ILIDS, the circle size is not related to the droplet size, but it only depends on the out-of-focus level, i.e., the ratio l/L_f. If the laser sheet was very thin, all the illuminated droplets would belong to the same plane, the image plane would be the same for all droplets and all the corresponding circles would have the same size. For a thicker laser sheet, particularly when using a high magnification optic, both L_f and circle size vary significantly with the distance of the droplet from the lens, and the third droplet coordinate can be deduced from the circle diameter. For a spherical droplet, the interference pattern is easy to detect and to count in that it is composed of regular fringes in a well defined direction. Conversely, irregular solid particles can be recognized and discarded as they show less regular scattering patterns. For spherical droplets, the number of fringes in the circle equals the number of fringes that would be measured in the lens aperture, i.e., the number of fringes in the collected part of the scattering diagram. For scattering angles $20° \leq \theta \leq 80°$ the relation between fringe number and droplet diameter can be evaluated based on geometrical optics considerations. For $\theta = 90°$, as adopted in this work, the relation is deduced from Lorenz-Mie theory.

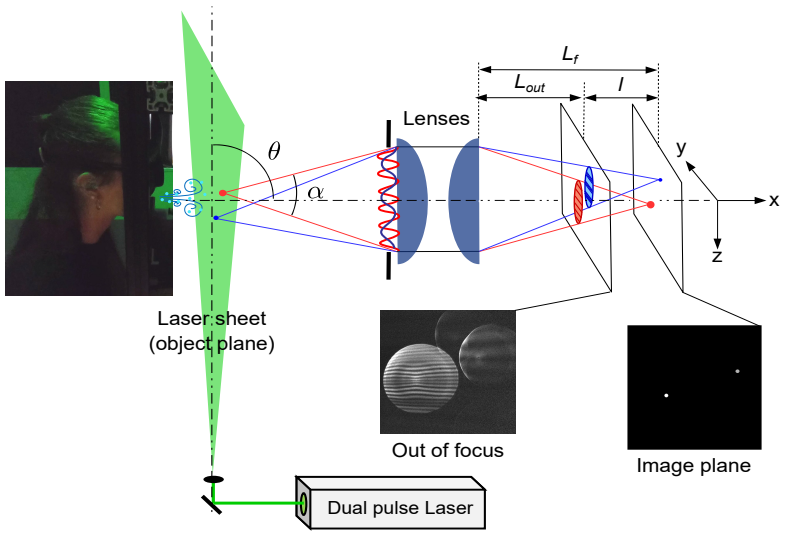

Figure 2.1: Sketch of ILIDS technique principle. A laser light sheet illuminates the particles. A portion of the light scattered by the particles is collected by an optical system (lenses) along the direction identified by θ. The angle formed between the particle and the effective lens aperture is the collection angle α. Out-of-focus images of the particles are taken by means of a camera located at a distance L_{out} from the lenses. The light scattered by the particles is characterized by interference fringes, whose frequency is related to the particle size. Therefore, in the out-of-focus image the particles appear as circles with interference fringes inside. Differently, in the image plane (at a distance L_f from the lenses) the particles appear as glare points. The out of focus images become more and more blurry as the distance l increases.

2.2.2 Particle size measurement

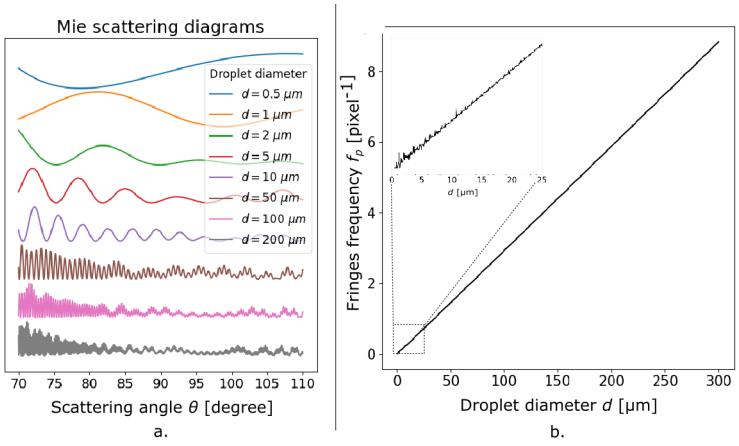

Figure 2.2: a. Water droplet scattering diagram computed according to Lorenz-Mie Theory, for droplet diameters between 0.5 and 200 μm (from top to bottom of the left panel) and b. Fringes angular frequency as a function of droplet diameter, computed by using Lorenz-Mie Theory and Fourier analysis for scattering angle centered on $\theta = 90°$, a wide collection angle $\alpha = 40°$, a wavelength $\lambda = 532\ nm$ and a sampling step on scattering angle $\delta_\theta = 0.05°$.

As mentioned in the former Section, the droplet diameter, d, can be determined in the scattering diagram from the angular spacing of the fringes, $\Delta\theta$. Assuming a perfect thin lens (i.e., of negligible thickness and not affected by any kind of aberrations) and a collection angle α, $\Delta\theta$ can be written as

$$\Delta\theta = \frac{\alpha}{N} = \frac{\alpha}{2Rf_p} \tag{2.1}$$

where N and and R are the fringe number and the circle radius in out-of-focus image, respectively, while f_p is the fringe frequency, measured in pixel unit. Figure 2.2a shows portions of the scattering diagrams for $70° \leq \theta \leq 110°$ ($\alpha = 40°$ centered on $\theta = 90°$) and droplet diameters lying in the range 0.5 - 200 µm. The laser beam is linearly polarized. The polarization direction has been chosen perpendicular to the plane of incidence (x, z) (S-polarization) to maximize the fringe contrast for the smallest droplets. Figure 2.2a also reveals that the number of fringes is too low to be measured for the smallest diameters, even with $\alpha = 40°$. The lower limit for droplet diameter measurement is then around 1.5 µm, corresponding to about 2 fringes in the collection angle. A smaller α would increase the lower limit, while an α significantly greater than 40° can hardly be considered in practice for several reasons, as detailed below. Thus $d_{min} = 1.5$ µm can be considered as the lower limit of the technique, and a wide collection angle (nearly 40°) is required to reach this limit.
The relation between the fringe spacing $\Delta\theta$ (or the fringe angular frequency $\Delta\theta^{-1}$) and droplet diameter can be established by using the Lorenz-Mie theory. Figure 2.2b depicts the main fringe frequency as a function of the droplet diameter for $\theta = 90°$, $\alpha = 40°$, light wavelength $\lambda = 532$ nm and sampling step on scattering angle $\delta_\theta = 0.05°$. This figure has been obtained by computing scattering diagrams similar to those presented in Figure 2.2a for droplet diameters

going from 0.5 µm to 300 µm and by extracting the main fringe frequency from the derivative of the Fourier transform of each diagram. As Figure 2.2b also shows, the droplet diameter is proportional to the fringe angular frequency, viz.

$$d = \kappa \frac{1}{\Delta\theta} = \kappa \frac{2Rf_p}{\alpha} \tag{2.2}$$

The coefficient $\kappa = 34.0$ µm degree is calculated from a linear regression of the curve (Figure 2.2b). This coefficient depends mainly on λ, θ and the droplet refractive index n. It also varies weakly with the collection angle ($\kappa = 35.2$ µm degree for $\alpha = 10°$ and $\kappa = 33.9$ µm degree for $\alpha = 44°$).

For the smallest diameters (inset in Figure 2.2b) oscillations due to both Mie scattering properties and signal sampling are observed. These oscillations clearly limit the accuracy of the measurement of the smallest particles, with an uncertainty greater than 40% for diameters lower than 1.5 µm. This confirms that 1.5 µm is the lower particle diameter measurable with the ILIDS technique. To account for this unavoidable source of uncertainty, only droplets having $d_{min} \geq 2$ µm will be considered in the remainder of this work. For $d_{min} \geq 2$ µm the absolute error is less than 0.45 µm.

The maximum measurable particle diameter d_{max} depends on the sampling conditions. For the parameters adopted to compute the curve presented in Figure 2.2b, in particular $\delta_\theta = 0.05$, the Nyquist frequency $f_{max} = 10$ pixel^{-1} corresponds to a maximum diameter $d_{max} = 340$ µm.

Note that the range of measurable diameters is also limited by the dynamic range of the camera sensor. The intensity of scattered light is roughly proportional to the particle diameter squared. Using a 16bit-camera with a low read noise, the diameter range is limited to one or two orders of magnitude. To measure particle sizes down to 2 µm, the scattering diagram (Figure 2.2a) must be collected over a large collection angle and entirely projected onto the sensor. In practice, the effective collection angle is limited by spherical aberrations as illustrated by the examples of ray tracing depicted in Figure 2.3. When using a pair of spherical lenses (Figure 2.3a), the rays collected at large angles (far from the optical axis) are focused at shorter distances. In the out-of-focus sensor plane, information carried by rays with different incidence angles overlaps and the projected interference pattern is folded in on itself and deformed, thus, preventing any measurement. The different ways to limit spherical aberrations are (i) to reduce the lens aperture, thus increasing the lower size limit, (ii) to increase the magnification ratio, reducing the field of view (hereinafter FOV) and the measurement volume, (iii) to increase the defocused level l/L_f then increasing overlapping of defocused images and (iv) to use or design special lenses that reduce the spherical aberration. To reach an effective collection angle of order 40°, the last three solutions are applied together. Figure 2.3b illustrates the case of two aspherical lenses set in order to obtain a 1:1 magnification lens, nearly free from spherical aberration. In the out-of-focus plane (with the same out-of-focus level as in Figure 2.3a) the different rays formed regularly spaced concentric

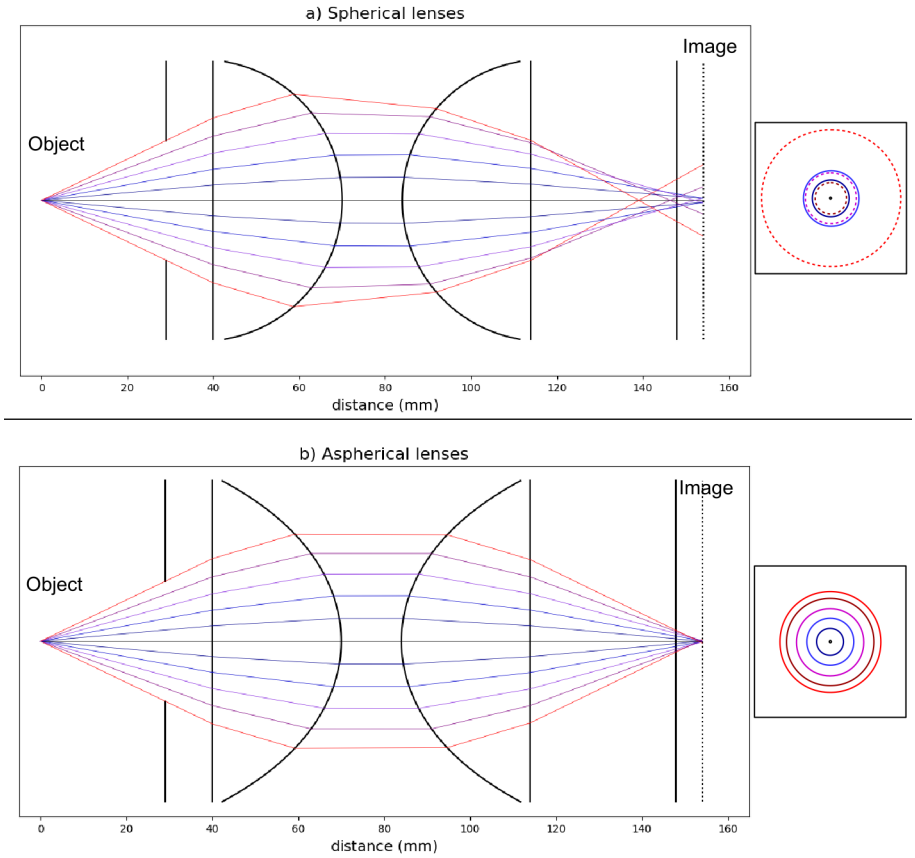

Figure 2.3: Effect of spherical aberrations on out-of-focus images. Using a pair of spherical lenses (a), the red rays at greater angles, far from the optical axis, cross this axis at shorter distances than the blue rays, closer to the optical axis. Using aspherical lenses (b), almost all the rays cross the optical axis at the same distance. As a consequence, a set of concentric circles corresponding to the different rays appears on the out-of-focus images. With aspherical lenses, the circle diameter increases linearly with ray angle. With spherical lenses, the circle diameter increases, then decreases and increases again, leading to a destructive folding of the fringes to be analysed.

circles, without any folding. This means that, despite the large collection angle ($> 40°$), the effects of spherical aberration are negligible. Note that this collection angle is however limited by an adjustable aperture placed in front of the first lens. To select the maximum aperture for which spherical aberrations remain negligible, the procedure consists in increasing it progressively while the circle diameter in the out-of-focus plane remains proportional to the aperture diameter. Preliminary to this work, several commercial lens assemblies have been tested. The largest collection angle has been obtained by using a 100 mm macro lens (Zeiss Milvus 2/100M) similar to the one used by Chao et al. (2009). The nominal aperture of this lens is 50 mm but it must be reduced to less than 30 mm to fulfill the ILIDS requirements, leading to an effective collection angle of about 12° and minimum measurable diameter of about 6 µm. Note that this low performance of commercial lenses to compensate the spherical aberration is not surprising. Such lenses are optimized to reduce several kinds of geometrical and chromatic aberrations on focus images and not to reduce specifically the spherical aberration and its effect in a out-of-focus plane.

Even though aspherical lenses could be used to reduce spherical aberration, they are not

perfectly thin and are prone to other geometrical aberrations. In particular, the image of an object away from the optical axis is deformed due to comatic aberrations. In the out-of-focus plane, the circles containing the interference patterns are deformed, in particular when the particle is close to the sensor edges. In the present case, the deformed circles are nearly elliptical and the effective collection angle is not affected significantly. The deformation does not prevent the measurement but it must be considered in the image processing phase. For droplets close to the top or the bottom of the image, the circle deformation is maximal in the direction perpendicular to the fringes, leading to a reduction of the fringe sampling condition of about one third. Therefore, the maximum measurable diameter for droplets in these image areas decreases by the same factor to about $d_{max} \sim 225$ µm.

2.2.3 Particle velocity measurement

As mentioned earlier, the setup used in this work allows us to measure all three components of the particle velocity vector. These are determined from the particle coordinate changes between two images recorded with time delay Δt. The spanwise (y) and vertical (z) coordinates are evaluated from the circle centre displacement in the sensor plane, while the streamwise coordinate (x, i.e., normal-to-the-mouth) is deduced from the circle size variation. Let us con-

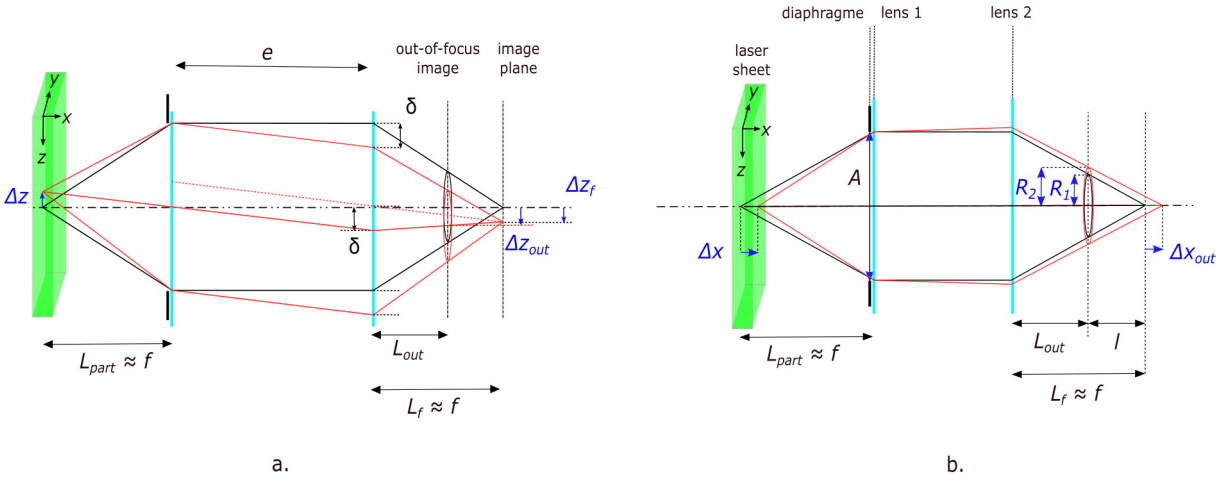

Figure 2.4: a. y,z-displacement and b. x-displacement. The conditions at two subsequent time steps are depicted in black and red. The displacements of the particles occurring between the two time step are Δz and Δx. In case a. the displacement Δz_{out} is observed in the out-of-focus image. In case b. the circle radius variation ΔR is observed in the out-of-focus image. The lines linking the particle in the laser sheet and its image are the central and the two extreme light ray paths.

sider a simple idealized lens assembly to illustrate how the circle position in the out-of-focus image varies with the particle displacement along the z-axis (or y-axis). The lens assembly is composed of two perfect thin lenses having the same focal length f and spaced at a distance e (Figure 2.4a). For a particle located in the focal plane of the first lens, simple geometric considerations leads to the following relationship between the circle displacement, observed in the out-of-focus image Δz_{out} (or Δy_{out}), and the real displacement of the particle Δz (or

Δy):

$$\Delta z_{out} = \Delta z \left[\frac{e - L_{out}\left(\frac{e}{f} + 1\right)}{f} \right] = -\gamma_1 \Delta z \tag{2.3}$$

where γ_1 is a constant that depends on the optical system characteristics, i.e., f, e, the distance L_{out} between the first lens and the out-of-focus sensor plane, and the aperture A.

As mentioned in Section 2.2.1, the radius of the circle associated to a particle depends on the distance between the particle and the optical system. As the laser sheet has a non-zero thickness, it is possible to detect the particle at different distances from the optical system (different positions within the laser sheet thickness). The third coordinate x can therefore be calculated from the circle radius R. Considering the same idealized optical system, with magnification $M \approx -1$, the circle radius for a particle located at Δx from the focal plane of the first lens can be written as

$$R(\Delta x) = \frac{A}{2} \left[1 + \frac{e\Delta x}{f(f - \Delta x)} \right] \left[1 - \frac{L_{out}}{f - \Delta x} \right] \tag{2.4}$$

The radius variation ΔR, for Δx close to zero is nearly proportional to the displacement Δx, that is

$$\Delta R \approx \frac{A}{2f^3} \left(ef + L_{out}f - eL_{out} \right) \Delta x = \gamma_2 \Delta x \tag{2.5}$$

γ_2 is nearly constant for small displacement Δx and depends on the optical system characteristics. Note that the variation of the circle radius R does not affect the measurement of droplet size d. Since f_p varies inversely as R varies, the fringe angular frequency $1/\Delta\theta$ does not vary, and so does the droplet size d (see Equation 2.2).

To take into account for the real characteristics of the optical system used in the experiments and the inevitable default of optical adjustment, the two constants γ_1 and γ_2 have been estimated by means of a calibration procedure (see Section 2.3.2).

2.2.4 Measurement volume and particle concentration

ILIDS is based on a laser light sheet illumination that is supposed to delimit the measurement volume. However, the intensity of the laser sheet profile $I(x)$ is never perfectly sharp, so that the identification of the laser sheet edges is not trivial. Moreover, dealing with a large size distribution, the effective measurement volume actually depends on the particle size (Figure 2.5). Therefore, the measurement volume cannot be estimated a priori by multiplying the FOV with the thickness of the laser sheet. To be detected, the light intensity corresponding to a particle on the image must be greater than a given threshold that depends on the sensor sensitivity and noise level. Considering the real shape of the laser sheet profile, the actual width within which a particle can be detected decreases with its size. On the one hand, the intensity of the light scattered by a particle is roughly proportional to the square of its diameter and to the incident light intensity at the particle location. On the other hand, $I(x)$ is not constant along the laser sheet thickness, but it is rather characterised by a smooth

Gaussian-like shape. The measurement volume decreases with the particle size since smaller particles can be detected only at the centre of the laser sheet, where the light intensity is sufficiently high. Conversely, the largest particles can be detected even in the edges of the laser sheet, where the light intensity is smaller, leading to a greater measurement volume. Note however that the largest particles located in the center of the laser sheet may lead to sensor saturation. This would prevent fringe frequency measurement, therefore leading to a measurement volume split into two parts. Besides, one should also consider the variation with x of the circle radius in the out-of-focus image. For smaller circle radii, the same amount of energy collected by the lenses is contained in a smaller area (circular surface in the out-of-focus image). Therefore, the minimum laser light intensity for which a particle of a given size can be detected is lower when the particle is positioned further away from the lenses, i.e. when the circle radius in the image is smaller. The most reliable way to quantify the

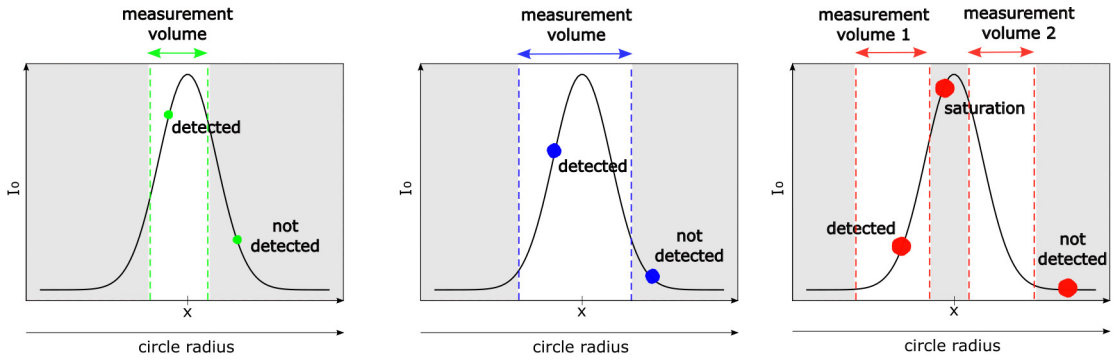

Figure 2.5: Detection range for particle of different sizes. Small, medium and large particles are represented in green (left panel), blue (central panel) and red (right panel), respectively. I_0 is the laser light intensity, while x is the position within the laser sheet thickness.

measurement volume for each particle size class is to deduce it *a posteriori* considering the actual x-coordinate variation observed for all the detected particles in a particle size class, d, through its standard deviation, $\sigma_x(d)$. This method has been previously used by Mees et al. (2011). The measurement volume for particle diameter d is then simply estimated as:

$$V(d) = \sigma_x(d)S \tag{2.6}$$

where S is the FOV area.

2.3 Experiments

2.3.1 Setup and measurement campaign

To measure size and velocity of the particles ejected while speaking, twenty volunteers have been recruited to speak following the same protocol. To simulate the speech, they counted ten times from “one” to “one hundred”.

A double pulse Nd:YAG laser (Litron Bernoulli-PIV 200-15, wavelength: 532 nm, pulse duration: 8 ns, power: 2*200 mJ) was synchronized with a double frame camera (Lavision

imager sCMOS, 16 bit, 2560x2160 pixel, pixel size: 6.5x6.5 µm, sensor size: 16.6x14 mm) by using a programmable timing unit. The acquisition frequency was set to 15 Hz (i.e. 15 couples of frames per second). The time delay between two consecutive frames, Δt, varied with the different respiratory activities, based on the expected range of particle velocity. On the one hand, Δt must be high enough to observe a significant particle displacement. On the other hand, Δt must be small enough not to let the particle exit the laser sheet. The optical system consisted of two aspherical lenses in series (Thorlabs ACL7560U, focal length: 60 mm, lenses aperture: 75 mm) and a diaphragm, which limited the effective lenses aperture to about 28 mm. The laser sheet was parallel to the lenses and to the mouth of the volunteer (see Figure 2.6 for a schematic of the experimental setup). The location of the focus image plane was found experimentally. The corresponding magnification and field of view were $M \approx 1$ and FOV$\approx$ 14x17 mm^2, respectively. The FOV was actually slightly narrower because of the cutting of a little portion of the images made in the image processing. Both the focus-image plane position and magnification agreed well with those computed by a house made software calculating the light ray path derived from the properties of the optical system and laser sheet position. Given the distance between the laser sheet and the diaphragm, the collection angle was $\alpha \approx 45°$ – it slightly varied for particles located at the two edges of the laser sheet thickness.

A mask was used to allow volunteers to place their mouth close to the optical axis (Figure 2.6). The mask protected also the face of the volunteers and prevented them from moving, therefore avoiding any contact with the laser sheet. Besides, a black paper panel was placed between the laser sheet and the volunteers' body. The eyes of the volunteers were completely covered.

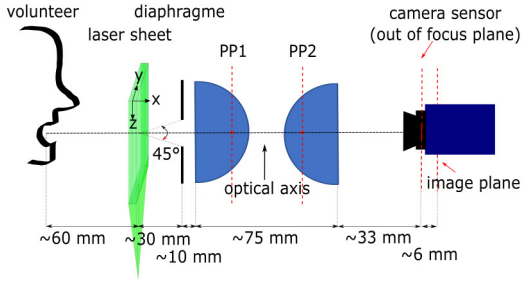

Figure 2.6: Schematic of the experimental setup. The principal planes (PP1 and PP2) of the two lenses are also drawn; these represent the position of the equivalent perfect thin lenses defined in Section 2.2.3.

2.3.2 Calibration

Several calibrations are required to consider the deformations due to comatic aberrations and to calculate the two coefficients γ_1 and γ_2 in Equations 2.3 and 2.5 [1].

As described in subsections 2.2.2 and 2.3.1, two aspherical lenses in series are used to obtain an effective collection angle $\sim 45°$, to measure particle size down to 2 µm. The

[1] A more detailed description of the three calibrations can be found in Appendix A

deformation of the circles due to comatic aberrations not compensated by these lenses must be corrected by means of image pre-processing. This consists in applying a deformation to the images to retrieve a circular shape whatever the particle location in the image. To estimate the deformation to be applied, images of a point light source are taken at different distances from the optical axis (Figure 2.7a, upper panel). The point light source consists of a pin-hole mounted on a 3D translation stage, illuminated at oblique incidence. A 5^{th}-order polynomial deformation as a function of the distance from the optical axis is chosen. The result obtained by applying the deformation to the calibration images is shown in the upper panel of Figure 2.7b. Note that this deformation is not physical, but it has the aim to make the automatic detection of the circles associated to the particles easier. Such deformation is necessary to simplify the detection of out-of-focus images, of different sizes and sometimes overlapping, by imposing a circular shape and thus reducing the number of free parameters for the detection. In the lower panels of Figure 2.7 an example of image before and after deformation is depicted. Similar images of a point light source at different positions are used to estimate γ_1. The ratio

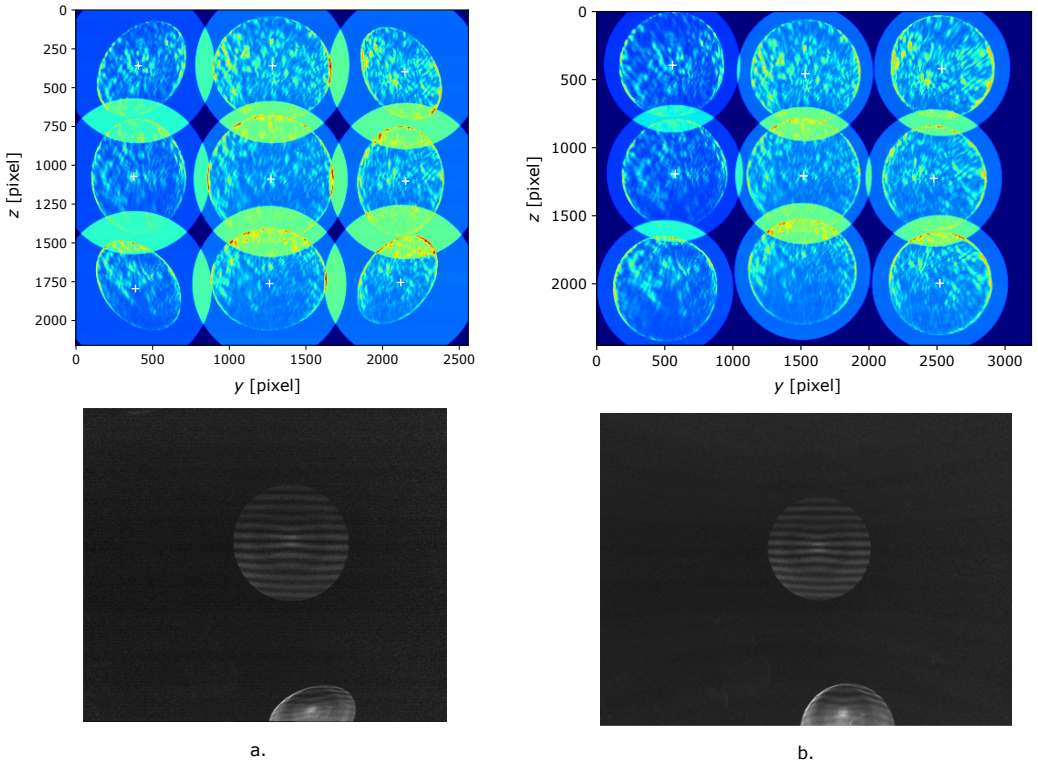

Figure 2.7: Upper panels: a. Superposition of 9 images of a point light source at 9 different distances from the optical axis and b. The same images after deformation. Lower panels: Example of image before (a) and after (b) deformation.

between the real displacement of the point light source and the displacement measured in the images is calculated. The calibration suggests that γ_1 is not perfectly constant over the whole FOV, with variations of ± 0.05 around a mean value $\gamma_1 \sim 0.91$. Note that, considering an equivalent idealized optical system, as that presented in section 2.2.3, with $f = 60$ mm,

$e = 35$ mm, $L_{out} = 54$ mm and $A = 56$ mm, Equation 2.3 would lead to $\gamma_1 \sim 0.86$.

The proportionality between ΔR and Δx (see Equation 2.5) has been tested by displacing the point light source within the laser sheet thickness and measuring the circle radius. The coefficient $\gamma_2 = 0.38$ obtained from the experiments is comparable with $\gamma_2 = 0.44$, obtained for the idealized optical system from Equation 2.5. The parameter γ_2 also varies slightly over the image and its variations are also taken into account through the calibration.

2.3.3 Image processing

The data consisted of $\sim$ 240000 images of about 15 MB each collected during the phase of speaking of the 20 volunteers. To deal with this large amount of images, a multicore version of the processing code, written in Python language has been implemented on the high-performance computers available at the Ecole Centrale de Lyon. To characterise droplet emission occurring over 2 minutes speaking (captured by 1200 images), data processing required about 96 hours (CPU time). Using 32 cores on a HPC, the effective computing time was reduced to 3 hours per test. Processing the data set acquired in the whole experimental campaign (240 000 images) would require 20.000 hours CPU on a single core, which would be reduced to 600 hours using 32 cores on HPC. In terms of memory, about 6 GB (Random Access Memory) per core are required. The image processing is composed of several steps, i.e., background subtraction, image deformation, particle detection, fringe analysis as well as velocity, size distribution and concentration calculation.

A background image is calculated for each test. It consists of the minimum intensity value for each pixel over all the images. The background image is subtracted to each image of the set.

Each image is deformed in order to compensate the aberrations as described in section 2.3.2.

In the third step, all particles – both liquid and solid – are detected by means of a convolutive approach. A Gaussian filter is applied to filter out the interference patterns within the circles. The gradient of the image is then calculated, exhibiting the circle edges, and convoluted by synthetic ring images of different sizes to detect the circles and to measure their position and radius. The detected particles are removed from the image and new particles are identified, until the correlation peak is above a fixed threshold. At the end of this step, radius and position of all detected particles are known.

In the fourth step, the interference pattern within the circles are analysed and the fringe frequency is measured. When the circles overlap, only the non-overlapped part of them is analysed. The size of the liquid particles is then calculated by means of Equation 2.2 (provided that α and k are known). At this step, solid particles are recognized and rejected in that they do not show regular interference fringes. It is worth noting that this is a point of strength of ILIDS technique applied to droplet recognition as it makes unnecessary to filter out ambient air to remove dust. However, even if the distinction between droplets and solid particles is

rather evident to human eyes, it is more difficult to perform it automatically so that detected droplets are still checked a-posteriori. In fact, the images are analysed in the frequency space by applying to them a Fourier transform. Then, the maximum of the transformed image is found, which corresponds to fringe frequency in case of droplets. Nonetheless, a maximum is always detectable, even in case of solid particles. The setting of validation criteria defining the significance of the maximum found is, hence, required. This setting is not straightforward. It has been done iteratively, based on visual inspection of a large sample of processed images. This strategy allow to recognize most of the droplets and solid particles but, some errors inevitably persist. An other strategy, based on machine learning could be considered in futur development. [2]

Particle size and position and circle radius are known at the end of the fourth step . Then, the three components of the particle velocity can be calculated by means of Equations 2.3 and 2.5 using γ_1 and γ_2 determined during the calibration procedure. The velocity components are directly inferred from associating the detected droplets in both frames once known the time delay Δt between two consecutive frames. The association of droplets from both frames is made by minimizing both particle location and size changes between the frames.

Once repeated the four steps for all the images, size and velocity distributions can be built. The measurement volume for each particle size class, and therefore the particle concentration, can be estimated from Equation 2.6.

2.4 Results and discussion

In order to show the potential of the ILIDS technique employed in this paper, some preliminary results concerning the speaking activity are presented.

2.4.1 Measurement volume

Figure 2.8b shows the measurement volume referred to a single frame for each particle size class along with the standard deviation of the circle radius, the latter proportional to the volume. The measurement volume increases almost linearly from 2 to 10 µm, while it remains nearly constant for $d > 20$ µm. The presence of such plateau can be ascribed to the weak variation of the light intensity at the laser sheet edges. However, the range of volume variation with the particle size is quite narrow, i.e. $0.2 - 0.4$ cm^3. As expected, the measured laser light intensity profile shows an almost Gaussian shape (Figure 2.8a). The figure also shows the ranges of x for which particles of 2, 10 and 20 µm have been detected. As mentioned earlier, smaller particles can be detected only at the centre of the laser sheet, where the light intensity is higher. The circle radius corresponding to each x-position is also reported (see Equation 2.5).

[2] The flowchart of the algorithm used for droplet detection and sizing is shown and explained in Appendix B

As already mentioned in Sect. 2.2.4, saturation is supposed to occur only for the larger particles (i.e., $d > 40$ µm). Nonetheless, saturation is not observed, probably because of a lack of data for the larger particles. Besides, since threshold estimation is based on light intensity measurement, it is intrinsically inaccurate.

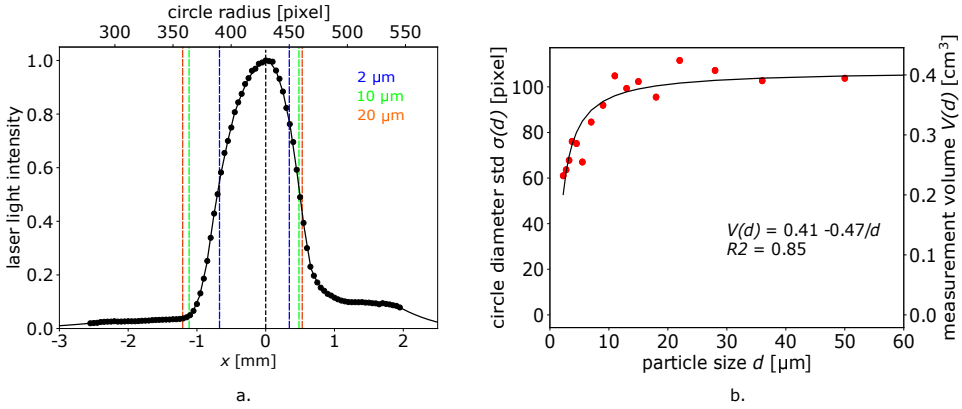

Figure 2.8: a. Measured laser intensity profile along with detection limits for particles of 2, 10 and 20 µm, b. Volume of measurement and related standard deviation of circle radius for each particle size.

2.4.2 Size distribution

Figure 2.9 shows the particle size distribution obtained considering all the tests. For each size class the particle number concentration normalized with the width of each bin size is given. The range of particle diameters detected during all the experiments is $2-60$ µm, even though most of the particles lie in the size range $2-4$ µm. The particle number decreases quickly up to ~ 15 µm. The absolute concentration maximum occurs for $d = 2$ µm, while a local maximum takes place at $d \sim 28$ µm. The size distribution obtained with the technique presented here shows no droplet sizes greater than 60 µm (even though the upper limit of the technique is above 300 µm). This shows that these larger droplets are very rare in emissions occurring while speaking. Note however that the detection of these droplets may be affected by measurement errors that would to excluded them from the statistics, in case they contain solid or gas inclusions. Indeed, the presence of inclusions would lead to a much more complex fringes pattern. This would in turn result to a complex scattering pattern that would (erroneously) interpreted as representative of an irregular (solid) particle. For the interpretation of the complex patterns characterizing irregular particles the reader is referred to the work by Brunel et al. (2014).

In Figure 2.9 we also plot data from two other works found in the literature, i.e., the seminal work by Duguid (1946), which is considered as a main reference in the field, and that more recently published by Johnson et al. (2011). In both the two works, the data were collected using almost the same protocol adopted here (for the respiratory activity associated to speaking). Johnson et al. (2011) detected a wide size range thanks to the use of a combination of two techniques, i.e. Aerodynamic Particle Sizer (APS) and Droplet Deposition Analysis

(DDA). Note that APS data by Johnson et al. (2011) appear twice in Figure 2.9. The green circles refer to APS data, while the red ones correspond to the same data set corrected for dilution and evaporation, together with the data provided by the DDA. Such correction had to be adopted since the sample probe of the APS was located far away from the volunteers' mouth.

The size distribution obtained in the present work lies between the two Johnson's distributions. We can explain this by recalling that, compared to Johnson et al. (2011), the measurement volume in our experiments is closer to the volunteers' mouth and that we did not apply any correction to the data to take into account for evaporation and dilution effects. Our results also differ considerably from those by Johnson et al. (2011) for larger particles. Namely, we observe a concentration maximum at $d \sim 28$ µm in place of the minimum found by Johnson et al. (2011). However such minimum occurs for diameters in the range corresponding to that of the maximum diameter detectable by the APS and the minimum diameter for the DDA. Note also that the efficiency of the APS decreases as the particle size increases (Morawska et al., 2009). The size distribution of Duguid (1946) differs from that presented in this work and in Johnson et al. (2011). Nevertheless, Duguid (1946) stated that the size distribution he obtained should be taken with caution, because of the several approximations he made. For instance, Johnson et al. (2011) noted that the particle size estimated by Duguid (1946) could be shifted to larger sizes due to evaporation effect overestimation. Besides, since Duguid (1946) provided only the particle number, the particle concentration had to be calculated by estimating the air volume expired during the speaking activity (Johnson et al., 2011).

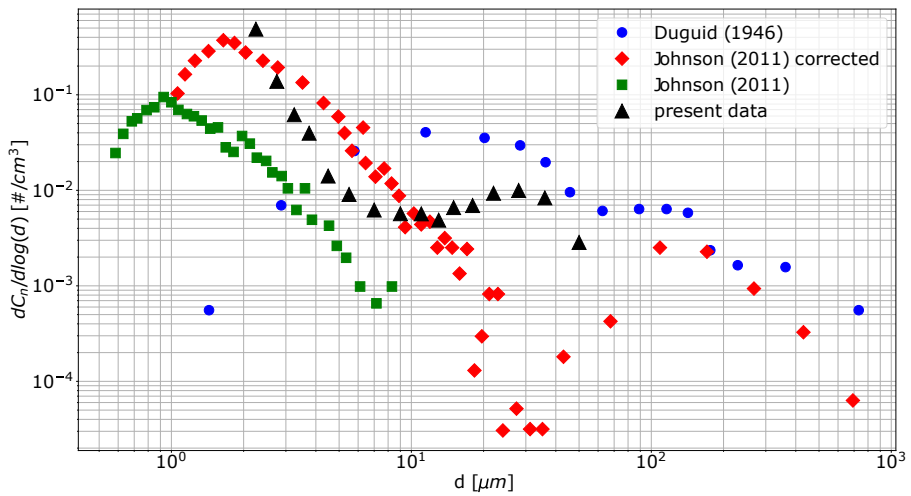

Figure 2.9: Measured particle size distribution, compared to data by Duguid (1946) and Johnson et al. (2011).

2.4.3 Joint probability density function of particle velocity and size

Figure 2.10 shows the joint probability density function (pdf) of particle velocity and size measured simultaneously in our experiments.

To build the joint pdf maps five size classes have been considered in order to have robust statistics for each size class. All three velocity components depend on the particle size. In particular, the normal-to-the-mouth velocity component, v_x, grows with the particle size. On average, v_x is about 0.1 ms^{-1} for $2 \leq d \leq 2.5$ µm and 0.3 ms^{-1} for $20 \leq d \leq 60$ µm. It is worthwhile noting the presence of negative v_x. These can be probably ascribed to air inspiration by the volunteer while speaking and particle recirculation due to vortices forming along the border of the air jet associated with the emitted air. As expected, the spanwise velocity component, v_y, has (nearly) zero mean value ($\sim$ 0.01 ms^{-1}) due to flow symmetry for all the size classes. The vertical component of the velocity v_z (positive downward) ranges between 0.02 ms^{-1} and 0.05 ms^{-1} when $2 \leq d \leq 20$ µm, while it is higher ($\sim$ 0.1 ms^{-1}) for the largest particles, probably due to their settling.

Note that the theoretical minimum detectable value of the velocity components along y and z is $\sim$ 0.005 ms^{-1}, corresponding to a displacement of 0.5 pixel in 700 µs. The minimum velocity detectable along the x-direction is slightly higher, $\sim$ 0.02 ms^{-1} (i.e. a variation of 1 pixel in the radius of the circle between two frames). The maximal detectable particle velocity is 7 ms^{-1}. However, the maximum v_x is limited by the thickness of the laser sheet where the particles can be effectively detected. Considering the values shown in Section 2.4.1, the maximum v_x for 2 µm and 50 µm particles are 1.5 ms^{-1} and 2.5 ms^{-1}, respectively. The maximal values of v_x effectively measured are slightly higher. This is due to a slight underestimation of the x-particle detection range within the thickness of the laser sheet. The latter is, indeed, estimated by measuring the standard deviation of x, but some particles could be detected at an x-position which exceeds the $\sigma_d(x)$ considered.

The mean particle velocity observed in our experiments ranges between 0.26 ms^{-1} and 0.56 ms^{-1} for the smallest and the largest particles, respectively. For comparison, the mean particle velocity measured by Wang et al. (2020b), Bahl et al. (2021) and de Silva et al. (2021) is far higher. The larger particle sizes and the different respiratory activity - i.e., coughing and sneezing rather than speaking - can explain such difference with the current work.

2.4.4 Particle direction

Particle direction can be determined once the three velocity components are known. The ratios between the velocity components, v_z/v_x and v_y/v_x, which are linked to the angle of departure of the particles from the x-axis (normal to volunteers' mouth) are shown in Figure 2.11. The ejected particle cloud appears symmetrical and the aperture angle is quite wide. About 45% and 60% of the particles fall into an aperture angle of about 60° and 90°, respectively. Only a few particles depart from the mouth with an angle larger than 70°, corresponding to a ratio $\sim$ 2.5. Note that only forward moving particles are considered in the figure.

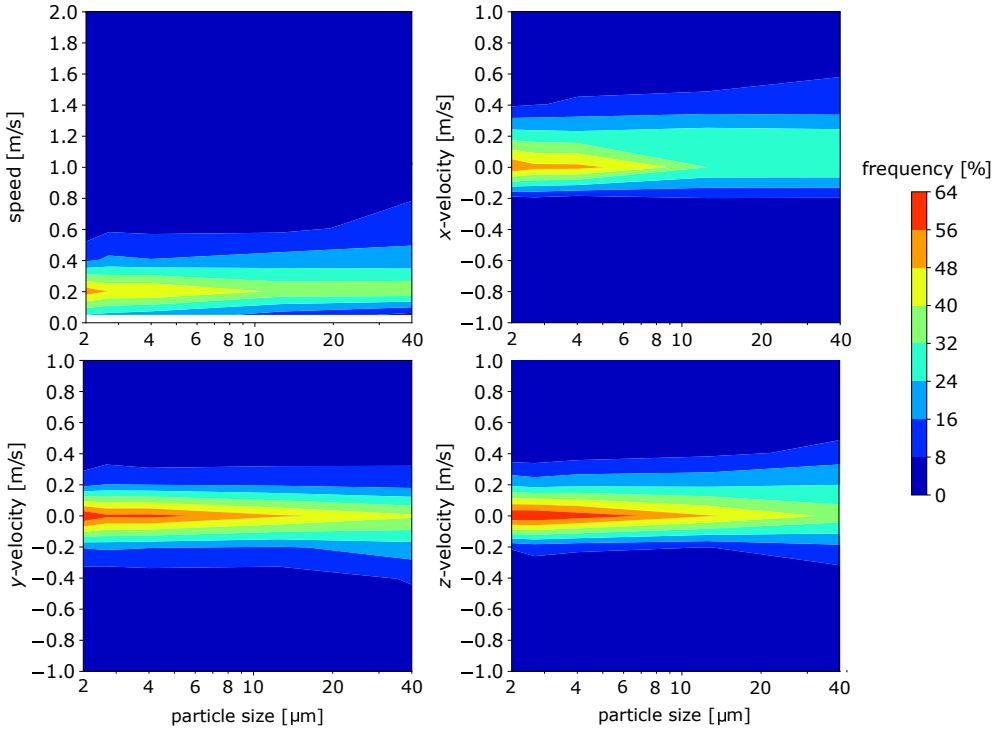

Figure 2.10: Joint probability density function of particle velocity and size. Colors are number of particles characterized by a certain size and velocity normalized by the total number of particles of each size.

2.4.5 Uncertainty estimation

The droplet sizes are determined from the image circle radius and the fringes frequency measurements. The uncertainty on image radius is estimated to be 1 pixel. Given that the circles radius are of order 400 pixels, the relative uncertainty in droplet diameter is only 0.25%. The fringe frequency measurement relies on a sub-pixel determination. Considering an uncertainty of 0.5 pixel (probably overestimated) the resulting uncertainty depends on the fringe frequency itself and decreases linearly with the droplet diameter. For a 2 µm droplet, this relative uncertainty is about 15%, and it decreases to 1.5% for a 20 µm droplet. The droplet velocity in the x-direction is also deduced from the image circle radius in two consecutive images. Assuming a 1 pixel uncertainty on the image circle radius variation and given the 700 µs time lag between two frames, the relative uncertainty on the x-velocity is about 0.02 m/s (about 20% for a typical velocity of 0.2 m/s). Velocities in the y- and z-direction are determined from the displacement of the image circle centre. These locations are determined by detecting a sub-pixel maximum in a convolution map. Assuming a 0.5 pixel uncertainty, the uncertainty on z- and y-velocity is of order 0.005 m/s (i.e. 10% for typical velocity of 0.05 m/s in those directions). Note that the uncertainties on velocity measurement can be easily reduced by a factor 2 or 4 by increasing the time lag between the frames by the same factor. Other factors that could potentially increase the measurement uncertainty are related to i) the presence of droplet images not perfectly circular after image deformation, ii) image circles partly cut at the edge of the image, or iii) background noise. These uncertainties are

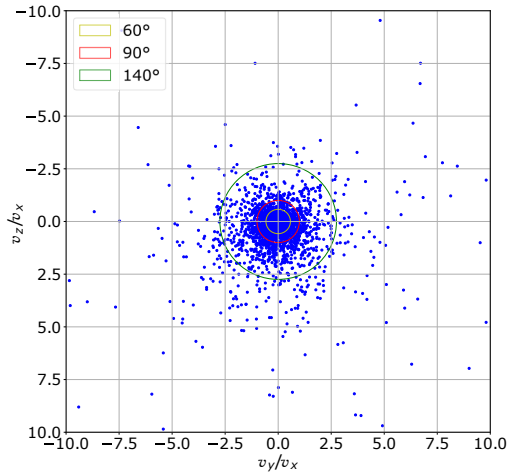

Figure 2.11: Ratios between the spanwise and the streamwise (normal-to-the-mouth) velocity components. The yellow (inner), red (intermediate) and green (outer) circles indicate an aperture angle of the particle cloud of 60°, 90° and 140°, respectively.

more difficult to assess individually. A global estimate of the droplet sizing uncertainty can be provided by the average difference between the droplet size measured in the two consecutive frames (as the same size should be measured for the same particle detected in the two frames). On average, the variation of the droplet size between the two frames, (normalized with the mean size) is about 4%; considering each size class individually, a maximum variation of 8% is observed for droplet size in the range 20-24 µm. Note that the association of droplets from frame 1 and frame 2 is based on the proximity of several measured parameter, including the measured diameter. In other words, a maximum variation of the droplet position and diameter between the to frames is imposed and the maximum allowed diameter variation is set to $(\Delta d/d)_{max} = 20\%$. As a consequence, the previous estimation of (4%) is not totally independent from this criteria but we have checked that it does not vary significantly for reasonable variation $(\Delta d/d)_{max}$ between 10% and 30%.

2.5 Summary and conclusion

In this work, the Interferometric Laser Imaging Droplet Sizing (ILIDS) technique has been employed to determine size and velocity of particles emitted by humans while speaking. ILIDS made it possible to overcome some of the problems encountered in previous works, i.e., i. it is effective in measuring low particle concentrations, as in the case of humans' emission; ii. it allows data collection close to the emission point and thus it minimizes the effect of both dilution and evaporation; and iii solid irregular particles are can be recognized, so that the measures are not affected by dusts naturally present in the air (filtered-air chambers are not needed for the experiments).

Several improvements have been introduced over standard ILIDS in order to widen as much as possible the range of measurable diameters, in particular the smallest ones. In this

way, particle diameters down to $d = 2$ µm and all three components of the particle velocity vector have been measured simultaneously. Besides, the variation of the measurement volume with particle size has been taken into account, making its estimation more reliable than that obtainable using more common measurement techniques based on light sheet illumination.

The main results that can be drawn from our experiments are:

1. The measurement volume increases linearly from 0.2 to 0.4 cm^3 going from d=2 to 10 µm; for bigger particles it remains nearly constant.

2. The particle size distribution – expressed as particle number concentration – shows that most of the detected particles lie in the range 2 - 4 µm in diameter; a relative maximum of particle number concentration occurs at $d \sim 28$ µm.

3. The agreement between our data with the APS measurements carried out by Johnson et al. (2011) via Droplet Deposition Analysis is quite good for particle size between $2 \leq d \leq 10$ µm. In contrast, large differences with the results by Johnson et al. (2011) are observed for bigger particles.

4. The joint probability density functions of particle diameter and velocity components show a clear dependence of the normal-to-the-mouth velocity component on the size, e.g., v_x ranges between 0.1 ms^{-1} for $2 \leq d \leq 2.5$ µm and 0.3 ms^{-1} for $20 \leq d \leq 60$ µm.

5. The emission of the particles from the mouth is far from being unidirectional.

In spite of all its merits, the ILIDS technique has its drawbacks. For example, the size range of the ejected particles is not completely covered as particles smaller than 2 µm cannot be recognized. Some problems occur also for the larger particles, whose scattering diagram may differ from that expected theoretically due to possible inclusions of air (or other substances) or to their not perfectly spherical shape. Another limitation of ILIDS consists in the small field of view area needed to detect the smallest particles. Long measuring time is thus required in order to have robust statistics. The last aspect to be considered is that ILIDS does not work well in case of high droplet concentrations, which would lead to a more likely overlapping of their out-of-focus images. The overlapping of droplet (or irregular particles) images is considered by limiting the fringe analysis to the non overlapping part of the images, but for images that overlap almost completely, the fringe analysis becomes impossible. In the case of speaking or breathing activities the droplet concentrations are relatively low, so that droplet image overlapping occurs rarely and is easily managed. In case of coughing instead, the number of droplet images overlapping increases due to higher droplet concentration. Preliminary tests show that overlapping is still manageable, without changing the optical set-up. In the case of sneezing, however, we estimate that the higher droplet concentration and the larger droplet sizes would require some adaptations of the set-up, to reduce the laser sheet thickness, the out-of-focus level and possibly the collection angle. A development of the present work concerns the use of consolidated techniques and instruments such as FMPS (Fast Mobility

Particle Sizer) and OPS (Optical Particle Sizer), which could be employed to analyze the size range (but not the velocity) of particles not detectable with ILIDS. A partial superposition of the measured size range could be useful also to compare the results. Furthermore, the reliability of the technique to characterise other respiratory activities is worth to be evaluated.

Chapter 3

Simultaneous size and velocity measurements of droplets exhaled while speaking, coughing and breathing

3.1 Introduction

Since the end of the 19^{th} century, the scientific community realised that humans exhale droplets during any respiratory activity. These droplets could contain pathogens present in the airways, constituting a way of disease transmission. The exhaled droplets can contaminate surfaces and objects around the emitter, or they can be inhaled by a susceptible person while they are still suspended in air. The fate of the droplets and the phenomena that they undergo depend on the properties of the droplet-laden air cloud at the emission, whose experimental characterization is of striking importance to quantify the risk and possibly reduce it.

Several studies in the literature provide droplet size distribution for speaking (e.g. Asadi et al. (2019), Chao et al. (2009), Duguid (1946), Johnson et al. (2011), Morawska et al. (2009), Buckland and Tyrrell (1964), Loudon and Roberts (1967), Papineni and Rosenthal (1997), Xie et al. (2009)), breathing (e.g. Asadi et al. (2019), Johnson et al. (2011), Morawska et al. (2009), Almstrand et al. (2010), Edwards et al. (2005), Fabian et al. (2008), Haslbeck et al. (2010), Holmgren et al. (2010), Papineni and Rosenthal (1997)), coughing (e.g. Chao et al. (2009), Duguid (1946), Johnson et al. (2011), Morawska et al. (2009) , Buckland and Tyrrell (1964), Fang et al. (2008), Gerone et al. (1966) , Hersen et al. (2008), Loudon and Roberts (1967), Papineni and Rosenthal (1997), Xie et al. (2009), Yang et al. (2007), Zayas et al. (2012)) and sneezing (e.g. Duguid (1946), Han et al. (2013), Buckland and Tyrrell (1964), Gerone et al. (1966)). The works concerning sneezing are rarer due to the difficulty in artificially inducing this activity. Different protocols have been used for the same respiratory

activity. For instance, Almstrand et al. (2010) tested different levels of airways closure during air expiration to assess the effects on droplet size distribution of different possible droplet formation mechanisms. Analogous tests have been conducted by Holmgren et al. (2010) and Haslbeck et al. (2010). Other researchers focused instead only on the differences between nose and mouth breathing (e.g. Papineni and Rosenthal (1997), Morawska et al. (2009)). To simulate the speaking activity, volunteers were usually asked to count in English (Chao et al. (2009), Duguid (1946), Loudon and Roberts (1967), Johnson et al. (2011), Morawska et al. (2009), Papineni and Rosenthal (1997), Xie et al. (2009)). Asadi et al. (2019) and co-authors investigated the effect of speech loudness and of the language. Concerning the coughing, it must be noted that the coughs are never spontaneous, even if the volunteers are asked to cough as strongly as they can. In addition, both the quantities and the properties of the liquid in the respiratory airways change in the case of healthy subjects compared to subjects presenting symptoms. Among the above-mentioned works, only Fang et al. (2008), Gerone et al. (1966), Hersen et al. (2008) and Fabian et al. (2008) considered not-healthy volunteers.

Despite the great effort devoted by the scientific community in recent years, the measured size distributions of the exhaled droplets is still poorly characterized, with significant discrepancies between data produced in different studies (Seminara et al., 2020; Bourouiba, 2021; Mittal et al., 2020). This has a great importance in improving the knowledge of droplet dispersion process since, as recently highlighted by Rosti et al. (2020), different droplet size distributions at the emission provides completely different results in numerical simulations of droplet dispersion. The reasons for those discrepancies are numerous. One reason is the wide variability among volunteers, so that robust statistic should be considered, even if hard to obtain as consisting in human beigns. Another reason is the complex evaporation process that the droplets undergo after the ejection. Its effect is not easy to predict, due to the complex droplet composition and to its dependency on ambient conditions. Furthermore, droplets move within a turbulent moist hot air cloud that changes its characteristics while dispersing. The further the measuring device from the mouth the more the droplet size considered for the analysis is affected by evaporation. Therefore, the measure should be carried out as closer as possible to the emission point. In addition, the distance of the measuring device from the emission could affect the quantity of detected droplets, due to dilution effects. Another reason for the discrepancy is the wide range of droplet sizes, which span over three orders of magnitude ($o(0.1) - o(100)\ \mu m$). Measurement techniques usually adopted in this field are suitable to detect droplet size only over a limited range. Their efficiency is therefore reduced when applying these over a wider size ranges. Furthermore, each technique implies its own assumptions on droplet properties and is based on different physical phenomena, sometimes providing different size values for the same droplet (e.g. aerodynamic, optical or mobility diameter)(Gralton et al., 2011). Another aspect to be considered is the interference of dusts naturally present in the air. To avoid this latter problem, the measurements are usually carried out into filtered air chambers. Another method consists in using tracer substances, which, however, could affect the measurements (Xie et al., 2009).

Concerning the velocity measurements, several works have been carried out to characterize air velocity, but only a few for droplets velocities. Notable examples of works focusing on the velocity of the air ejected by volunteers while speaking, breathing, coughing and sneezing are Abkarian et al. (2020), Chao et al. (2009), Kwon et al. (2012), Zhu et al. (2006), VanSciver et al. (2011), Nishimura et al. (2013), Tang et al. (2013). Particle Image Velocimetry (PIV) with different kinds of seedings were used, except for Tang et al. (2013) who employed a shadowgraph imaging technique. Gupta et al. (2009) and Gupta et al. (2010), Mahajan et al. (1994) and Singh et al. (1995) measured the airflow rate by means of spirometry. For the breathing and speaking activities, air ejection velocity is of the order $o(0.1) - o(1)$ m/s, while for coughing and sneezing $o(1) - o(10)$ m/s. Droplet velocity has been measured in few works, such as Nishimura et al. (2013), Wang et al. (2020b), Bahl et al. (2020), Bahl et al. (2021), de Silva et al. (2021) for coughing and sneezing activities. Among these, only Wang et al. (2020b) and de Silva et al. (2021) assessed the correlation between droplet size and velocity. Since these works were based on the analysis of on focus images the measurements were possible only for sufficiently large droplets (the minimum detected size is 36 μm in de Silva et al. (2021)). Besides, only the streamwise and the vertical droplet velocity were determined in these works. Even though the droplet velocity is comparable to that of the air, droplets depart from the mouth in a wider angle range with respect to the air. This is also observed in the visualizations by Bourouiba et al. (2014). Besides, from the comparison between droplet and air velocity shown in de Silva et al. (2021), droplets and air share almost the same velocity only at the beginning of the cough and sneeze.

The aim of the present work is to measure size and velocity of droplets ejected by humans while speaking, coughing and breathing. The corresponding distributions are provided. The velocity is measured for droplets down to 2 μm, extending the size range generally found in the literature. It is worth to note that smaller droplets are also more numerous. As droplet size and velocity measurements are performed simultaneously, the correlation between the two quantities is also assessed. Besides, all the three velocity components are measured. The measurements have been conducted using the Interferometric Laser Imaging for Droplet Sizing (ILIDS). An improved setup with respect to its classical application has been developed. Details concerning the technique are reported in Grandoni et al. (2023). ILIDS overcomes some of the problems encountered in the literature. Namely, it makes it possible i. to carry out the measure close to the volunteers' mouth, reducing evaporation and dilution effects and ii. to distinguish between dusts and exhaled droplets, making air filtration in the testing chamber unnecessary. On the other hand, ILIDS is not suitable for high droplet concentrations and the analysis is limited to liquid spherical particles. A further target of the present work is to assess the effect of surgical and tissue masks on droplet size and velocity distribution and the variability of the results for the same volunteer repeating the experiments many times.

The work is organized as follows. Section 3.2 describes the measurement campaigns and the working principles of measurement technique. Some preliminary considerations are reported in Section 3.3.2, while in Sections 3.3.3-3.3.8 the main results are presented and dis-

cussed. Summary and conclusions are reported in Section 3.4.

3.2 Materials and methods

3.2.1 Measurement campaigns and setup

Two measurement campaigns have been carried out at the Laboratoire de Mécanique des Fluides et d'Acoustique of the École Centrale de Lyon, the first one in May 2021 and the second in November and December 2021. The two campaigns involved 23 volunteers. An improved configuration of the interferometric laser imaging for droplet sizing (ILIDS) is used to carry out the measurements. The equipment for the ILIDS consists in a laser light source, a camera and an optical system. A brief explanation of the ILIDS working principles is given in Section 3.2.2. Preliminary tests have been carried out starting from December in order to choose the proper optical system, to carry out the required calibrations and to develop an in-house image processing software. Quite a long time has been spent to define the setup, due to the rather unusual experiments involving human volunteers, especially when COVID-19 pandemic restrictions were in place.

A sketch of the setup is drawn in Figure 3.1. The volunteer sits on the chair and locates his face in correspondence of the mask. The eyes of the volunteer are completely covered for safety reasons. The height of the chair is adjustable according to the volunteer's height. A hole has been made on the mask in order to leave the mouth uncovered and let the ejected droplets to pass. The laser light is produced by a double pulse Nd:YAG laser (Litron Bernoulli-PIV 200-15, wavelength: 532 nm, pulse duration: 8 ns, power: 2*200 mJ). The laser beam is conveyed close to the volunteer's location by means of a tube equipped with a system of mirrors inside. The laser beam is directed from the ground towards the ceiling. At the exit of the tube the beam passes through a cylindrical lens to create a divergent laser light sheet parallel to volunteer's mouth. At volunteer's mouth height the laser sheet is ~ 10 cm wide. A black panel separates the body of the volunteer from the laser sheet. A double frame camera (Lavision imager sCMOS, 16 bit, 2560x2160 pixel, pixel size: 6.5x6.5 m, sensor size: 16.6x14 mm) and the optical system (two lenses and a diaphragm) are aligned and fixed over a plate. The plate can rotate around three axes so that the optical system and the camera can be positioned horizontally and perpendicularly to the laser sheet. The double frame camera and the double pulse laser are connected to a programmable timing unite (PTU) and to a personal computer in order to be synchronized. As the volunteer speaks and coughs without wearing protection masks during the experiments, he/she is alone in the testing room to ensure COVID-19 safety. The operator is outside the room and can look inside through a window and communicate with the volunteer by means of a walkie-talkie. The computer and the PTU, which control the laser, are also located outside the room. Before entering the testing room, the volunteer is asked to disinfect his/her hands and between one volunteer and the next the mask, the chair and the safety panels are disinfected. Besides, the testing room is ventilated for about

40 minutes. Before starting the test all the needed instructions are given to the volunteer.

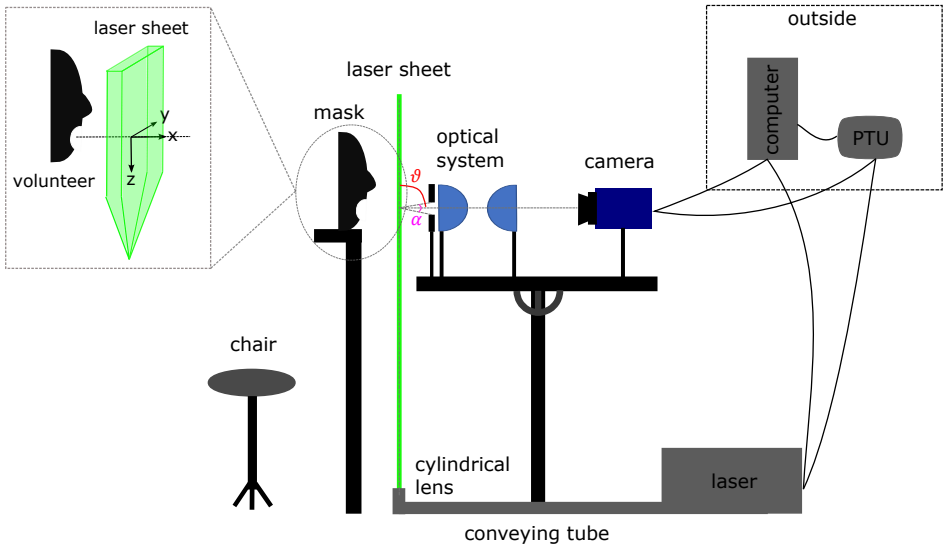

Figure 3.1: Sketch of the experimental setup. The volunteer sits on the chair and locate his/her face in correspondence of the mask, whose mouth is open to let the exhaled droplet pass. The laser light is conveyed by means of a tube close to the volunteer. The laser light passes through a cylindrical lens forming a laser light sheet parallel to the volunteer's mouth. The optical system and the camera are located on a rotating plate. The angle formed between the laser sheet and the axis of alignment of the optical system and the camera is the observation angle θ. The angle that forms between an observed droplet and the effective lens aperture is the collection angle α. The laser and the camera are connected to a programmable timing unite (PTU) and to a personal computer to be synchronized. The computer and the PTU are outside the testing chamber, together with the operator for COIVID-19 safety reasons.

Three respiratory activities are investigated in the present work, i.e. speaking, coughing and breathing. Speaking and coughing while wearing tissue and surgical masks are also assessed. For each respiratory activity a precise protocol is fixed, which limits as long as possible the discomfort of the volunteers. To simulate speaking activity each volunteer performed ten tests, consisting in counting aloud from "one" to "one hundred". The duration of the test is not fixed a priori, but the acquisition is stopped once the counting ends, generally taking about 2 minutes. After each test the volunteer is allowed to take a break and to drink water. Five tests are performed by each volunteer for the coughing activity. During each test the volunteer has to cough for ten times consecutively, starting with mouth closed. It was not asked to the volunteers to cough with the maximum strength, as this would be particularly hard. As well as for speaking, after each test the volunteer can take a break and drink water. For the breathing, ten tests for each volunteer are carried out. The volunteer inspire air through the nose and expire air through the mouth at his/her own frequency for ~ 67 s, corresponding to 1000 images. The same protocol is used for speaking and coughing tests carried out by the volunteers wearing the masks. Furthermore, one volunteer repeated six times the protocols for speaking and coughing (six times the ten speaking tests and six times the five coughing tests) with the aim of assessing intra-volunteer variability.

The protocol, the measurement campaign and the number of available volunteers for each respiratory activity are summarised in Table 3.1.

Table 3.1: Summary of the respiratory activity investigated and the related protocol, number of available volunteers and measurement campaign.

Activity	Protocol	Number of volunteers	Campaign
Speaking	10 tests for each volunteer. Each test consists in counting loudly from "one" to "one hundred". Breaks with the possibility of drinking water are allowed after each test.	20	First (May 2021)
Coughing	5 tests for each volunteer. Each test consists in coughing five time consecutively, starting with mouth closed. Breaks with the possibility of drinking water are allowed after each test.	23	First (May 2021)
Breathing	10 tests for each volunteer. Each test consists in breathing at the comfortable frequency (inspiring through the nose and expiring through the mouth) for about 1 minute (1000 images taken at a frequency of 15 Hz).	3	Second (November -December 2021)
Speaking with tissue mask	Same as speaking but wearing a tissue mask.	3	Second (November -December 2021)
Speaking with surgical mask	Same as speaking but wearing a surgical mask.	3	Second (November -December 2021)
Coughing with tissue mask	Same as coughing but wearing a tissue mask.	3	Second (November -December 2021)
Coughing with surgical mask	Same as coughing but wearing a surgical mask.	3	Second (November -December 2021)
Speaking for intra-volunteer variability	The speaking protocol is repeated by 1 volunteer for six times in different days.	1 (x6)	Second (November -December 2021)
Coughing for intra-volunteer variability	The coughing protocol is repeated by 1 volunteer for six times in different days.	1 (x6)	Second (November -December 2021)

3.2.2 Measurement technique

The interferometric laser imaging for droplet sizing (ILIDS) is used to measure size and velocity of the droplet ejected by the volunteers while speaking, coughing and breathing. The working principles of this technique are reported briefly in what follows.

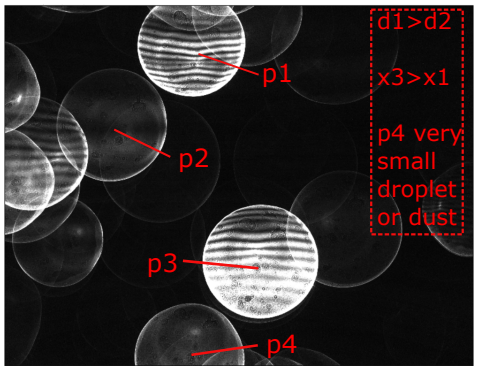

Figure 3.2: Example of acquired out-of-focus image. In the example image, droplets of different size (d) and position within the laser sheet thickness (x) are present. Each circle in the image correspond to a detected droplet. It is evident how droplet size is related to the fringe frequency, while droplet x-position to the circle radius. Some circles without fringes are visible. These are either very small droplets (not measurable) or dusts.

The light scattered by particles passing through the laser light sheet is collected by the optical system and acquired by the camera. The camera is located in such a way that out-of-focus images are obtained, where particles appear as bright circles instead of glare point, as in an on-focus image (Figure 3.2). The circles are a projection of the portion of the particle scattering pattern collected by lenses of circular shape. Hence, neither the shape nor the dimension of the object appearing on the images in correspondence of the particle are in any way related to particle shape and size, but only to the type of lenses employed and to the relative distance between them, the observed particle and the camera. Regular interference fringes are observed within the circles on the images for spherical transparent particles (in this case liquid droplets ejected by the volunteers). The fringes are the result of the interference between the light reflected and refracted by the transparent particle. The spacing among the fringes provides the information on the droplet size, according to the following relation (Eq. 3.1):

$$d = \kappa \frac{1}{\Delta\theta} = \kappa \frac{N_f}{\alpha} \tag{3.1}$$

where $\Delta\theta$ is the angular fringes spacing, N_f is the number of fringes appearing withing the circle and is the collection angle (angle that forms between the observed particle and the lens aperture). The proportionality coefficient k depends mainly on the laser light wavelength λ, on droplet refractive index n and on the observation angle (θ in Figure 3.1). In the present work $k \sim 34\mu m$ degree (water droplets are considered along with $\lambda = 532nm$ and $\theta = 90°$). Note that to measure fringes spacing on the recorded images, at least two fringes must be observable within the circle. As fringes spacing increases for decreasing droplet size, large collection angles

are required to measure the smallest droplets. However, practical problems occur when using large collection angles, namely, spherical aberration effects become important preventing the measure. In this work an optical angle of $\sim$ 45° and $\sim$ 43° is used in the first and second measurement campaign, allowing us to measure droplet sized down to 2 μm. Note that this is an absolute lower limit for the ILIDS, as for smaller droplets the inverse proportionality between droplet size and fringes spacing does not hold anymore. In order to use such large collection angles avoiding spherical aberration effects, a particular optical system is chosen after several tests. Namely, two wide aspherical lenses (Thorlabs ACL7560U, focal length: 60 mm, lenses aperture: 75 mm) in series and a diaphragm which covers the more external part of the lenses are employed. However, this optical system produces images affected by other geometrical aberrations, for whose treatment special software are self-made developed.

Note that solid irregular particles do not show regular interference fringes. Therefore, dusts naturally present in the environment can be easily discerned from droplets ejected by the volunteers, making it unnecessary to carry out the measurement in a filtered air chamber.

The use of a double frame camera synchronized with a double pulse laser makes it possible to measure droplet velocity by evaluating the displacement of the circles corresponding to the same droplet in the two consecutive frames. This measure provides the two velocity components laying in the image plane (y and z directions). In this work also the third velocity component, perpendicular to the image plane (x direction), is determined. As mentioned above, the radius of the circle appearing in the image in correspondence of each droplet depends on the distance between the optical system and the droplet itself. Therefore, the displacement of the droplet within the thickness of the laser sheet can be obtained by measuring the variation of the circle radius between the two frames. Based on geometrical considerations regarding the specific setup used in this work, the following relations can be obtained:

$$\Delta z_{out} \approx -\gamma_1 \, \Delta z \tag{3.2}$$

$$\Delta y_{out} \approx -\gamma_1 \, \Delta y \tag{3.3}$$

$$\Delta R \approx \gamma_2 \, \Delta x \tag{3.4}$$

where Δz_{out} and Δy_{out} are the displacement observed on the out-of-focus image, while Δz and Δy are the related droplet displacements. R is the radius of the circle on the out-of-focus image and Δx is the displacement of the droplet in the direction perpendicular to the image plane and to the laser sheet. The proportionality coefficients have been inferred by means of ad-hoc calibrations. Their values are $\gamma_1 \sim 0.9$ for both the measurement campaigns and $\gamma_2 \sim 0.38$ and 0.34 for the first and the second campaign, respectively. To obtain the velocities, the displacements are finally divided by the time lag between the frames. The time lag varies for different respiratory activities as it must be short enough for the droplet to stay

in the measurement volume and long enough for the droplet displacement to be measurable. Therefore, it is fixed to 700 μs for speaking and breathing and to 50 μs for coughing. The time lag is shorter for coughing, as higher velocities are expected. The acquisition frequency is always fixed at 15 Hz, so that one couple of frames is recorded each 1/15 s.

Differently to what commonly done for measurement techniques involving a laser light sheet, the measurement volume is calculated in the present work. Note that the estimation of the measurement volume is not straightforward, so that usually it is either not considered and only the number of detected droplets is provided, or it is assumed equal to the thickness of the laser sheet. Neither of the two options is exactly correct because the volume where a particle can be detected increases with its size since the light intensity scattered by a particle depends on the square of its diameter. Consequently, larger particles are detectable also at the edge of the laser sheet, where the laser light is weaker. It is worth noting that the light intensity varies within the thickness of the laser sheet, generally following a Gaussian trend. Therefore, the number of detected droplets of different sizes are not exactly comparable if not related to the volume where they can be actually detected. A method to estimate the measurement volume in the ILIDS technique is proposed in Mees et al. (2011). The relation between the circle radius and the position of the droplet within the thickness of the laser sheet is used. Notably, at the end of the image processing, all droplets have been detected and their size and the radius of the circles corresponding to them on the images have been measured. The range of circle radius corresponding to droplets of different sizes can be obtained *a posteriori*, which is related to the range of x positions of the respective droplets and, then, to the thickness of the laser sheet where the droplets can be detected. Multiplying this thickness with the field of view (FOV) area ($\sim$ 2.3 cm^2) the measurement volume is obtained.

More details about the improvements that have been done with respect to ILIDS classical application in order to measure i. droplets down to 2 μm, ii. the third droplet velocity component and iii. the measurement volume varying with droplet size are given in Grandoni et al. (2023).

3.3 Results and discussion

3.3.1 Measurement volume

As explained in Section 3.2.2, the measurement volume varies with droplet size. Its estimate is then required to compare the quantity of droplets detected in different size classes. Besides, droplet number concentrations can be obtained provided the estimation of the measurement volume. The volume can be inferred *a posteriori*, once the size and radius of the circles on the images corresponding to all the detected droplets are known, at the end of the image processing. The circle radii and the respective droplet positions within the thickness of the laser sheet (Eq. 3.4) range in a wider interval for increasing droplet size. In Figure 3.3, the measurement volume obtained for the first and the second measurement campaigns is

depicted. In both the measurement campaigns the volume increases from $\sim 0.2\ cm^3$ to $\sim$ 0.4-0.5 cm^3 for droplets in the range 2-50 μm.

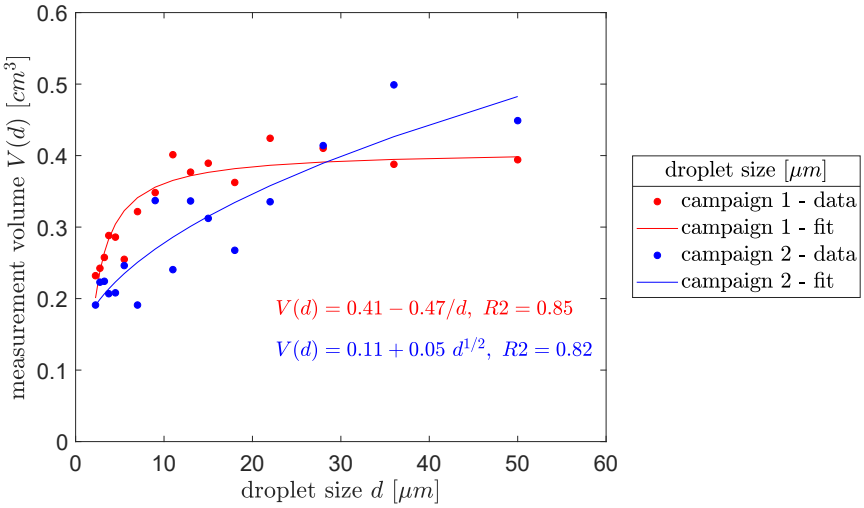

Figure 3.3: Variation of the measurement volume with droplet size inferred for the first (red) and the second (blue) measurement campaigns.

3.3.2 Preliminary considerations about coughing activity

Cough droplets seem to be emitted in high concentrations over a short time, as expected from the nature of the phenomenon. Therefore, few images with high concentrations and many images with low concentrations are observed. Considering the configuration used for the ILIDS and the related image processing, it is possible to manage droplet concentrations up to $\sim 70\ \#/cm^3$, corresponding to ~ 35 droplet per image, with a circle diameter of ~ 800 pixel. Therefore, some of the images with very high concentration occurring in the coughing activity cannot be analysed with the ILIDS, at least for the configuration and processing adopted in this work.

High concentration images do not occur for all the volunteers tested. Particularly, for volunteers 1, 4, 6, 7, 10, 13, 16, 17, 18 high concentration images do not occur at all, for volunteers 2, 8, 11, 15, 3, 12 only rarely, while for volunteers 5, 9, 14, 19, 21, 22, and 23 often. In some cases, the circles appearing in the very high concentration images are not fringed, indicating droplets smaller than the minimum size measurable by ILIDS, i.e. $< 2\ \mu m$. From background dust analysis carried out 30 minutes before and after testing one volunteer it can be excluded that these not fringed circles correspond to dust particles. Volunteers for which very high concentration images contain mainly not fringed circles are 5, 8, 11, 22, and 23.

About 4 % of the images cannot be analysed by the image processing. Excluding the images where droplets are outside the measurable size range (not fringed circles), the percentage is ~ 2.5 %. In these images the detection of the circles cannot be performed well due to their high number. Circles corresponding to the droplets are either badly detected (wrong radius and position) or not detected at all. Nonetheless, badly detected circles are not validated as

droplets in the fringe frequency analysis. Therefore, only few of the total amount of droplets are detected, but their size measurement is correct. Droplets for which an error was made in the validation or size measurement in two of the most critical cases, i.e. volunteers 14 and 19, are 2.3% and 4 %, respectively. For this reason, the results concerning the coughing activity are reported in the followings. However, it is worth to bear in mind that the number of detected droplet is reduced with respect to the total amount.

In future work, several solutions could be tested to enhance the results on coughing activity: modifying the particle detection in image processing by using filters on image intensity values and frequencies, by considering images in a logarithmic scale, instead of linear scale, or experimentally, by reducing the laser sheet thickness in order to reduce the number of particles per image.

3.3.3 Droplet size distribution for speaking, coughing and breathing

In Figure 3.4 a,b,c droplet size distributions measured for the activities of speaking, coughing and breathing, respectively, are depicted. For each volunteer, the size distribution averaged over the tests performed (10 for speaking and breathing and 5 for coughing) is calculated. Then, the size distribution averaged over all the volunteers is obtained and depicted in the figures [1]. The error bar indicates the minimum and maximum values detected among the volunteers.

The distributions are expressed as droplet number concentrations, divided by the width of the size class considered (difference between the logarithmic of the minimum and maximum sizes defining the bin). This kind of expression is commonly used as it makes possible to compare concentrations measured in size classes of different width. In the present case, the bin sizes considered vary between 0.5 and 20 μm. Note also that the use of droplet number concentration instead of droplet number is necessary to compare droplet quantities measured in different size classes as they are detected in a different measurement volume.

Both for speaking and coughing, droplets are detected in the range $2 - 60$ μm, while for breathing the range is reduced to $2 - 8$ μm. The absence of droplets larger than 60 μm is surprising but it is probably due to presence of gas or solid inclusions in the largest droplets that could modify their scattering pattern preventing their identification.

The maximum droplet number concentration occurs between 2 and 2.5 μm for all the respiratory activities investigated. In the speaking the concentration decreases rapidly from ~ 2.25 μm to ~ 13 μm and presents a relative maximum around 28 μm. In the coughing the concentration declines more slowly and almost monotonically with size. We note that the reduced number of large droplets could be due to a lack of statistics. For the breathing the decrease is even slower until the concentration reaches zero for droplet larger than 8 μm. Considerations concerning the shape of the size distributions for the three activities are more evident looking at the cumulative frequency in Figure 3.4d, calculated as the percentage of

[1] Fits of the speaking and coughing size distributions with known functions can be found in Appendix C

concentration of droplets smaller than a given size with respect to the total concentration. The size for which about 50 % of droplets are smaller and 50 % are larger, d_{50}, is greater for coughing than for speaking. This remains true until about d_{87} (87 % of the droplets are smaller than d_{87} and 13 % are larger), but then the cutoff sizes are larger for the speaking due to the relative concentration maximum around 28 μm. The cutoff sizes are larger for breathing than for both speaking and coughing until about 85 and 75 %, respectively.

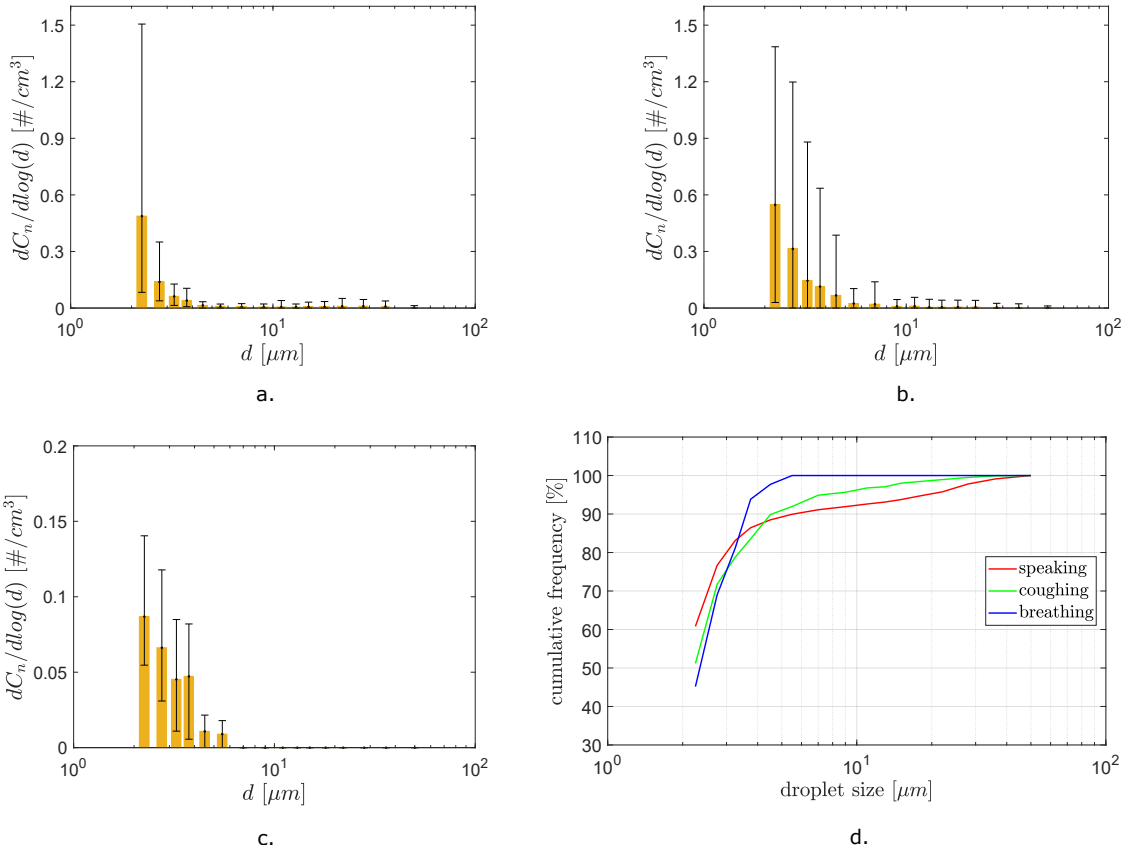

Figure 3.4: Droplet size distributions, expressed as droplet number concentration normalized with the bin size width, measured for speaking(a), coughing (b) and breathing(c). Panel (d) depicts the cumulative frequency of occurrence for the three respiratory activities.

Table 3.2 lists the values of droplet concentrations over all the sizes considering all the volunteers, particularly, the average value among all the volunteers (in brackets, the minimum and maximum values). Note that the number of detected droplets is reduced due to the problems in image processing described previously (Section 3.3.2). Note also that speaking is a quasi continuous process with the protocol adopted here (counting continuously), while volunteers take a break (one or two seconds) between two coughs. In addition, the volunteers were not sick during the test, producing less secretions than symptomatic individuals would do. Despite the possible under-estimation of droplet concentration in coughing, the total droplet concentration measured is higher than for speaking, in turn larger than that for breathing. However, because of the rarer occurrence of coughing with respect to speaking and breathing, the role of the two latter activities in disease transmission should not be excluded, as already pointed out in the literature (e.g. Asadi et al. (2019)) and recognized by the authorities

(WHO; MS).

Table 3.2: Total droplet number concentration for speaking, breathing and coughing (mean, minimum and maximum values obtained among the volunteers).

Activity	C_N tot $[\#/cm^3]$
Speaking	0.0731 (0.0163 ÷ 0.190)
Coughing	0.109 (0.0138 ÷ 0.290)
Breathing	0.0212 (0.00548 ÷ 0.0327)

The measurements show a great variability among volunteers, as already found in the literature (e.g. Chao et al. (2009), Loudon and Roberts (1967), Xie et al. (2009)). The difference between the minimum and maximum concentration is greater than the mean value. Besides, the results of the present work confirm that people emitting more droplets than the average are not the same for different respiratory activities (Asadi et al., 2019). For instance, for coughing the greater emitters are volunteers 14 and 19, while for speaking volunteers 1 and 9 eject more droplets.

In Figures 3.5 a,b,c size distributions obtained for speaking, coughing and breathing are compared with literature data. For the speaking activity the size distributions measured by Johnson et al. (2011), Morawska et al. (2009), Duguid (1946), Loudon and Roberts (1967), Xie et al. (2009) and Papineni and Rosenthal (1997) are considered. In these works, the volunteers count to simulate the activity of speaking, even if slightly different protocols are used. Duguid (1946), Loudon and Roberts (1967), Xie et al. (2007) and Papineni and Rosenthal (1997) droplet number is presented as results, therefore, some assumptions must be done to express the data as number concentration. The procedure proposed by Johnson et al. (2011) is adopted. It is assumed that the volunteers eject on average 7.5 l/min while speaking and that 2 words per seconds are pronounced on average. The concentration is then divided by the bin size considered to make the values comparable. As mentioned in the introduction, the size distributions disagree on the size range where droplets are detected and on the size of maximum concentration. Note that the size range depends on the measurement technique used since there is not any tool that can cover the whole droplet size range. On the other hand, the position and the value of concentration peak is affected by possible dilution and evaporation phenomena. The results obtained in the present work agree well with the distributions presented by Johnson et al. (2011) and Morawska et al. (2009) in the range 2-10 μm. In this range Johnson et al. (2011) and Morawska et al. (2009) use the Aerodynamic Particle Sizer (APS) for the measurements and correct their data accounting for dilution (both) and evaporation (only Johnson et al. (2011)). Data in the present work are acquired close to the mouth so that no correction is applied. For droplets $>$ 10 μm our results differ significantly from Johnson et al. (2011). Namely, our distribution shows a relative maximum between 20 and 30 μm, while in Johnson et al. (2011) concentrations are almost zero. However, this size range coincides with the upper limit of the APS (20 μm) and the lower limit for the

Droplet Deposition Analysis, used by the authors to detect droplets in the range 20-1000 μm. Besides, the efficiency of the APS decreases getting close to its lower and upper limit (see e.g. Morawska et al. (2009)). The other distributions are very different from the ones in the present work, Johnson et al. (2011) and Morawska et al. (2009). Xie et al. (2009) uses an impaction method able to detect only sufficiently large droplets. Loudon and Roberts (1967) and Duguid (1946) employ a combination of two techniques so that they can theoretically detect droplets larger that 1 μm. These works seem to confirm the concentration peak around 100 μm, even if characterized by very different concentration values. However, it must be stressed that the concentrations shown in these cases have been inferred with the above-mentioned assumptions and not directly measured. The results by Duguid (1946) and Loudon and Roberts (1967) seem to support the non-zero concentrations measured in this work around 20-30 μm, even if the distribution by Duguid (1946) should be shifted towards smaller sizes due to a too high correction of evaporation effect according to Johnson et al. (2011).

Concerning the coughing, our results are again compared with those by Johnson et al. (2011), Morawska et al. (2009), Duguid (1946), Loudon and Roberts (1967), Xie et al. (2009) and Papineni and Rosenthal (1997). Droplet number provided by Duguid (1946), Loudon and Roberts (1967) and Xie et al. (2009) are expressed as concentration considering that a volume of 1400 ml is exhaled in one cough (Johnson et al., 2011). Even if an underestimation of droplet concentration was expected due to the problems ilustrated in Section 3.3.2, our results agrees well with the APS measurement by Johnson et al. (2011) and Morawska et al. (2009), at least in the range 2-10 μm. For larger droplets, considerations similar to those reported previously for the speaking activity can be made. Also for coughing a peak around 100 μm is observed in the literature.

For the breathing activity the works by Almstrand et al. (2010), Holmgren et al. (2010), Johnson et al. (2011) and Morawska et al. (2009) are considered. Tidal breathing is assessed in these works , except for Johnson et al. (2011), where a more rigid protocol is used. The main difference between the works in the literature and the present data is the size range of the detected droplets. Literature data demonstrate that droplets far smaller than 2 μm are exahled by humans while breathing, even if they are not detectable with the ILIDS. Considering for comparison only the works by Johnson et al. (2011) and Morawska et al. (2009), whose droplet size range ovelap with the present data, some differences still occur. These are probably due to the evaporation and dilution effects which are not corrected in the two literature works. If the effect of evaporation and dilution were taken into account, the size distributions by Johnson et al. (2011) and Morawska et al. (2009) would have been shifted towards higher concentrations and sizes, getting closer to the present data. In Holmgren et al. (2010) and Almstrand et al. (2010) the evaporation is limited by maintaining almost the same temperature and relative humidity as in exhaled air. Lastly, some differences in the measured size distributions could be ascribable to the slightly different protocol used.

For all the three respiratory activities investigated, speaking, coughing and breathing,

the instruments used in the literature highlighted the presence of droplets smaller than 2 μm, which cannot be detected by the ILIDS. However, it is reasonable to assume that larger droplets are more effective in infection transmission as they can contain a larger number of viruses of a given size (about 100 nm for SARS-Cov 2). This assumpion has been done in several works in the literature, such as Rosti et al. (2020), Buonanno et al. (2020), Wang et al. (2021) and Wang et al. (2022). In particular, the same virus copies concentration measured in the sputum (see e.g. Pan et al. (2020)) is considered for the droplets, irrespective of their size. However, it is worth noting that whether a droplet contains pathogens or not depends also on their actual presence in the zone of the respiratory apparatus where the droplet has formed. To the best of our knowledge, there is no certainty about where particles of different sizes are formed and what the mechanisms of their formation are, even though some works attempt to answer this question (e.g. Morawska et al. (2009) and Johnson et al. (2011)). Besides, it is worth to bear in mind that the risk of infection is rather complex to define as several other factors are involved which are not completely known, such as particle penetrability in the respiratory apparatus, virus inactivation (depending on environmental conditions) and virus dose needed for infection (varying among individuals).

3.3.4 Droplet velocity for speaking, coughing and breathing

Droplet velocity distributions for stream-wise (x), span-wise (y) and vertical (z) components are depicted in Figures 3.6-3.8. The distributions are expressed as frequency of occurrence. For speaking and coughing, five distributions are shown for five different droplet size classes, along with the overall velocity distribution. Differently, for breathing only the overall velocity distribution is shown due to the weak statistic. Note that the statistic available to compute droplet velocity is weaker in general. Thus, the size classes used are wider with respect to the ones considered previously. In fact, only a portion of the detected droplets is present in both the consecutive frames. Some droplets are detected only in the first frame, as they escape the measurement volume in the time elapsed between the frames, or are detected only in the second frame, if they have not yet entered the measured volume when the first frame is taken. If a droplet is not detected in both frames, its velocity cannot be computed. The number of droplets detected in both frames is 3334, 555, 58, with respect to the total amount of detected droplets, i.e. 4842, 853 and 145 for speaking, coughing and breathing, respectively.

The minimum measurable velocity depends on the chosen time lag between the two consecutive frames and on the velocity component considered. For speaking and breathing, a time lag of 700 μs was set, while for coughing the time lag was fixed to 50 μs, as higher velocities were expected. For the span-wise and vertical velocity components, the minimum detectable displacement is $\sim$ 1 pixel, corresponding to $\sim$ 7 μm for both the measurement campaigns, considering a pixel size of 6.5 μm and the coefficient γ_1 in Equations 3.3 and 3.2. Therefore, the minimum span-wise and vertical velocity detectable for speaking and breathing is $\sim$ 0.01 m/s, while for coughing it is $\sim$ 0.1 m/s. The stream-wise velocity component is

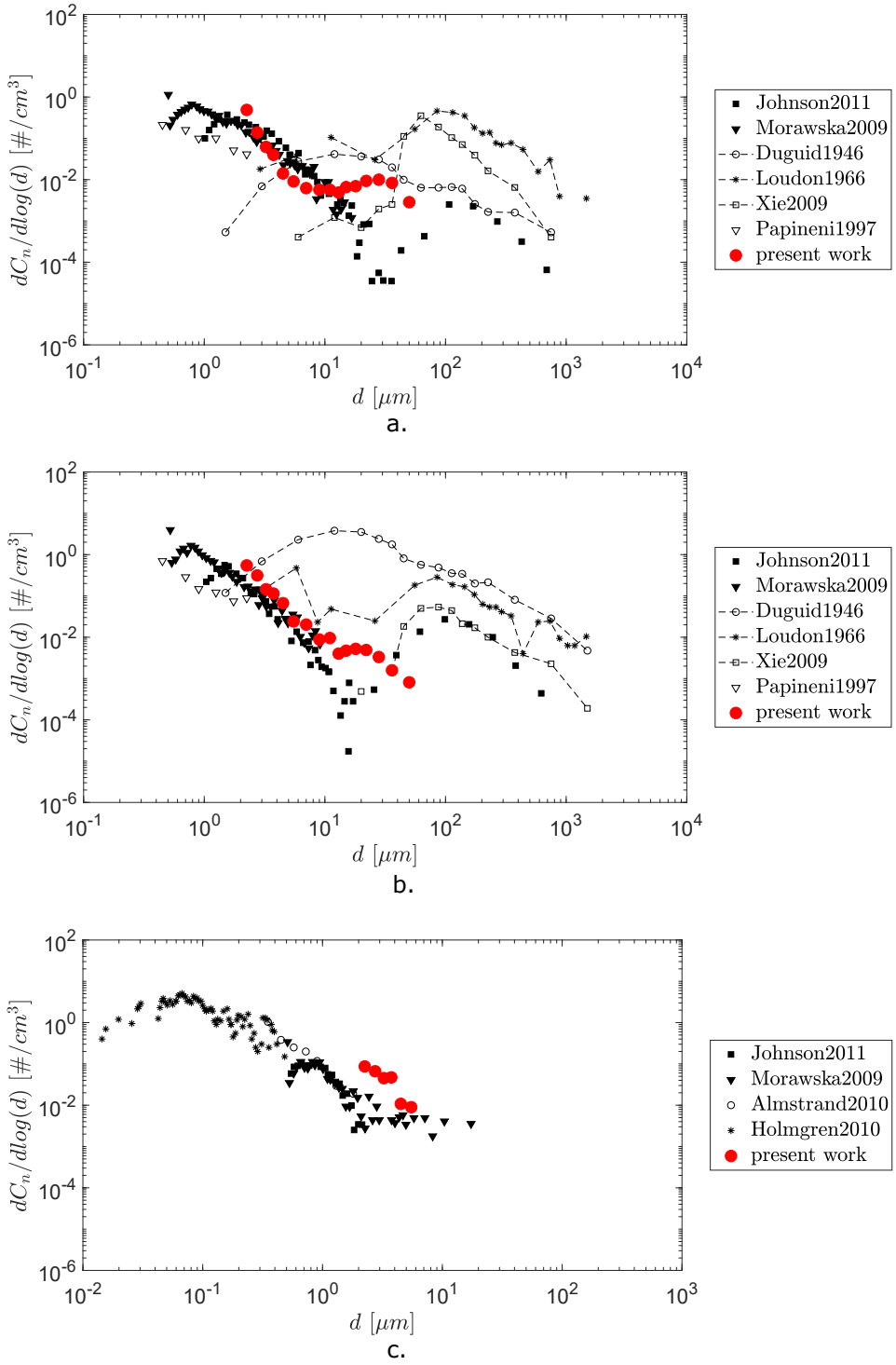

Figure 3.5: Comparison with the literature of the droplet size distributions measured in this work for the activities of speaking (a), coughing (b) and breathing(c).

related to variation of the circle radius corresponding to the droplet in the first and second frame. The minimum detectable circle radius variation is ~ 1 pixel, that is ~ 17 μm and ~ 19 μm droplet displacement in the stream-wise direction for the first and the second measurement campaign, respectively, considering Eq. 3.4 and the coefficient γ_2 calibrated for the two campaigns. Hence, the minimum measurable velocity for speaking (first campaign) is ~ 0.024 m/s, for breathing (second campaign) is ~ 0.028 m/s and for coughing (first campaign) is ~ 0.34 m/s. Bins for the velocity distributions are chosen in agreement with the minimum measurable velocities, namely 0.2 m/s – wide bins are used for speaking and breathing, while 1 m/s – wide bins are used for coughing.

Results for the speaking activity are depicted in Figure 3.6 . The stream-wise velocity component (Figure 3.6a) mainly varies between -1 and 2 m/s (3.68 m/s is the maximum detected value, while the minimum is -1.52 m/s). Velocities > 0 m/s prevails, as expected, as the droplets are ejected from the mouth. Negative values are likely to be due to vortices forming downstream the ejection or to inspiration. The velocity distribution varies with droplet size. Particularly, high velocities become more frequent increasing droplet size. The mean velocity for each size class increases from ~ 0.1 to 0.3 m/s for droplets between ~ 2.25 and ~ 40 μm (Figure 3.6d). The span-wise velocity distribution (Figure 3.6b) is almost symmetric for all five size classes, so that the mean velocity lies around zero (Figure 3.6d). Minimum and maximum measured span-wise velocities are -4.35 m/s and 3.31 m/s. Vertical velocity distributions are slightly asymmetric towards positive values, especially for larger droplets, possibly due to the beginning of the sedimentation. In Figure 3.6d the mean velocity magnitude for the five size classes is also depicted. It ranges between 0.25 and 0.55 m/s for droplet sizes from 2 to 60 μm.

Velocity distributions measured for coughing are about one order of magnitude higher than for speaking (Figure 3.7). The values are mainly between -5 and 20 m/s for the stream-wise velocity component, between -15 and 15 m/s for the span-wise and between -10 and 10 m/s for the vertical. As well as for speaking, the stream-wise component is asymmetric, with prevailing positive values. Mean x-velocity increases from 1 to 4 m/s from 2 to 60 μm-droplets. The mean span-wise velocity is zero on average, as the distribution is symmetric irrespective of droplet size, as expected. For the coughing, the variation of the vertical velocity with droplet size is evident. Namely, the velocity distribution is symmetric and the mean value is about 0 m/s for the smallest droplets, while for droplets of size ~ 12.5 μm the vertical velocity increases, with a mean value reaching 1 m/s. Note that the velocity distribution for droplet in the range 20-60 μm is not represented here, since these results are not reliable due to lack of data. The mean velocity magnitude ranges between 1 and 6 m/s for droplets between 2 and 20 μm.

For the breathing activity (Figure 3.8) the velocities are of same order as for the speaking. As for the other two respiratory activities assessed, the x-velocity distribution is shifted towards positive values, while the other two components are almost symmetric. In this case it is not possible to evaluate the dependency of droplet velocity on their size as only droplets

5 μm are detected in both the frames making possible the measure of the velocity.

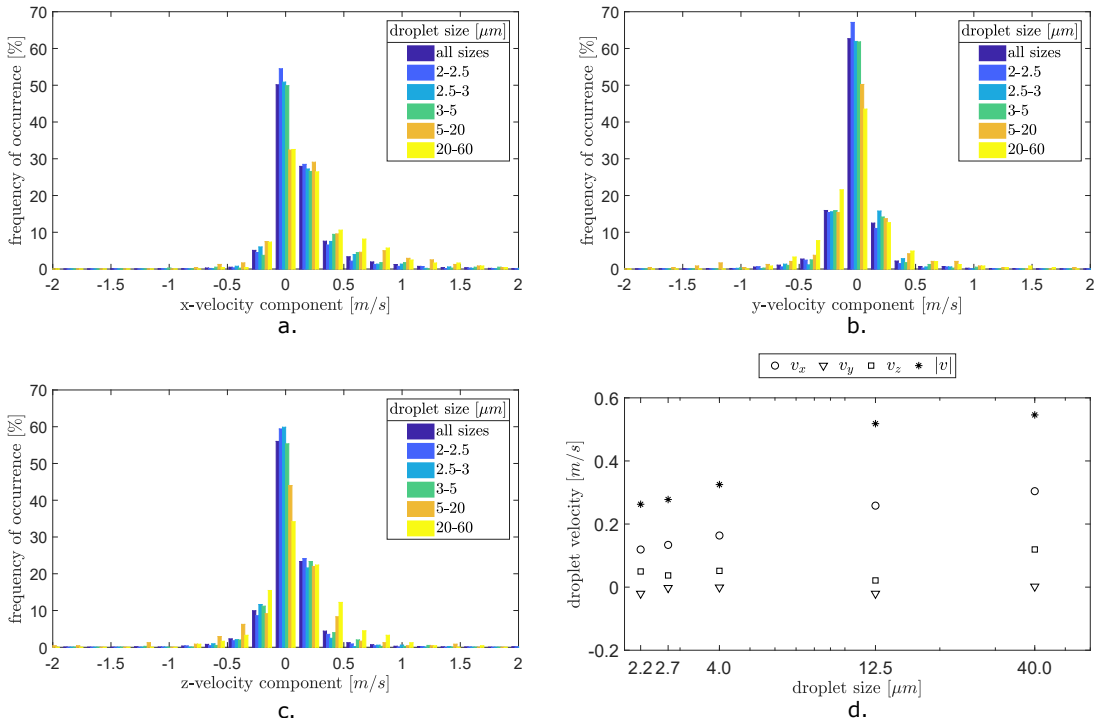

Figure 3.6: Streamwise (a), spanwise (b) and vertical (c) droplet velocity distributions measured for five different size classes and over all the sizes for the speaking activity. Panel (d) depict mean streamwise, spanwise, vertical velocities and velocity magnitude for each droplet size class.

Due to the small number of droplets available for the velocity calculation, it is not possible to assess the variability among volunteers both for the velocity distribution and on mean velocity for the five classes considered. Then, only the overall mean velocity for each respiratory activity is considered. Table 3.3 summarises the overall mean velocity value among the volunteers of the three velocity components and the velocity magnitude. The mean velocity is measured for each volunteer. Then, the average value among the volunteers is calculated (outside the brackets in the table). A measure of the variability among the volunteers is given by the minimum and maximum values of mean velocity detected among them. As already observed, speaking and breathing have values of x-velocity and velocity magnitude of the same order, while coughing presents values about one order of magnitude higher. In all the three activities the y-velocity is about zero. Differently, z-velocity is slightly positive in case of speaking and coughing. As for the size distribution, the variability among volunteers of droplet velocity is larger than its mean value.

Another quantity of interest is the maximum velocity, particularly for the stream-wise component that is responsible for the transport of the ejected droplets further away from the mouth. In Table 3.4 the minimum, maximum and mean value among the volunteers of the maximum x-velocity and velocity magnitude is reported. For the maximum droplet velocity, a greater difference between speaking and breathing is observed. Notably, the former is higher than the latter. Droplet maximum velocity remains the highest in case of coughing activity.

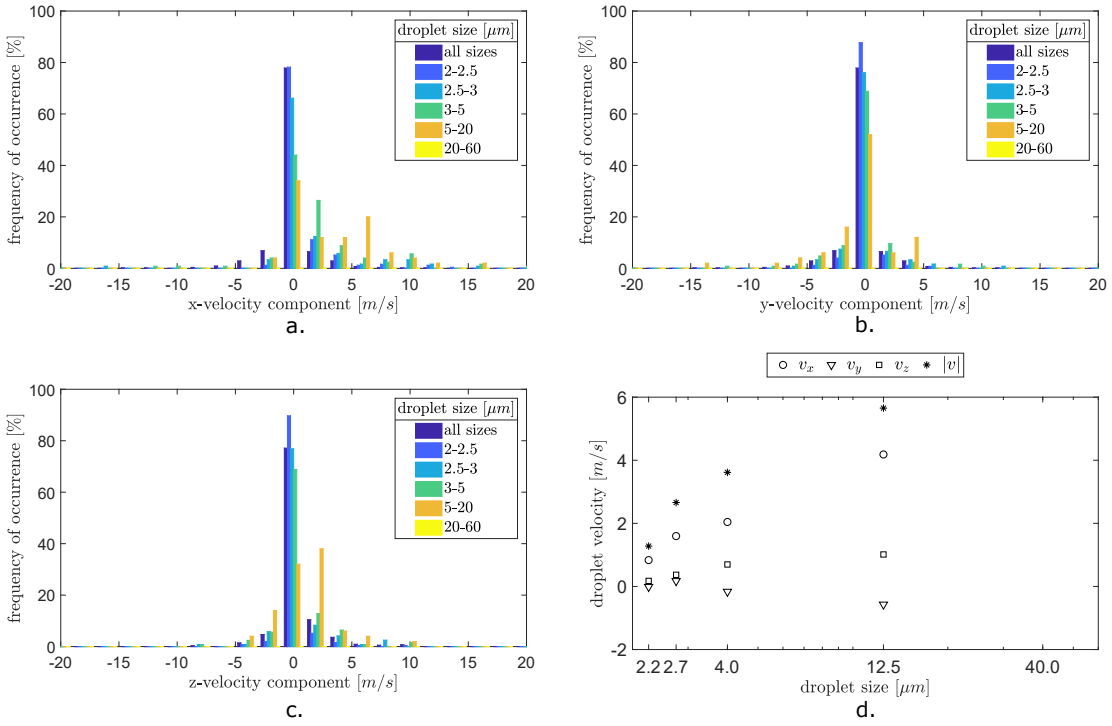

Figure 3.7: Streamwise (a), spanwise (b) and vertical (c) droplet velocity distributions measured for four different size classes and over all the sizes for the coughing activity. Panel (d) depict mean streamwise, spanwise, vertical velocities and velocity magnitude for each droplet size class.

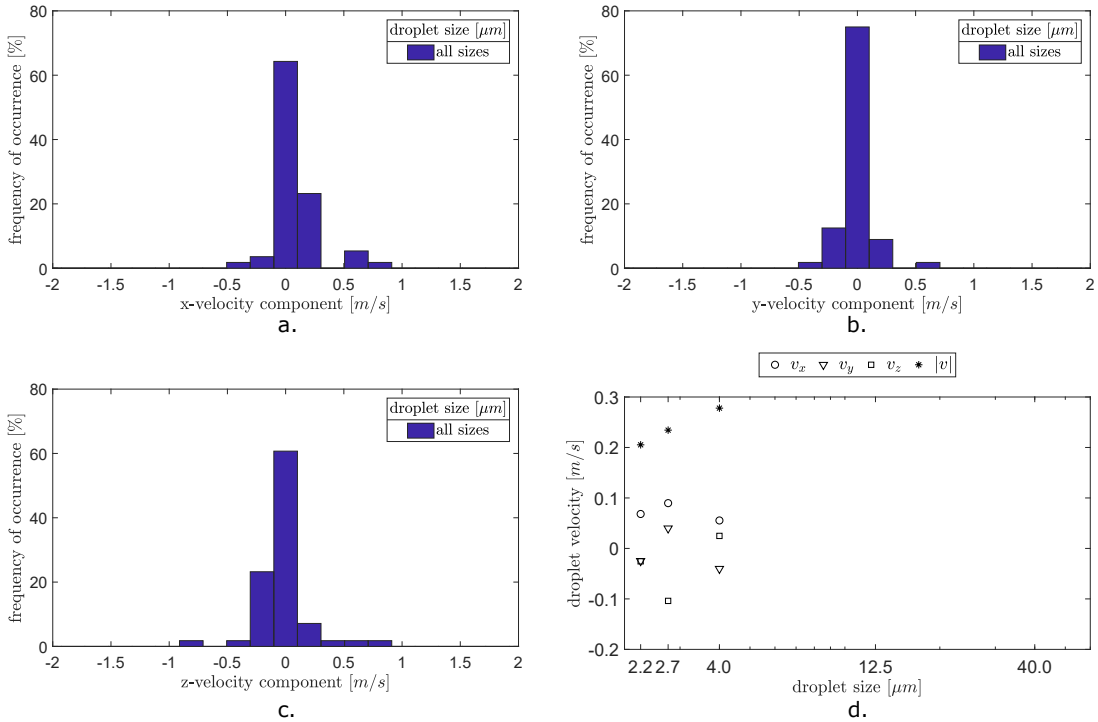

Figure 3.8: Streamwise (a), spanwise (b) and vertical (c) droplet velocity distributions measured over all the sizes for the breathing activity. Panel (d) depict mean streamwise, spanwise, vertical velocities and velocity magnitude for three droplet size classes.

Table 3.3: Mean velocity (average, minimum and maximum values) measured among the volunteers. Namely, the three velocity components and the velocity magnitude are reported).

Activity	v_x [m/s]	v_y [m/s]	v_z [m/s]	$\|v\|$ [m/s]
Speaking	0.162 $(0.047 \div 0.363)$	-0.017 $(-0.240 \div 0.069)$	0.043 $(-0.066 \div 0.200)$	0.326 $(0.179 \div 0.637)$
Coughing	1.68 $(0 \div 6.68)$	0 $(-1.39 \div 0.932)$	0.384 $(-0.381 \div 1.80)$	2.48 $(0.397 \div 8.88)$
Breathing	0.090 $(0 \div 0.147)$	-0.022 $(-0.040 \div 0)$	-0.046 $(-0.074 \div -0.031)$	0.2227 $(0.161 \div 0.281)$

Table 3.4: Maximum velocity (average, minimum and maximum values) measured among the volunteers. The span-wise component and the velocity magnitude are reported.

Activity	v_x [m/s]	$\|v\|$ [m/s]
Speaking	1.81 $(0.831 \div 3.68)$	2.55 $(0.916 \div 4.48)$
Coughing	10.5 $(0.993 \div 28.1)$	11.8 $(1.93 \div 29.0)$
Breathing	0.392 $(0.221 \div 0.713)$	0.735 $(0.388 \div 1.01)$

To the best of our knowledge, there are no measures reported in the literature about droplet velocity regarding for speaking and breathing activities. Therefore, only the velocity measured for the ejected air can be considered for comparison. Abkarian et al. (2020) measured by means of the Particle Image Velocimetry (PIV) technique an average air ejection velocity of tents of centimetres per seconds, with peaks of the order of ~ 1 m/s. Chao et al. (2009) and Kwon et al. (2012) also used PIV and measured a maximum air ejection velocity of ~ 4 m/s. These values are in agreement with the results of the present work, even if they are referred to the gaseous phase instead of the droplets. On the other hand, Gupta et al. (2010) measured a mean air velocity of ~ 4 m/s based on the airflow collected by a spirometer. Similarly, they measured a velocity range of $\sim$ 0.3-2 m/s in the case of breathing activity. Tang et al. (2013) measured a maximum velocity of the ejected air while breathing velocity equal to 1.13 m/s based on shadowgraph imaging technique. More data are available for violent expiratory events, such as coughing and sneezing, as they have been more frequently studied. Examples of maximum air ejection velocities in the coughing activity measured in the literature are 28.3 m/s by Gupta et al. (2009), 22 m/s by Zhu et al. (2006), 13.2 m/s by Chao et al. (2009) and 14 m/s by Tang et al. (2013). VanSciver et al. (2011) found a range 1.15-28.8 m/s for the maximum air ejection velocity for coughing, while Kwon et al. (2012) measured 10.6 m/s and 15.3 m/s for coughing of female and male subjects, respectively. Nishimura et al. (2013) detected velocities higher than 6 m/s. All these values are in agreement with the findings of the present work, taking into account the wide variability among volunteers. In the works

by de Silva et al. (2021) and Wang et al. (2020b) the velocity of the ejected droplets has been measured. de Silva et al. (2021) detected the stream-wise and vertical velocities for droplets ≥ 36 μm. The measured velocity magnitude ranged between 0 and 14 m/s. In the first 0.1 s elapsed from the beginning of the cough the velocity was mostly in the range 8 - 10 m/s, then, the velocity decreases as its mode was shifted between 0 and 2 m/s. Wang et al. (2020b) measured the stream-wise and vertical droplet velocity, for the size ≥ 250 μm. They also detected a decreasing velocity magnitude with time from the starting of the cough. Between 0 and 0.02 s, droplet velocity magnitude is mainly in the range 4-8 m/s. Even though the droplet sizes investigated in Wang et al. (2020b) and de Silva et al. (2021) are not comparable with the ones considered in the present work, the order of magnitude of the measured droplet velocities is in agreement with our results.

3.3.5 Droplet emission in time

Due to the discrete image acquisition (15 Hz sampling frequency) employed in this work, a portion of the ejected droplets is not detected. However, provided the measure of droplet velocity and the estimation of the measurement volume for different droplet size classes, the total number of droplets ejected in time (E) can be inferred, viz.:

$$E = \frac{N_{det}(d)\ v_x(d)}{N_{imm}\ Th(d)} \tag{3.5}$$

where $N_{det}(d)$ is the number of detected droplets, $v_x(d)$ is the stream-wise droplet velocity, N_{imm} is the number of images and $Th(d)$ is the thickness of the measurement volume, i.e. the estimated measurement volume divided by the field of view. Note that $N_{det}(d)$, $v_x(d)$ and $Th(d)$ depend both on droplet size. Notably, mean values of these quantities in five droplet size classes are considered for the calculation. The ratio between $Th(d)$ and $v_x(d)$ represents the time taken by a droplet in a given size class to cross the measurement volume thickness. The estimated emissions E for the five size classes selected and the three respiratory activities considered are presented in Table 3.5.

For the speaking activity the value of 2.3 #/s is reasonable and similar to other results in the literature. The value can be directly compared to the results provided in the work by Asadi et al. (2019). From the results of one volunteer reported as an example one can deduce an emission rate of 0.44 - 3.3 #/s for droplets in the range 2-20 μm; the smallest value is related to the lowest voice amplitude, while the largest to the loudest. Note that the measure is carried out further from the mouth with respect to our measurements. These results agree well with the one in the present thesis. Other comparisons can be performed by considering the total amount of exhaled droplets. Assuming that counting from "one" to "one-hundred" takes about 50 s, the total amount resulting from the estimated emission rate is 115 #. Duguid (1946) measures 230 # for 2<d<75 μm. A value of about 370 # can be deduced from the data by Johnson et al. (2011) for 2<d<1000 μm, considering the measured concentration and assuming an exhaled airflow of 7.5 l/min and a duration of the speech

of 50 s. Note that the measurements by Johnson et al. (2011) are taken further from the mouth with respect to what done in the present thesis, but they are corrected for dilution and evaporation. Therefore, the total amount of exhaled droplets estimated in the present thesis is smaller than the reported literature values. However, the agreement can be considered good, taking into account the assumptions done. Considering that a cough lasts for about 1 s, about 35 # are exhaled in the size range 2-20 μm according to the results in the present thesis. Duguid (1946) reports a total amount of droplets of 3700 # in the size range 2-24 μm, while Johnson et al. (2011) about 112 # in the range 2-1000 μm. The value for Johnson et al. (2011) has been obtained from the measured total concentration of droplets in the size range 2-1000 μm and considering a total exhaled volume of 1.4 l. The discrepancies among data in the literature are, thus, quite large. The emission rate shown for the coughing in the present thesis are underestimated due to the detection problem mentioned in Section 3.3.2. Despite the underestimation of droplet number, in coughing droplet emission is about ten times higher than in speaking and about a hundred of times higher than for breathing.

Table 3.5: Estimation of the total number of droplet of different sizes emitted in time while speaking, coughing and breathing.

	$2 \div 2.5\ \mu m$	$2.5 \div 3\ \mu m$	$3 \div 5\ \mu m$	$5 \div 20\ \mu m$	$20 \div 60\ \mu m$	
Activity	$\#/s$	$\#/s$	$\#/s$	$\#/s$	$\#/s$	$\#/s$
Speaking	1.27	0.33	0.273	0.216	0.223	2.31
Coughing	9.97	8.93	10.1	6.24	-	35.3
Breathing	0.129	0.106	0.0827	-	-	0.317

3.3.6 Droplet ejection direction

Once the stream-wise, the span-wise and the vertical droplet velocities are determined, it is possible to calculate the droplet direction. This is an interesting quantity as droplets do not follows strictly the ejected air cloud, but depart in different directions (Bourouiba et al., 2014; Li et al., 2022).

Droplet direction is expressed in the present work by means of two angles, i.e. β_h and β_v. Taking the stream-wise direction as the reference, β_h is the angle formed between the droplet y-velocity and the reference, while β_h is the angle formed between the droplet z-velocity and the reference (Figure 3.9). The percentage of droplets moving in a given range of directions is reported in Table 3.6. Note that only forwards moving droplets are considered in this calculation. For coughing, about the half of the ejected droplets move within β_h and β_v angles in the range $\pm$ 30 °, while for speaking and breathing the percentage is slightly lower, which suggests that wider spread of directions occur. However, in breathing and speaking most of the droplets move with a range of directions within $\pm$ 70 °. On the contrary, in coughing, a good number of droplets move in a direction that deviates even more from the streamwise direction.

In Li et al. (2022) the cone shape formed in the vertical plane by trajectories of the droplets ejected in a cough is 90 ° wide (β_v within ± 45°). In de Silva et al. (2021) most of the droplets move with β_v in the range 0-60° at the beginning of a cough.

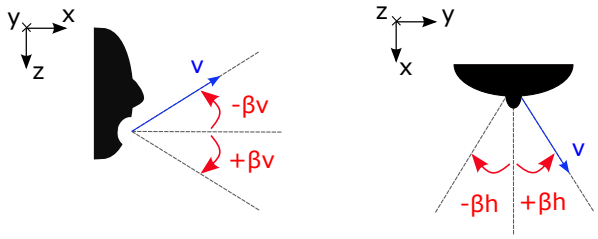

Figure 3.9: Sketch representation of the two angles defining droplet direction.

Table 3.6: Percentage of droplets moving with a direction in a given range defined by the two angles β_h and β_v.

	β_h			β_v		
angle	speak	cough	breath	speak	cough	breath
± 30°	46	48	42	44	49	31
± 45°	65	61	61	61	60	50
± 60°	78	66	78	75	67	67
± 70°	85	69	83	83	67	75

3.3.7 Effects of masks on droplet size distribution and velocity

In Figures 3.10 a-d the size distributions obtained in the tests where the volunteers wear a tissue and a surgical masks for both speaking and coughing activitie are depicted. The size distributions are expressed as droplet number concentration divided by the difference between the logarithms of the size defining each bin (Section 3.3.3). In Table 3.7 the overall mean, minimum and maximum number concentrations measured among the three volunteers tested are listed.

The overall droplet concentration is significantly reduced when wearing a mask with respect to cases where volunteers speak and cough without any protection. The tissue mask reduces droplet number concentrations of $\sim 70\%$ and $\sim 71\%$ for speaking and coughing, respectively, while the surgical mask of $\sim 66\%$ and $\sim 61\%$. It is important to note that the higher filtration efficiency obtained in the present work for the tissue mask with respect to the surgical mask cannot in any way be generalized, since there are not standards for the realization of tissue masks (in other words, each one is different from the others). It is worth noting that the filtration efficiency of the masks varies with droplet size. In fact, in neither of the cases analyzed here droplet larger than 8 μm are detected.

Differently from tissue masks, surgical masks must respect precise standards defined by UNI EN 14683 in Europe. Nevertheless, it is not possible to compare the results obtained here with the European standards, as only bacterial filtration efficiency tests are intended for

surgical masks.

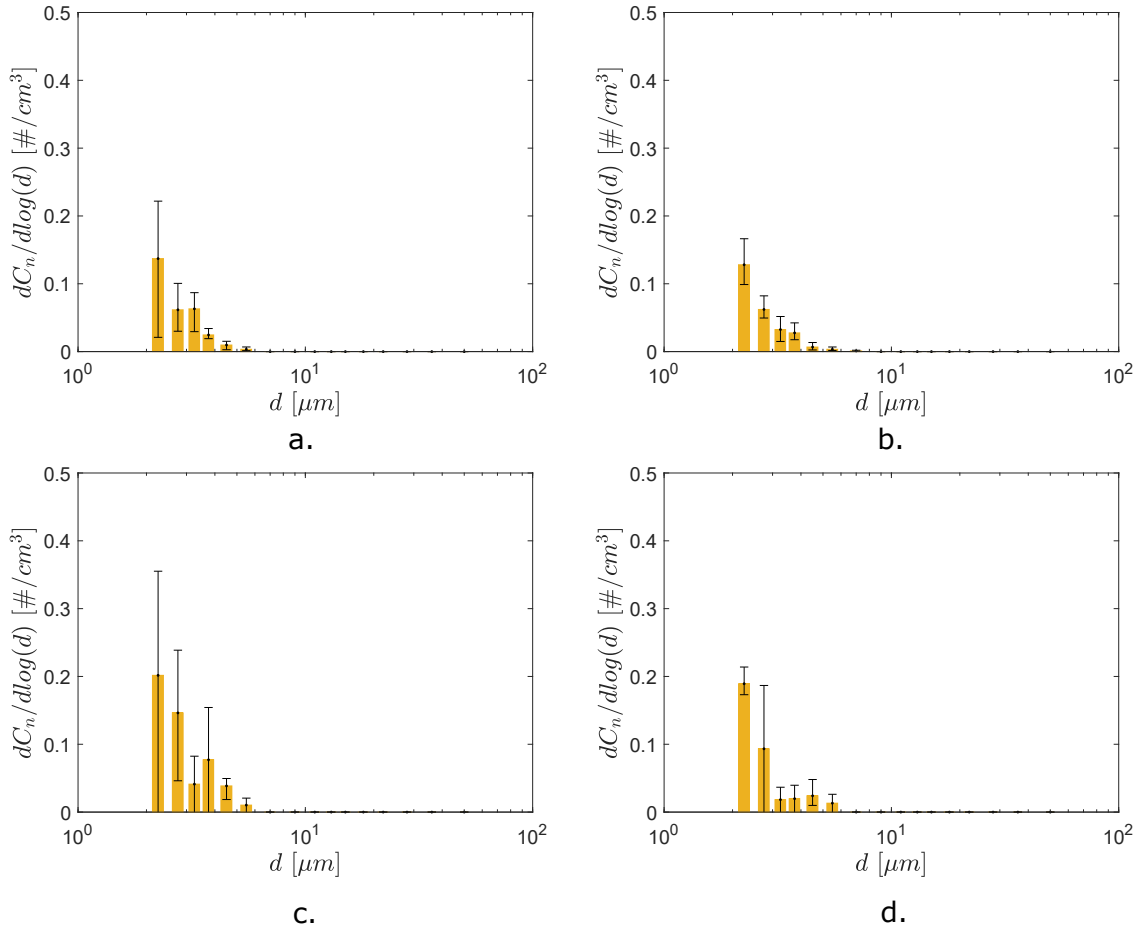

Figure 3.10: Droplet size distribution measured for speaking (a, b) and coughing (c, d) when wearing surgical (left panels) or tissue (right panels) protection masks.

The effect of masks on ejected droplet velocity is also assessed. Analogous results as previously presented for speaking, coughing and breathing are reported in Tables 3.8 and 3.9 for speaking and coughing wearing the masks. The masks are very effective also in reducing droplet velocity, particularly the stream-wise component. The latter, which is responsible for the horizontal distance traveled by the droplets away from the mouth, has a zero-mean value for all the cases considered, except for coughing wearing a surgical mask. Besides, its maximum value (Table 3.9) is reduced of about one order of magnitude irrespective of the type of masks worn.

3.3.8 Variability of ejected droplet size and velocity for one volunteer

The variability of droplet size and velocity distributions among different tests performed by the same volunteer is also investigated in this work. To this aim, volunteer 13 repeated the speaking and the coughing tests for six times.

In Figure 3.11 a,b the size distribution obtained by averaging the data of the six repetitions of volunteer 13 are shown. The error bar indicates the minimum and maximum values obtained

Table 3.7: Total droplet number concentration for speaking and coughing when wearing surgical and tissue protection masks (mean, minimum and maximum values obtained among the volunteers).

Activity	C_N tot $[\#/cm^3]$
Speaking tissue mask	0.0221 (0.0211 ÷ 0.0233)
Speaking sugical mask	0.0250 (0.0119 ÷ 0.0423)
Coughing tissue mask	0.0315 (0.0192 ÷ 0.0449)
Coughing surgical mask	0.0429 (0.0146 ÷ 0.0894)

Table 3.8: Mean velocity (average, minimum and maximum values) measured among the volunteers while speaking and coughing with protection masks. Namely, the three velocity components and the velocity magnitude are reported.

Activity	v_x [m/s]	v_y [m/s]	v_z [m/s]	$\|v\|$ [m/s]
Speaking surgical mask	0 (0÷0)	0 (0÷0)	0.029 (0.022÷0.039)	0.068 (0.052÷0.089)
Speaking tissue mask	0 (0÷0)	0 (0÷0)	0.23 (0÷0.039)	0.065 (0.033÷0.083)
Coughing surgical mask	0 (0÷0.985)	0 (0÷0)	0.153 (0÷0.348)	0.451 (0÷1.10)
Coughing tissue mask	0 (-1.25÷0.991)	0 (0÷0)	0 (-0.351÷0.279)	1.21 (0.507÷2.09)

Table 3.9: Maximum velocity (average, minimum and maximum values) measured among the volunteers while speaking and coughing with protection masks. Namely, the stream-wise component and the velocity magnitude are reported.

Activity	v_x [m/s]	$\|v\|$ [m/s]
Speaking surgical mask	0.237 (0.055÷0.451)	0.440 (0.133÷0.707)
Speaking tissue mask	0.168 (0.053÷0.339)	0.238 (0.072÷0.351)
Coughing surgical mask	0.917 (0÷1.98)	1.04 (0÷2.07)
Coughing tissue mask	2.22 (0.794÷3.96)	5.38 (0.900÷11.1)

among the 6 repetitions. The variability remains still very high among different repetitions performed by the same volunteer. The variability could be related to the day when the measurements have been carried out. Tests 1 and 2 have been carried out on 8^{th} November 2021, tests 3 and 4 on 9^{th} November 2021, finally, tests 5 and 6 on 2^{nd} December 2021. Tests from 1 to 4, performed closer in time, are more similar, while the last two tests differ more from the others. It is not clear whether the variations with the date of acquisition are due to a different condition of the volunteer or caused by different environmental conditions. Further measurements are required to deepen the comprehension of the problem. However, the variaiton of the overall droplet number concentration (Table 3.10) seems to be smaller than the variation among different volunteers (Table 3.2).

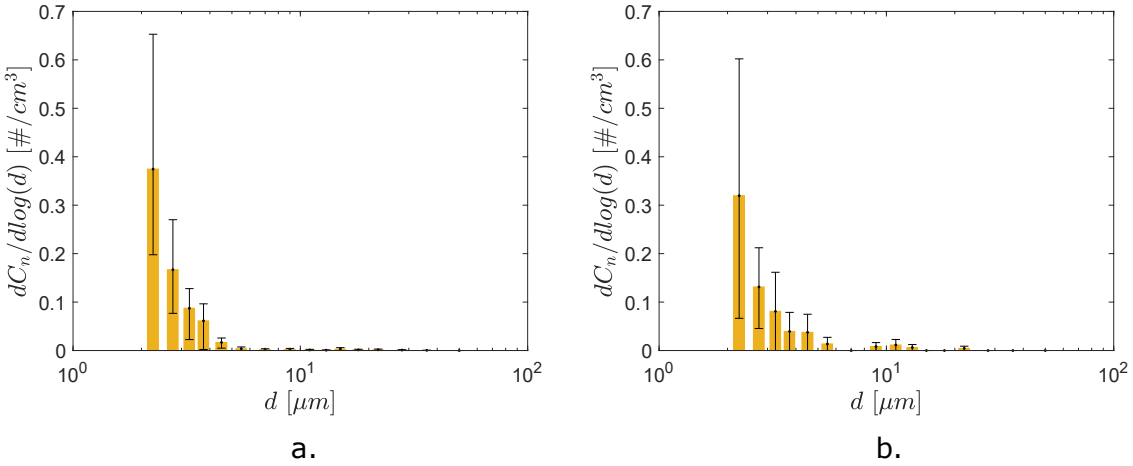

Figure 3.11: Mean, minimum and maximum droplet size distribution measured among the six repetitions of speaking (a,) and coughing (b) protocols performed by the same volunteer.

Table 3.10: Total number concentration (mean, minimum and maximum value) measured among the six repetitions of speaking and coughing protocols performed by the same volunteer.

Activity	C_N tot $[\#/cm^3]$
Speaking	$0.0619\ (0.0254 \div 0.0888)$
Coughing	$0.0562\ (0.0145 \div 0.0950)$

In addition, the droplet velocity variability among different repetitions performed by the same subject seems to be smaller than among different volunteers. Minimum, maximum and average values of mean velocity measured in different tests for the same volunteer are summarised in Table 3.11, while Table 3.12 lists the minimum, maximum and average value of the maximum droplet velocity detected during the experiments.

3.4 Summary and conclusions

In this work, two measurement campaigns involving 23 volunteers have been carried out to characterize the emission of droplets during speaking, coughing and breathing. An improved

Table 3.11: Mean velocity (average, minimum and maximum values) measured among the six repetitions of the speaking and coughing protocol performed by the same volunteer. Namely, the three velocity components and the velocity magnitude are reported.

Activity	v_x [m/s]	v_y [m/s]	v_z [m/s]	$\|v\|$ [m/s]
Speaking	0.110 (0.090÷0.131)	0 (-0.059÷0.033)	0 (-0.081÷0.044)	0.236 (0.205÷0.286)
Coughing	3.36 (0÷5.58)	0 (-2.04÷0.754)	-0.879 (-2.96÷0)	4.86 (0÷8.26)

Table 3.12: Maximum velocity (average, minimum and maximum values) measured among the volunteers while speaking and coughing with protection masks. Namely, the streamwise component and the velocity magnitude are reported.

Activity	v_x [m/s]	$\|v\|$ [m/s]
Speaking	1.09 (0.737÷1.37)	2.04 (1.01÷4.28)
Coughing	12.1 (0÷18.4)	13.3 (0÷20.4)

configuration of the Interferometric Laser Imaging for Droplet Sizing (and of the related image processing) technique has been used to collect the data. Particularly, droplet size and velocity are measured simultaneously for droplets down to 2 μm, extending the knowledge provided by the existing literature. It is worth noting that the simultaneous measurement of size and velocity makes it possible to assess the correlation between these two quantities. Besides, as all the three velocity components are measured, the direction of the droplets can be obtained. The effect of tissue and surgical masks on droplet size and velocity distributions has been also analysed. Lastly, the variability of the results for the same volunteer is tested.

Both for the speaking and coughing activities, droplets are detected in the range 2-60 μm, while for breathing the range is limited to 2-8 μm. The highest concentration occurs for the smallest droplets irrespective of the activity. In speaking, a relative maximum of concentration is observed between 20 and 30 μm. In the range 2-10 μm the size distribution is more scattered for coughing than for speaking, where most of the droplet are in the range 2-2.5 μm. Despite the detection problems faced during the analysis of the coughing data, this activity shows the highest droplet concentration over all sizes. As expected, the lowest concentrations are measured for breathing.

The comparison with the literature is not straightforward, due to the different setup used for the experiments. However, the results is the present work agrees reasonably with those in the literature in the size range 2-10 μm. The absence of droplets above 60 μm in the present work must be further investigated. In the range 10-50 μm the results in the literature differ significantly among them, therefore it is hard to draw reasonable conclusions. Repeating the experiments conducted in the present work using different experimental setup and instrumentations would lead to a better understanding of the problem.

As expected, the velocity of coughed droplets is far higher – about one order of magnitude – than droplets ejected while speaking and breathing. This is particularly true for the

streamwise component, enlarging the possible contamination range further from the emitter. In agreement with the literature, mean droplet velocity magnitude are $\sim$ 0.3 m/s for speaking and breathing and $\sim$ 2.5 m/s for coughing. It is worth noting that the values available in the literature are mainly referred to the velocity of the exhaled air, rather than of the droplets. In all cases, the streamwise velocity is the highest and mainly positive, while the spanwise and vertical components are both positive and negative with an average of $\sim$ 0 m/s. Maximum streamwise velocity detected on average among the volunteers are 1.81, 10.5 and 0.4 m/s for speaking, coughing and breathing, respectively, while the corresponding absolute maximum values are 3.68, 28.1 and 0.7 m/s. Both for speaking and coughing, a correlation between the streamwise velocity of the droplets and their size is observed. Namely, the velocity increases for larger droplets.

As already reported in previous works, droplets depart from the mouth with a wide range of angles, namely about 60 % of the droplets move with a direction that forms an angle of $\pm$ 45° with the axis passing through the mouth centre.

Both for droplet size and velocity measurements, a great variability among volunteers is observed, which is only slightly reduced when considering different tests performed by the same volunteer. However, this last feature requires to be assessed more deeply, in order to understand the possible relation with different environment or volunteer's conditions in the different acquisition lots.

Finally, the tests carried out by the volunteers wearing surgical and tissue masks revealed a strong reduction both in droplet concentration and velocity.

Chapter 4

Numerical dispersion modelling of droplets expired by humans while speaking

4.1 Introduction

The study of the dispersion process of droplet-laden air clouds ejected by humans during different respiratory activities is of major importance for the comprehension of disease transmission involving the airways. In fact, the exhaled droplets can contain pathogens present in the airways of the emitter person. This topic has particularly attracted the attention of the scientific community in recent years due to the COVID-19 pandemic.

After the emission, the droplets undergo different phenomena, i.e., they can settle at the ground, evaporate, and be dispersed by the airflow. Droplets settle more or less rapidly depending on their size. The smallest droplet cannot settle at all and keep on following the airflow. In general, droplet size reduces in time due to evaporation. Some of the droplets can reach their final equilibrium size – varying with ambient conditions – becoming the so-called droplet-nuclei. Depending on the behaviour of the droplets after the emission, they can be responsible for different transmission mechanism, i.e. direct contact, contact with fomites (contaminated surfaces and objects), close (or short-range) airborne and distant (or long-range) airborne (Seminara et al., 2020; Mittal et al., 2020; Asadi et al., 2020; WHO). Transmission via direct contact occurs when a susceptible person touches directly an infected one. Droplets that settle on surfaces or objects are responsible for the second type of contact transmission. Close airborne transmission occurs when the exhaled droplets are directly inhaled by a susceptible person, located close to the emitter, while the distant airborne transmission is associated to the smallest droplets that remain suspended and that are mixed in the air. The risk of distant airborne transmission is higher in closed or semi-closed environments due to weak ventilation and dilution.

Several works – including experiments, simplified models and numerical simulations -

have been carried out to assess the behaviour of the droplets after the emission and to understand if they are responsible for disease transmission of different kind. Abkarian et al. (2020), Bourouiba et al. (2014), Tang et al. (2013), VanSciver et al. (2011), Zhu et al. (2006), Nishimura et al. (2013) and Wang et al. (2020b) carried out real scale experiments, conducted by means of different measurement techniques, i.e., visualizations with high speed imaging, Particle Image Velocimetry, and Schlieren/Shadowgraph imaging technique, in which the volunteers were asked to breath, speak, cough and sneeze. Only in a few real scale experiments the behaviour of the exhaled droplets has been directly assessed, e.g., Bourouiba et al. (2014), Nishimura et al. (2013), de Silva et al. (2021), Li et al. (2022), Bahl et al. (2020) and Bahl et al. (2021). Bourouiba et al. (2014) and co-authors tracked the droplets exhaled in a cough and described their behaviour qualitatively. Nishimura et al. (2013) measured the evolution in time and space of the velocity of the exhaled droplets in the case of a sneeze, i.e., when higher concentrations and larger sizes of the droplets occur. de Silva et al. (2021), Bahl et al. (2020) and Bahl et al. (2021) measured the variation of droplet velocity probability density function between 5 and 25 cm from the mouth in a cough and a sneeze. Lastly, Li et al. (2022) tracked the droplets exhaled in a small area downstream of the mouth and used the results to validate their numerical simulations of a cough. Laboratory experiments, such as the ones performed by Bourouiba et al. (2014), Wei and Li (2017), Liu et al. (2020), consist in reproducing the emission resulting from expiratory activities in a water tank; the density difference between the exhaled and ambient air - due to temperature difference in reality - can be obtained with a salinity difference, while solid spheres of various sizes are used in place of droplets. In simplified models, such as the ones proposed by Bourouiba et al. (2014), Xie et al. (2007), Wei and Li (2015), Liu et al. (2017), Chaudhuri et al. (2020), Wang et al. (2020a), Balachandar et al. (2020), Renzi and Clarke (2020) and Wang et al. (2022), existing jet and puff models are used to describe the airflow, while the droplets are either treated individually by solving their momentum balance equation or globally (in Bourouiba et al. (2014) and Balachandar et al. (2020)) by considering the variation in time of the droplet number concentration within the puff. In Wei and Li (2015), Liu et al. (2017) and Wang et al. (2020a) turbulent velocities are considered and Discrete or Continuous Random Walk models are used for particle motion. Note that in Wei and Li (2015) results from Computational Fluid Dynamics (CFD) are used to account for turbulent velocities. Droplet evaporation is also considered in these works, except for Bourouiba (2020). Many numerical simulations have been carried out to assess exhaled droplet dispersion, mainly in violent expiratory events such as coughing and sneezing (e.g. Li et al. (2022), De Padova and Mossa (2021), Dbouk and Drikakis (2020a), Dbouk and Drikakis (2020b), Busco et al. (2020), Rosti et al. (2020), Abkarian et al. (2020), Wang et al. (2021), Rosti et al. (2021)). CFD makes it possible to afford the complexity of the phenomenon, including the complex evaporation processes strongly affected by ambient conditions and the effects of ambient airflows, of head movement during the exhalations, of time-varying exhalation velocity and of droplet and air ejection spread angle.

Numerical simulations require, however, realistic input data in order to provide reliable

results that can be used in guidelines. Rosti et al. (2020) highlighted this problem by showing the wide variability of the results obtained in their simulations when considering different initial droplet size distributions. Data used as input consist in an initial size distribution for the ejected droplet and an initial exhaled air velocity. Droplet ejection velocity could also be an interesting quantity as it could also affect their dispersion. Indeed, differently to what commonly assumed in numerical simulations and simple models, droplets and air do not share the same velocity at the mouth. Bourouiba et al. (2014) and de Silva et al. (2021) showed that droplets span a wide direction range. Besides, de Silva et al. (2021) observed that droplets have almost the same velocity of the air only at the beginning of a cough and a sneeze.

Even though many works in the literature dealt with this problem, the knowledge still have to be deepened. Droplet size distributions reported in the literature (e.g. Asadi et al. (2019), Chao et al. (2009), Duguid (1946), Johnson et al. (2011), Morawska et al. (2009), Loudon and Roberts (1967), Papineni and Rosenthal (1997), Xie et al. (2007) for the speaking activity) significantly differ due to intrinsic variability among human beings, but also because of the inherent difficulties in measuring (Seminara et al., 2020; Bourouiba et al., 2014; Mittal et al., 2020; Johnson et al., 2011). For example, it is difficult to account for evaporation undergone by the droplet when travels between the mouth and the sampling point, which causes a variation in the measured size distribution. The distance between the mouth and the sampling point also affects the number of detected droplets due to dilution. Furthermore, a wide range of tools has been employed to carry out this measure, which have different sensibilities. Lastly, particulate matter naturally present in the air could interfere in droplet number measurement. Air ejection velocity has been measured by Abkarian et al. (2020), Chao et al. (2009), Kwon et al. (2012) and Gupta et al. (2009) for the speaking activity, but their results also disagree. Gupta et al. (2010) measured by means of a spirometer a mean airflow of 0.8 l/s, which corresponds to a mean velocity of ~ 4 m/s, considering a mean mouth opening of $\sim 1.8\ cm^2$, while Kwon et al. (2012) and Chao et al. (2009) measured by means of the PIV technique 4 m/s as a maximum expiration air velocity instead. Abkarian et al. (2020) measured velocity of tents of centimetres per second on average and peaks of the order of 1 m/s. As above-mentioned. only a few works report velocity of the ejected droplets Nishimura et al. (2013), Wang et al. (2020b), Bahl et al. (2020), Bahl et al. (2021), de Silva et al. (2021) and only for violent expiratory activity (sneezing and coughing). Only in Wang et al. (2020b) and de Silva et al. (2021) droplet size and velocity were measured simultaneously, for quite large droplets ($\gtrsim 30\mu m$) and for two velocity components. A dependency of droplet velocity on their size is found in de Silva et al. (2021).

In this work numerical simulations of droplet dispersion conducted by means of ANSYS Fluent in a semi-closed domain are performed. Namely, the speaking activity is assessed, which is rarely considered in the literature even if asymptomatic disease transmission likely plays an important role for SARS-CoV-2 (Seminara et al., 2020). Input data consisting in droplet size and velocity distributions are provided by the measurement campaign carried out in the Laboratoire de Mécanique des Fluides et d'Acoustique of the Ecole Centrale de Lyon (France)

in May 2021. The experimental technique employed allowed us to measure simultaneously the size and the three velocity components of the exhaled droplets down to 2 μm. Besides, the technique makes it possible to collect data very close to the mouth, minimizing evaporation and dilution effects. Therefore, the effect of the initial velocity on the droplet fate can be assessed. That can be of interest for numerical modellers since most of the models reported in the literature assume that the initial velocity of the droplet coincides with that of the air or be zero. The number of droplets ejected per unit time is also provided by the experiments and that is useful to infer realistic droplet concentrations into the simulation domain. Information about the air ejection velocity is taken by the literature and two extreme values are evaluated. Two ambient temperature conditions, typical of summer and winter temperatures in indoor environments, are also taken into account.

In Section 4.2 the experimental campaign is briefly presented. The numerical simulation setup is also described in detail in this section. The results are presented and discussed in in Section 4.3.

4.2 Materials and methods

4.2.1 Experimental campaign

A measurement campaign involving 20 volunteers has been carried out in the Laboratoire de Mécanique des Fluides et d'Acoustique of the Ecole Centrale de Lyon. In order to simulate the activity of speaking each volunteer counted from "one" to "one hundred" for 10 times. A similar protocol has been adopted by Chao et al. (2009), Johnson et al. (2011) and Duguid (1946). Velocity and size of the droplets exhaled by the volunteers while speaking have been measured simultaneously by using the Interferometric Laser Imaging for Droplets Sizing (ILIDS). With ILIDS the liquid saliva droplets expelled are illuminated by a laser light sheet and, consequently, they scatter light in all directions. A portion of the scattered light is collected by means of a system of lenses and acquired by a camera. The scattered light is characterized by regular interference fringes resulting from the interference between the reflected and refracted light. The spacing among the fringes is inversely proportional to the droplet size. A couple of images – the time lag between the two is set to 700 μs - is recorded by the camera each 1/15 s. The droplet velocity is obtained by evaluating its displacement between the two consecutive images. The working principles of the ILIDS are described in detail in Mees et al. (2011). To make it possible the measure of particle sizes down to 2 μm and all the three velocity components, the technique has been improved with respect to its classical application, along with the related image treatment, as reported in Grandoni et al. (2023). Joint droplet velocity and size probability distributions can be, then, obtained. Since the measurements are not continuous, only a portion of the total amount of the ejected droplets is detected. However, the total number of droplets can be derived from the following

relation:

$$E = \frac{N_{P,det}\ \nu_P}{N_{imm}\ Th} \tag{4.1}$$

where E is the total number of droplets ejected in time, $N_{P,det}$ is the number of detected droplets, v_P is the droplet velocity, N_{imm} is the number of acquired images and Th is the thickness of the measurement volume. Th/v_P is the time taken by the droplets to cross the measurement volume. Since Th and v_P depend both on the droplet size d (Grandoni et al., 2023), different emissions, $E(d)$, for different size classes are first obtained, where the average droplet velocity value for each size class $v_P(d)$ is considered. Then, an average emission rate for all the size classes is calculated. It is worth noting that the emission estimate would not be possible without the simultaneous measure of droplet velocity and size.

4.2.2 Setup of numerical simulations

To assess the dispersion of the particle-laden air cloud ejected while speaking the software ANSYS Fluent is used. In what follows the numerical simulation setup is described.

Gaseous phase (air) The simulation domain is a parallelepiped box 3 m high, 2 m wide and 2 m long (Figure 4.1). The mouth is modelled as a square surface of 0.013 m x 0.013 m. The surface simulating the mouth is located on the left side of the domain at 1.6 m from the ground – the average height of the mouth of a standing person.

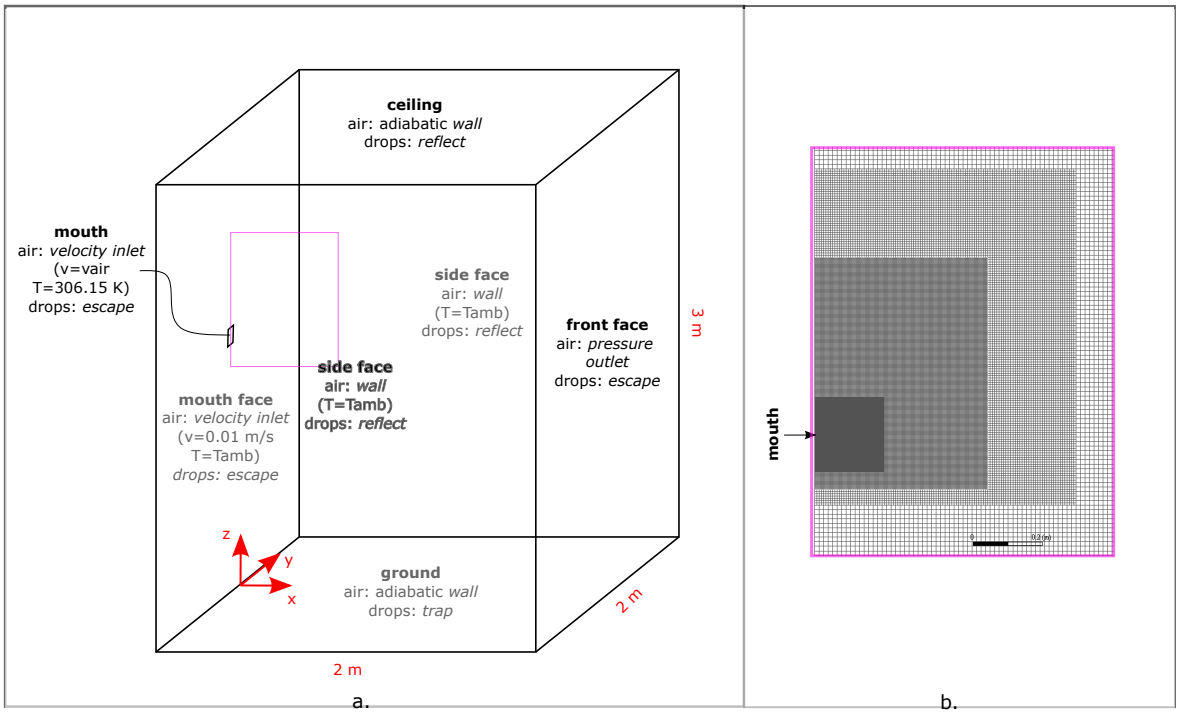

Figure 4.1: a. Sketch of the simulation domain. Boundary conditions for air and droplets are indicated on the respective faces. b. Enlargement of the mesh close to the mouth (pink rectangle in panel a.).

The mesh consists of $\sim$ 9 10^6 hexahedral cells. The maximum cell size is 0.013 m; the

size reduces getting closer to the mouth, so that the minimum size is 3.25 mm (Figure 4.1).

A *velocity-inlet* condition is set at the mouth, from which the expired air enters the domain. The mouth belongs to the "mouth face", on the rest of which a *velocity-inlet* condition (0.01 m/s) is considered. At the face in front of the mouth, hereinafter "front face", a *pressure-outlet* condition is used. At the ceiling, floor and side faces of the domain a smooth-*wall* boundary condition is set. With these boundary conditions a semi-closed space representative of an indoor environment is simulated.

Different buoyancy conditions are analysed by fixing different temperature differences, i.e., density differences, between the exhaled and the ambient air. The temperature of the exhaled air is always set at 306.15 K, while two values of the ambient temperature have been considered, i.e., 293.15 K and 301.15 K, which are the typical winter and summer indoor temperatures, respectively. The ambient temperature is maintained by fixing the temperature of the sidewalls and of the air entering the domain through the "mouth face". The floor and the ceiling are adiabatic. The air density is calculated by ANSYS Fluent through the incompressible ideal gas law (Eq. 4.2):

$$\rho = \frac{P_{op}}{\frac{R}{Mm}T} \tag{4.2}$$

where ρ is the air density, P_{op} is the operative pressure, fixed at 101325 Pa, $R = 8.314\ JKmol$ is the universal gas constant, $Mm = 28.96\ kg/kmol$ is the air molar mass. Note that in this work dry air is considered for both the ambient and exhaled air. Actually, the compositions of the exhaled and ambient air differ and this contributes to the density difference between the two gases. Namely, exhaled air is almost saturated with water vapour and has a higher concentration of carbon dioxide. The former has the effect of lowering the density, while the latter of increasing it. However, the temperature difference effect prevails over the composition difference effect, at least for great temperature differences between ambient and exhaled air (Wei and Li, 2015). If the same composition of the ambient air − 78.084 % of N_2, 20.948 % of O_2, 0.934 % of Ar and 0.031 % of CO_2 (volume percentage) − and a temperature of 306.15 K are considered for the exhaled air, as in the present work, the resulting density is 1.153 kg/m^3. If a realistic composition − 77 % of N_2, 13 % of O_2, 5 % of H_2O, 4 % of CO_2 and 1 % of Ar − and a temperature of 306.15 K are considered for the exhaled air, the resulting density is 1.146 kg/m^3. Therefore, the density difference resulting from the different composition is of 0.007 kg/m^3, which is smaller than the density difference due to the different temperature between exhaled and ambient air. When the ambient temperature is 293.15 K, the ambient air density is 1.204 kg/m^3, so that $\Delta\rho$ = (1.204-1.153) kg/m^3 = 0.051 kg/m^3. Increasing the ambient temperature, the gas composition effect becomes more important, e.g. when the ambient temperature is 301.15 K, the ambient air density is 1.172 kg/m^3, so that $\Delta\rho$ = (1.172-1.153) kg/m^3 = 0.019 kg/m^3.

Despite the process of speaking is highly unsteady due to the variety of phonemes, for sake of simplicity a steady emission of air is considered in this work, using an average air emission

velocity at the mouth, as suggested by Gupta et al. (2010). The steady emission results in a steady turbulent jet exiting the mouth. Abkarian et al. (2020) observed experimentally the formation of a turbulent jet-like flow when multiple words are spoken one after the other. This result is confirmed by Large Eddy Simulations performed by the same author considering a real varying emission of air from the mouth. The approximation of the expiratory flow from speech with a conical quasi-steady turbulent jet is used in the subsequent work of the same authors (Yang et al., 2020).

The values of the air emission velocity measured in the literature are discordant (see Section 4.1). In the present work two cases are considered for the speaking activity, representing the minimum and maximum air emission velocities, i.e., a constant air emission velocity of 0.5 m/s and of 4 m/s. In both cases, the emission velocity is perpendicular to the mouth surface.

The 4 cases, with varying ambient temperature and air ejection velocity at the mouth, are listed in Table 4.1.

Table 4.1: Ambient temperatures and air ejection velocities considered in the four study cases.

	Case I	Case II	Case III	Case IV
T_{mouth}	306.15 K	306.15 K	306.15 K	306.15 K
T_{amb}	293.15 K	301.15 K	293.15 K	301.15 K
v_{mouth}	0.5 m/s	0.5 m/s	4 m/s	4 m/s

Reynolds averaged Navier-Stokes (RANS) equations with a standard $k - \epsilon$ turbulence closure model are used to solve the airflow. Therefore, mass and momentum balance equations along with the equations of turbulence kinetic energy and its dissipation rate are solved. Buoyancy effects are considered for turbulence production term, but not for its dissipation rate. Due to the air temperature difference within the domain, the heat transport equation is also solved. The *pressure-based* solver with *SIMPLE* algorithm is employed. For spatial discretization of all the variables and for the gradients, the default schemes are used (*first order upwind*, *body force weighted* for the pressure and least squares cell based for the gradients). For more details on the equations, on the solver and on the discretization schemes refer to ANSYS (2013).

As convergence criterion 10^{-6} is considered for all the residuals.

Droplets To simulate droplet dispersion ANSYS Fluent *Discrete Phase Model* is used. This is a discrete random walk model in which the momentum balance equation is solved for each droplet to obtain droplet velocity and then, to compute its displacement (refer to ANSYS (2013) for more details). The default value of 0.15 is used for the *time scale constant*, which is involved in the computation of the integral time scale and then, of the eddy lifetime. Unsteady droplet dispersion simulations are carried out and the position of the droplets is recorded each 0.1 s for 1200 s. An uncoupled method is used, so that the gaseous phase transports the droplets by transferring them momentum, but droplets do not affect the fluid

motion. This hypothesis is valid in the real case thanks to the small droplet concentration. The droplets are simulated as spherical, inert water particles (evaporation is not taken into account).

The droplets, which are ejected with the air from the mouth, can rebound elastically on the side walls and on the ceiling (*reflect* boundary condition, with constant *reflection coefficients* equal to 1). They can either escape the domain through the front and the mouth faces (*escape* boundary condition) or be trapped on the floor (*trap* boundary condition). The boundary conditions used for the droplets are listed in Figure 4.1.

Each 0.1 s 1024 droplets are injected into the domain by using an ad hoc injection file. For each injected droplet its initial position, velocity and size are set in order to meet droplet velocity and size distributions measured in the experimental campaign. As the experiments highlighted a link between droplet velocity and size, five different velocity distributions for five different size classes are considered. Droplets of different sizes and velocities are randomly distributed over the mouth surface.

The number of droplets within the domain increases during the first few minutes of simulation. Then, a stationary condition is reached, as droplet injection does not change for the whole duration of the simulation and neither does the airflow. In this work, only the final stationary condition is considered. Nonetheless, unsteady simulations are useful to control the number of droplets ejected per unit time, making it possible to relate droplet concentrations provided by the numerical simulations within the domain to realistic concentrations. In fact, the number of droplets injected in the domain is higher with respect to real emissions in order to obtain good statistics for droplet size and velocity distributions. The realistic droplet concentration and the concentration obtained by means of ANSYS Fluent are related according to Eq. 4.3:

$$C_{real} = C_{sim} \frac{C_{mouth,real}}{C_{mouth,sim}} \tag{4.3}$$

where C_{real} and C_{sim} are the realistic concentration within the domain and the concentration obtained by ANSYS Fluent, respectively, while $C_{mouth,real}$ and $C_{mouth,sim}$ are the corresponding concentrations at the mouth. $C_{mouth,real}$ is given by the droplet emission E divided by the exhaled airflow. Note that the droplet concentration field is computed a posteriori, as ANSYS Fluent does not provide it when uncoupled fluid-discrete phase simulations are performed.

In order to analyse the role played by the initial velocity of the droplets an additional simulation in which it is set to zero is also carried out.

The effect of the initial droplet velocity is also assessed by means of a simplified calculation of droplets settling in a horizontal laminar airflow with velocity $v_a = 0.5$ m/s. Droplets of size d = 1, 10 and 100 μm are injected in the horizontal airflow with initial horizontal velocity $v_{Px,0}$ in the range 0-10 m/s. The droplets are accelerated (decelerated) by the gaseous phase if their initial velocity is lower (higher) than the air until they reach the equilibrium with

the airflow. On the other hand, the droplets are accelerated along the vertical direction due to gravity force until they reach their final settling velocity, v_{TS}. Air (ρ_a) and droplet (ρ_P) density of 1.2 kg/m^3 and 1000 kg/m^3 are considered, respectively. The momentum balance equation along the vertical and horizontal direction is solved for each droplet, i.e. Equations 4.4 and 4.5 (Hinds, 1999):

$$m\frac{dv_{xP}}{dt} = -C_D\ \frac{\pi}{8}\ \rho_a\ d^2\ (v_{xP} - v_{xa})^2 \tag{4.4}$$

$$m\frac{dv_{zP}}{dt} = F_G - C_D\ \frac{\pi}{8}\ \rho_a\ d^2\ v_{zP}^2 \tag{4.5}$$

where m is the droplet mass, v_{xP} and v_{zP} are the horizontal and vertical velocity, F_G is the gravity force, while the rightmost terms in the equations represent the drag force in the two directions.

The drag coefficient C_D depends on the droplet Reynolds number, Re_P. In particular, three motion regimes are identified based on Re_P, viz., i) Stokes' regime for $Re_P < 1$, ii) transition regime for $1 < Re_P < 1000$ and iii) Newton's (or turbulent) regime for $Re_P > 1000$. The corresponding expressions for C_D , valid for spherical droplets, are Eq. 4.6, 4.7 and 4.8 (Hinds, 1999):

$$C_D = \frac{24}{Re_P} \tag{4.6}$$

$$C_D = \frac{24}{Re_P}\ (1\ +\ 0.15\ Re_P^{0.687}) \tag{4.7}$$

$$C_D = 0.44 \tag{4.8}$$

The droplet Reynolds number is calculated as follows (Eq. 4.9) [EQ]:

$$Re_P = \frac{\rho_a\ d\ |\mathbf{v_P} - \mathbf{v_a}|}{\mu} \tag{4.9}$$

where μ is the dynamic viscosity of air.

The momentum balance equation is written for the two directions, horizontal and vertical. Note that the analysis of each component separately is strictly valid only within the Stokes' region. However, the approximation is acceptable for our purposes. The equation is discretized and solved for each time step. As initial condition for droplet velocity, zero velocity is assumed along the vertical, while $v_{P\ x,0}$ for the horizontal direction. At each time, the droplet Reynolds number is calculated and the related expression for the drag coefficient is chosen acordingly. The calculation ends once the droplet reaches its final velocity, i.e., 0.5 m/s for the horizontal component and v_{TS} for the vertical. The terminal settling velocity v_{TS} is calculated by means of an iterative procedure if Re_P exceeds the Stokes' region. The procedure consists in assuming a Stokes' settling velocity as a first approximation, calculating the related Reynolds and drag

coefficient considering the approximated value and, then, using the general expression for v_{TS} along with the Re_P an C_D just calculated; these steps are repeated adjusting from time to time the v_{TS} until it does not change significantly.

4.3 Results

4.3.1 Air motion

The air velocity magnitude and temperature contour plots at the central section of the domain are depicted in Figures 4.2, 4.3 for the four cases listed in Table 4.1. In all the four cases, a stationary jet forms at the exit of the mouth. The jet is initially horizontal near the mouth, where momentum prevails over buoyancy. Then, it bends upwards, as already observed in the experiments by Bourouiba et al. (2014). Ambient air is entrained by the jet causing a reduction of jet velocity and temperature as well as a variation of its buoyancy and momentum. The higher the temperature difference between the ambient and the exhaled air and the lower the air ejection velocity, the closer to the mouth the upward bending of the jet. The effect of buoyancy can be clearly observed in Figures 4.2, where the maps of the velocity magnitude for the four cases are depicted. In case I the exhaled air travels less than 20 cm horizontally, then, it moves upwards and reaches the ceiling at a longitudinal distance from the mouth of about 50 cm. The jet reaches the ceiling with a velocity $\sim$ 0.1 m/s, i.e., about 10 times higher than the ambient. Then, the jet opens close to the ceiling. In case II, qualitatively the same phenomenon occurs, but the jet reaches the ceiling at about 1 m from the mouth and with a lower velocity. In cases III and IV, the jet is mostly horizontal and does not reach the ceiling; it exits the domain through the front face with a velocity that is more than 10 time higher than that of the ambient velocity.

An airflow of $\sim 0.06\ m^3/s$ crosses the domain due to the entrance of air at very low speed through the mouth face. The resulting domain ventilation expressed as number of changes of the domain air volume per hour (ACH), is $\sim$ 18 1/h.

4.3.2 Droplet motion

Measured droplet size and velocity distributions Droplet size and velocity distributions obtained from the experimental campaign and used as input in the numerical simulations are depicted in Figures 4.4 a, b. The droplets detected in the tests of all the volunteers are considered for the statistics. Droplet sizes span the range 2-60 μm and are divided into 16 size classes; in the followings the average diameter d_{mean} of each size class is used for the result description. Most of the droplets lay in the range 2-4 μm, then the droplet number decreases until a relative maximum is observed between 25 and 30 μm. Note that 5 different droplet velocity distributions are used for 5 different droplet size classes (for the sake of brevity in Figure 4.4 b only the streamwise velocity component is shown). In fact, droplet velocity has been observed to vary slightly with droplet size; particularly, the streamwise velocity compo-

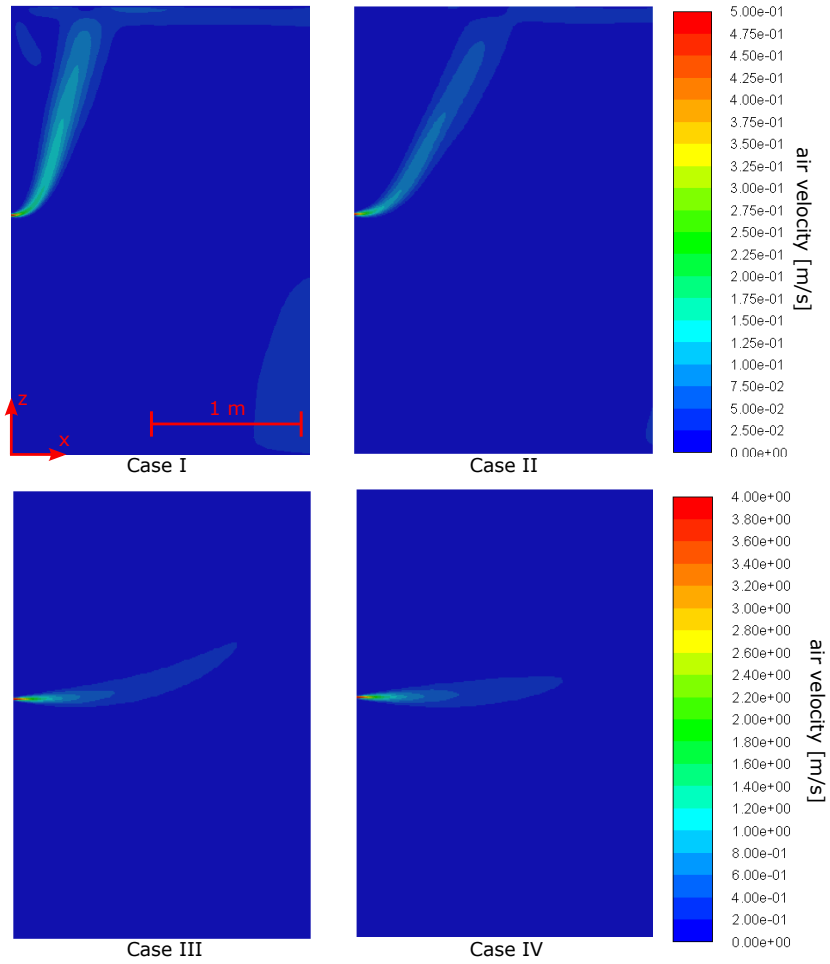

Figure 4.2: velocity magnitude contour plots at the central section of the domain for the four cases.

nent increases with droplet size, while the spanwise and vertical components remain almost similar (about zero on average).

Droplet trajectories In Figure 4.5 the droplet trajectories obtained for the four Cases I-IV once the steady state has been reached are depicted. Note that the figures are representative of a situation where a person speaks for a sufficiently long time with the same ventilation condition of the indoor environment, so that a steady state for both airflow and droplet concentration has been reached. As expected, the smaller and lighter droplets follow the airflow, while larger and heavier droplets fallout from the air jet and settle.

According to the model proposed by Bourouiba et al. (2014), droplets of a given size remain suspended into the air jet until when the jet velocity is greater than the droplet settling velocity. More precisely, droplets continuously fall out, but this simplification is useful to understand why, on average, droplets with decreasing size leave the jet and settle at increasing distances from the mouth.

For case I the largest droplets ($d_{mean} \sim 50\ \mu m$) immediately fallout from the jet, due to the low air velocity. Droplet of size $d_{mean} \sim 36\ \mu m$, instead, initially follow the upward motion of the air jet, but soon fallout and start to settle. Droplets in the size range 18-28 μm

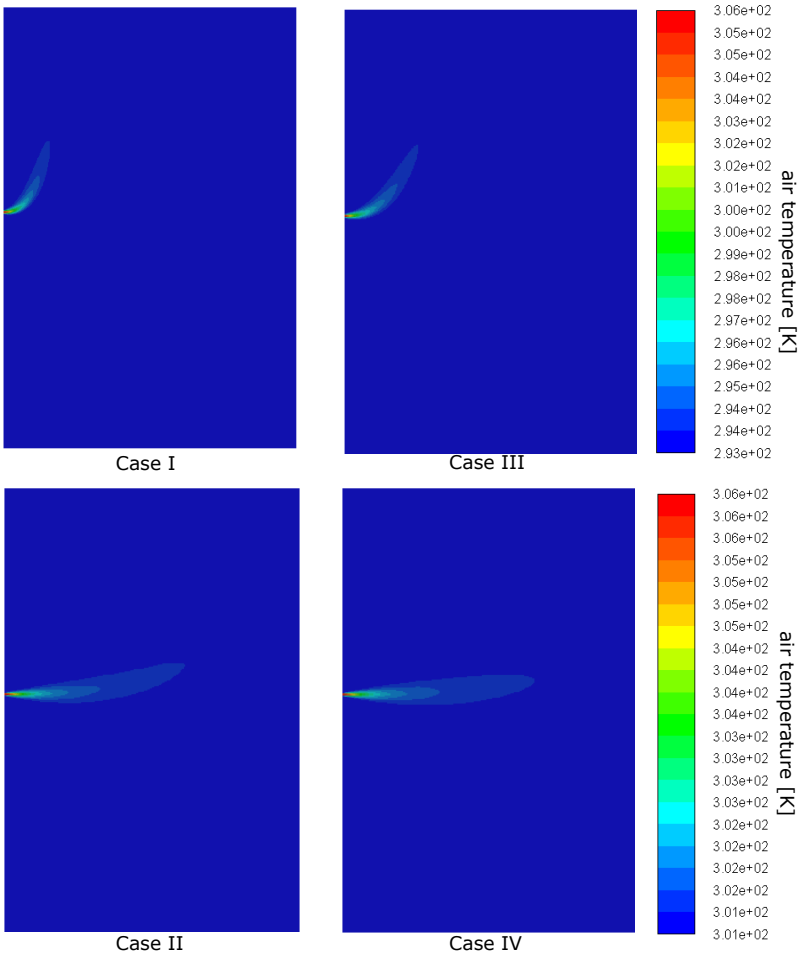

Figure 4.3: As in Figure 2, but for the temperature.

follow the air jet up to the ceiling; then, they move parallel to it for a while (the smaller the droplet size, the longer the traveled distance), until they start to settle. These droplets do not settle completely within the simulation domain but some of them exit either through the front face or through the mouth face. Smaller droplets completely exit the domain through the two open boundaries. In particular, droplets smaller than 8 μm remain close to the ceiling, except the droplets located close to the side walls which move downward due to the interaction with them. The downward motion of the smallest droplets is not observed in case IV, where the air jet does not interact with the ceiling and the side walls. In cases III and IV, where the air injection velocity is higher, larger droplets remain within the jet for a longer distance. Smaller droplets also remain at the mouth height for a longer distance in cases III and IV, as the air jet itself moves almost horizontally. In contrast, in cases I and II, the air jet and the smallest droplets move upward due to the stronger buoyancy.

In what follows, the spanned distances and the related number of droplets that travels them are analysed in detail, along with the concentration of the droplets that remain suspended in the air.

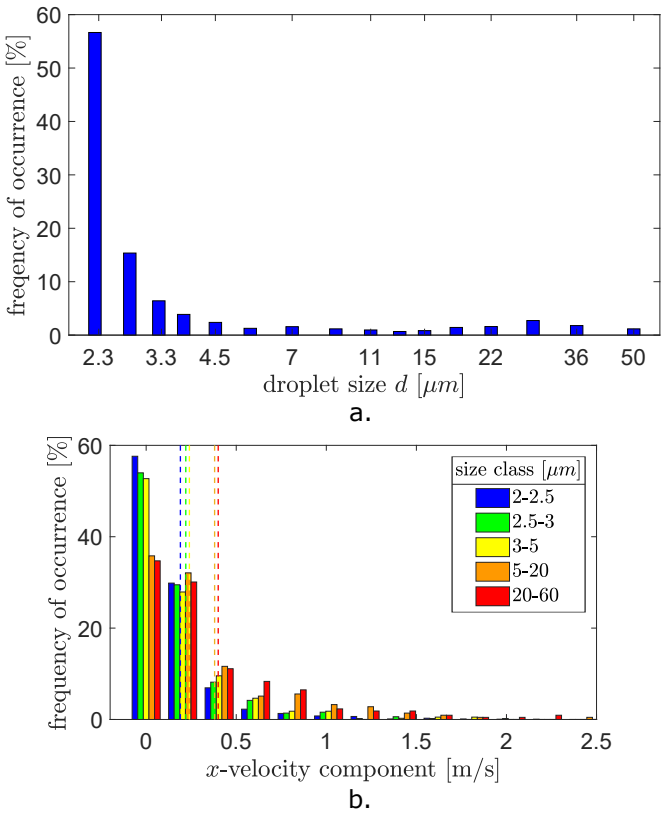

Figure 4.4: Droplet size (a.) and velocity (b.) distributions obtained from the experimental campaign. In the latter five velocity distribution (bars) and mean velocity (dashed lines) for five different droplet size classes are depicted. The data have already been shown in Grandoni et al. (2023), Grandoni et al. (2022)

Distance traveled by settled droplets Droplets that settle at the ground are removed from the air and, thus, they no longer represent a risk for airborne disease transmission. For this reason, most of the works focused on the distances traveled by the exhaled droplets before settling.

In the four panels of Figure 4.6 the floor surface (x,y) and the settled droplets are shown for the cases I-IV. The mouth is located at x = 0 m, y = 0 m. Besides, in Table 4.2 minimum, maximum and mean distances traveled by the settled droplets are reported.

In all the four cases the mean distance traveled by the droplets decreases with increasing size, as expected. However, there are some differences among the four cases, mainly due to the air emission velocity at the mouth.

As seen qualitatively above, in cases I and II, droplets of size $d_{mean} \sim 50\ \mu m$ do not follow the upward movement of the jet, so that they all settle at the ground within less than 50 cm from the mouth. Droplets of size $d_{mean} \sim 36\ \mu m$ partially follow the air jet and, hence, travel longer distances; nonetheless, they are concentrated within 1 m from the mouth. In case I few of these droplets can reach the ceiling and, thus, they settle further; this is not observed in case II since the jet rises more gradually and all the droplets of size $d_{mean} \sim 36\ \mu m$ fallout before reaching the ceiling. Droplets in the size range 18-28 μm span a wide range of distances and a portion of these particles - namely droplets in the range 18-22 μm - settle at a distance

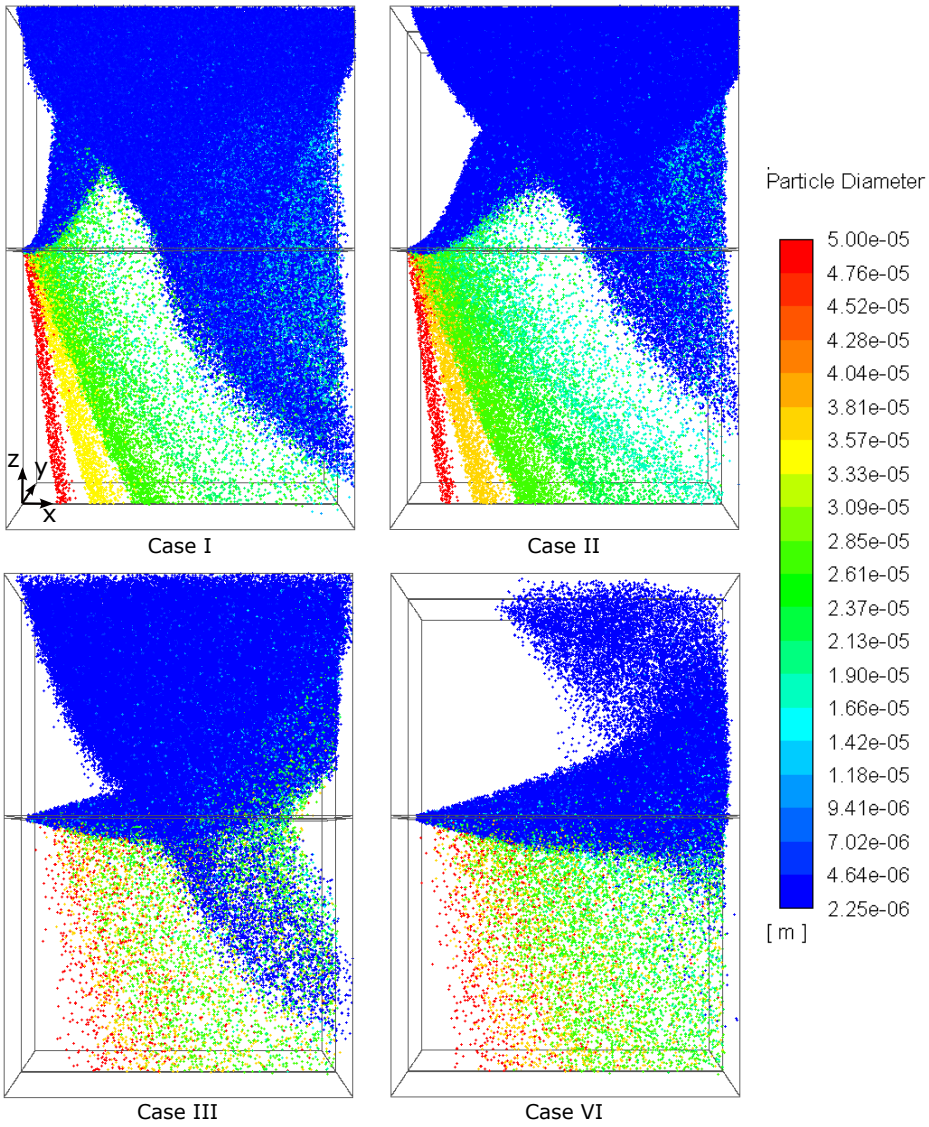

Figure 4.5: Droplet trajectories for the four cases once the steady condition is reached. Colours refer to particle diameter.

longer than the domain length (2 m). Also for the size 28 μm droplets in case II seem to travel a shorter distance. Note that in cases I and II only droplets larger than 18 μm settle at the ground.

The mean distances traveled by the droplets are longer in cases III and IV with respect to the two previous cases. All the droplets of size in the range 22-36 μm settle further than 2 m from the mouth and the distance spanned by the largest droplet is much greater than in cases I and II - between 25 cm and 1.9 m from the mouth in cases III and IV, between 20 cm and 38 cm in cases I and II -. Only droplet larger than 22 μm can be found settled at the ground in cases III and IV. The longer traveled distances in cases III and IV are due both to the higher speed of the air jet which keeps the droplets suspended into it and, also, to the fact that the air jet moves mainly horizontally. There is not a significant effect of the sole ambient air temperature difference on the settling distances between cases III and IV, as well as for cases I and II.

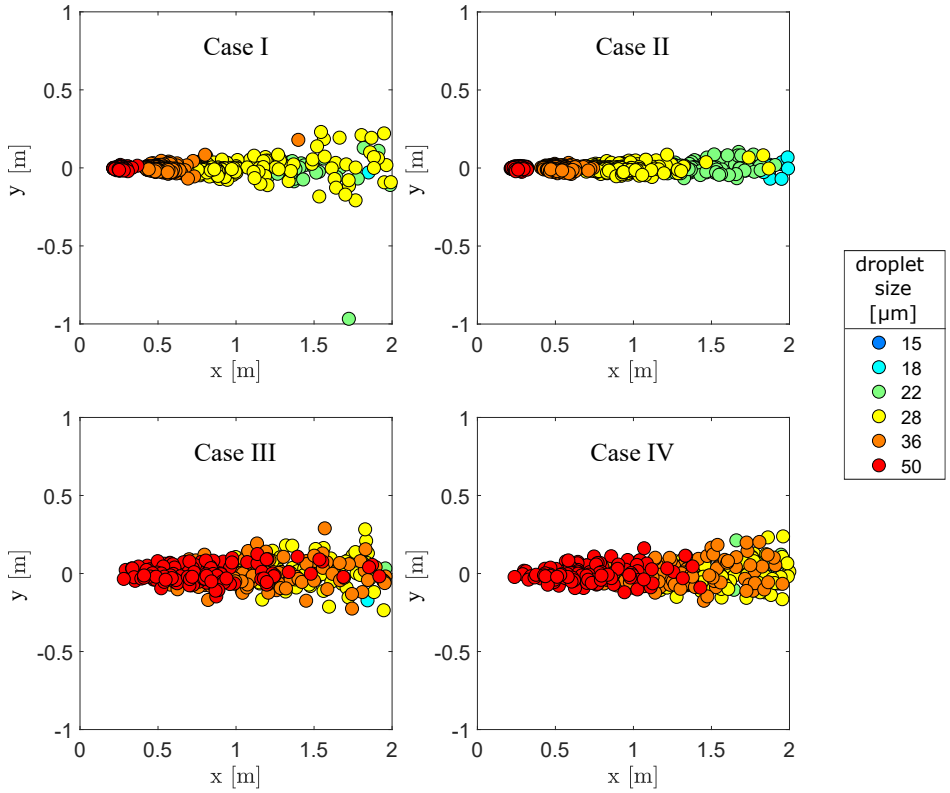

Figure 4.6: Droplets settled at the ground (x,y-plane) in 10 s once the steady condition is reached in the 4 cases. Each circle represents a droplet, while their colour refers to their size.

The reach probability of droplets in the different size ranges depicted in Figure 4.7 provides an idea of the number of droplets that are removed by settling at a given distance from the mouth. This quantity is used also in Wei and Li (2015), Rosti et al. (2020), Wang et al. (2020a). The reach probability (P_{reach}) is defined as (Eq. 4.10):

$$P_{reach}(x) = 100 \; - \; \frac{N_{set}(x)}{N_{inj}} \; 100 \tag{4.10}$$

where $N_{set}(x)$ is the number of droplets settled at the ground at the distance x in a given time interval, while N_{inj} is the number of the injected droplets in the same time interval. Note that once the steady state has been reached, $N_{set}(x)$ and N_{inj} are statistically constants.

In all the four cases, the largest droplets ($d_{mean} \sim 50\ \mu m$) are almost completely removed from the air within the domain (2 m from the mouth). In particular, at 50 cm from the mouth the largest droplets are completely settled in cases I and II, while in cases III and IV these largest droplets are still suspended. Then, their quantity starts to decrease rapidly so that at 1 m from the mouth only $\sim$ 20% of them have not been removed. However, they are suspended in the air – even if in a small quantity – up to 2 m from the mouth. Droplets of size $d_{mean} \sim 36\ \mu m$ are completely removed within 1 m from the mouth in cases I and II, while are still suspended at 2 m from the mouth in a good quantity in cases III and IV – about 40% and 20%, respectively. Droplets of size $d_{mean} \sim 28\ \mu m$ settle all within 2 m from the mouth only in case II. Smaller droplets are only partially or not at all removed by settling.

Table 4.2: Mean and maximum and minimum (in brackets) distances travelled by settled droplets of different sizes in the 4 cases.

	Case I	Case II	Case III	Case IV
size $[\mu m]$	x $[m]$	x $[m]$	x $[m]$	x $[m]$
18		1.862 (1.991 ÷ 1.717)		
22	1.405 (1.988 ÷ 1.160)	1.410 (1.908 ÷ 1.167)	1.669 (1.957 ÷ 1.266)	1.721 (1.966 ÷ 1.240)
28	0.959 (1.992 ÷ 0.687)	0.874 (1.867 ÷ 0.672)	1.402 (1.946 ÷ 0.791)	1.428 (1.999 ÷ 0.673)
36	0.514 (1.399 ÷ 0.421)	0.509 (0.742 ÷ 0.408)	1.112 (1.956 ÷ 0.555)	1.188 (1.955 ÷ 0.445)
50	0.253 (0.368 ÷ 0.213)	0.259 (0.321 ÷ 0.213)	0.770 (1.919 ÷ 0.281)	0.718 (1.429 ÷ 0.238)

Summarizing, a greater number of droplets remains suspended at a certain distance from the mouth when a higher air emission velocity is considered irrespective of the air temperature. In contrast, looking only at the effect of the ambient temperature, when the ambient temperature is higher (cases II and IV) a greater number of droplets is removed by settling at a certain distance from the mouth for all the sizes (except for $d_{mean} \sim 50\ \mu m$ in case II).

Because of the settling of the larger droplets, the size distribution of those that remain suspended in the air vary while moving away from the mouth. Namely, higher frequency of occurrence are observed for smaller droplet sizes. This results in a significant reduction of the suspended mass and, thus, of the potential viral load.

Most of the works in the literature focused on violent expiratory events, such as coughing and sneezing (Bourouiba et al., 2014; Wei and Li, 2015, 2017; Rosti et al., 2020; Busco et al., 2020; Dbouk and Drikakis, 2020a; De Padova and Mossa, 2021; Wang et al., 2020a; Li et al., 2022; Wang et al., 2021). Therefore, it is difficult to compare our results with those reported in the literature. In fact, both sneezing and coughing can be described as a two-stage phenomenon. The first phase occurs during the emission of the droplet-laden air cloud that lasts for less than 1 s and that can be described as a jet. In the second phase, the emission is interrupted and the cloud disperses as a puff (Bourouiba et al., 2014; Wei and Li, 2017). The initial jet is characterized by higher injection velocities with respect to the speaking activity, so that the droplets are transported far away from the mouth. Besides, in the puff phase a quicker decrease of the cloud velocity occurs (Wei and Li, 2015), resulting in a different droplet dispersion process with respect to the steady jet approximating the speaking activity.

Among the works in the literature, Wei and Li (2015) and Wang et al. (2020a) considered in their droplet dispersion simulations a case of stationary jet, even if with higher emission velocity with respect to the present work, i.e., $\sim$ 10 m/s, typical of coughing. In the work by Wei and Li (2015) droplets sized 50 μm reaches longer distances with respect to our case (4 m compared to 1.5 or 0.3 m of the present work), as expected due to the higher jet

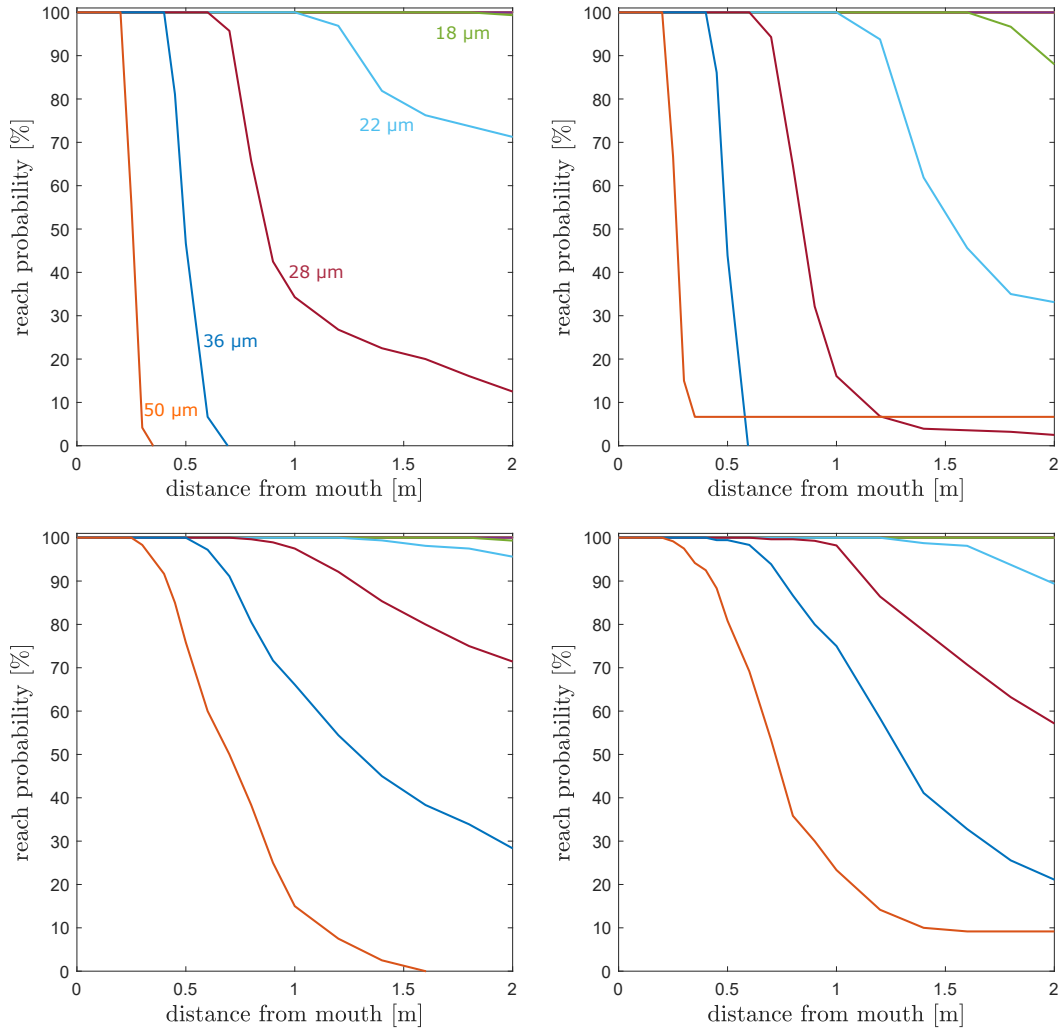

Figure 4.7: In the 4 plots the fraction of droplets with respect to the total injected that are suspended in the air at different distances from the mouth (reach probability) is shown for the 4 cases I-IV; a curve for each droplet size is depicted.

emission velocity and, also, to the absence of buoyancy. Analogous results are obtained in similar conditions – neither buoyancy nor evaporation are taken into account – in Wang et al. (2020a), where droplets of 50 μm are found to travel distances as long as 5 m. In Wei and Li (2015) the spanwise spread of the settled droplets is also provided as a result and it agrees with our work ($<$ 1 m). The spanwise spread of the droplets obtained by Li et al. (2022) in their simulations is in agreement with the results found in the present work, even if a different respiratory activity is assessed.

In the work by Xie et al. (2007) a stationary jet with an emission velocity proper of the speaking activity is considered. According to their model, considering air ejected at 306.15 K, an ambient temperature of 293.15 K, and emission velocity of the air jet of 5 m/s, droplets of about 50 μm travel horizontally for about 0.8 m. For an emission velocity of 1 m/s, droplets of about 30 μm travel about 0.3 m from the mouth, while droplets of about 50 μm travel about 0.2 m. The comparison cannot be carried out for smaller particles as droplets smaller than 30 μm evaporate before falling out from the jet and the complete evaporation distance

is considered as the maximum distance traveled by the droplet. The results obtained by Xie et al. (2007) show slightly smaller distanced with respect to the ones obtained in the present work. This could be probably explained by the fact that there is not spread of the traveled distances, as the effect of turbulence on droplet dispersion was not taken into account in the work by Xie et al. (2007). Furthermore, the mouth surface area used in Xie et al. (2007) is larger than the one used in this work, giving different air jet characteristics. In general, the present work confirms the findings by Xie et al. (2007), for which the horizontally travelled distance is strongly dependent on the initial air jet velocity.

Droplet concentrations Droplets that are not removed by settling, remain suspended in the air and either accumulate into the semi-closed environment or exit it through the two open boundaries. These suspended droplets are a potential risk for airborne disease transmission, which can be direct or indirect (Seminara et al., 2020). The former is due to droplets that move directly from the emitter to the receiving person's mouth, while the latter is due to droplets mixed within the semi-closed environment volume. Safe distances indicated during COVID-19 pandemic are useful to avoid direct airborne disease transmission, which constitutes a major risk due to higher droplet concentrations involved. However, in closed or semi-closed environments some risk remains even further from the emitter person due to possible indirect transmission.

In this section, droplet concentrations within the considered domain volume are analysed.

Figures 4.8, 4.9, 4.10 and 4.11 show droplet concentrations maps calculated along some vertical sections (y-z) of the simulation domain at different downstream distances (x) from the mouth. Here, z is the vertical axis ($0 \leq z \leq 3$ m), while y ($-1 \leq y \leq 1$ m) is the transversal axis (see inset in Figure 4.8; the pink square denotes the mouth position of a possible receiving person, i.e., a standing person as tall as the emitter). The concentration is normalized with that at the mouth and expressed as percentage. Therefore, it is possible to determine a realistic concentration field from the droplet concentration at the mouth known experimentally. The latter can be easily calculated by multiplying the droplet emission rate ($\sim 2.3\ \#/s$) estimated from the experimental data to the ejected airflow (see Section 4.2.2). Although the concentration is expected to vary with droplet size (see the results shown in the previous sections), for the sake of brevity droplets of all sizes are included in the concentration calculation.

If the droplets were completely mixed in the domain, applying the droplet mass balance and considering an air exchange rate of ∼18 1/h (see Section 4.3), the number of droplets in the domain would be $\sim 2\ 10^6$, which would correspond to a concentration in number of $\sim 1.7\ 10^5\ \#/m^3$. Nevertheless, in none of the four cases considered here a completely mixed condition occurs. In case IV (Figure 4.11) the air jet exits the domain almost undisturbed carrying all the suspended droplets. In this case the number of droplets within the domain is smaller than $\sim 2\ 10^6$. In case III the air jet is only partially affected by the presence of the ceiling, so that some droplets accumulate in the upper part of the domain. However, quite a

few droplets are transported outside the domain directly by the air jet, so that the number of droplets within the domain is still smaller than $\sim 2\ 10^6$. In contrast, in cases I and II, the droplets are transported by the air jet close to the ceiling, where accumulate and are not transported outside the domain. Consequently, their number within the domain is about $\sim 2\ 10^6$. Notwithstanding, in the cases I and II a completely mixed condition is not reached either. In fact, one clean and one droplet-laden layer, form into the domain. Only further from the mouth the droplets are mixed along the vertical.

A high concentration zone, possibly responsible for direct airborne disease transmission can be seen in all the four cases. Such zone dilutes and rises due to buoyancy moving away from the mouth. The non-zero concentrations below the mouth height are due to settling droplets. As can be observed in Figures 4.8, 4.9, 4.10 and 4.11, air jet buoyancy plays a key role in removing the droplets from the breathing height. Indeed, the lower the buoyancy effect, the longer the distance for which the high concentration zone persists at the mouth height. Normalized droplet concentration at mouth height as a function of the downstream distance from the mouth is depicted in Figure 4.12 for the 4 cases. As previously seen, both the lower buoyancy and the higher initial air jet velocity cause the persistence of the droplets at mouth height and, therefore, the increase of their concentration. Note that droplet concentration at mouth height does not significantly vary with droplet size. On the one hand, larger droplets are removed by settling, on the other hand, smaller droplets move upwards transported by the air jet.

Effect of the droplet initial velocity In this section, the results obtained setting a zero initial velocity for the droplets are shown. Position and size of the settled droplets are depicted in Figure 4.13, while minimum, maximum and mean distances traveled by them are reported in Table 4.3. There does not appear any significant difference with the results compared to those obtained when the measured droplet velocity distribution is set at the mouth (Figure 4.6). In other words, initial droplet velocity seems not to play an important role in the overall droplet dispersion process.

This result confirms simple calculations that can be done for droplets settling in a uniform horizontal airflow (Section 4.2.2), whose results are shown in Figure 4.14. In the figure the variation in time of the horizontal velocity and position of a 100 μm droplet is depicted (only the plots for 100 μm droplet are reported for sake of brevity). The equilibrium with the gaseous phase (velocity of 0.5 m/s) is reached almost immediately irrespective of the initial droplet velocity. Only for the first fractions of second droplets with higher initial velocity travel longer distances with respect to droplets with zero initial velocity. However, once the equilibrium with the air is reached, the difference in the distance traveled by initially faster and slower droplets remain constant, as all droplets move with the same velocity (0.5 m/s). In Table 4.4 the time needed to reach the equilibrium and the maximum difference in the distance traveled by faster droplets and droplets with zero initial velocity are reported for all the droplet sizes and initial velocities considered here. The time needed to reach the

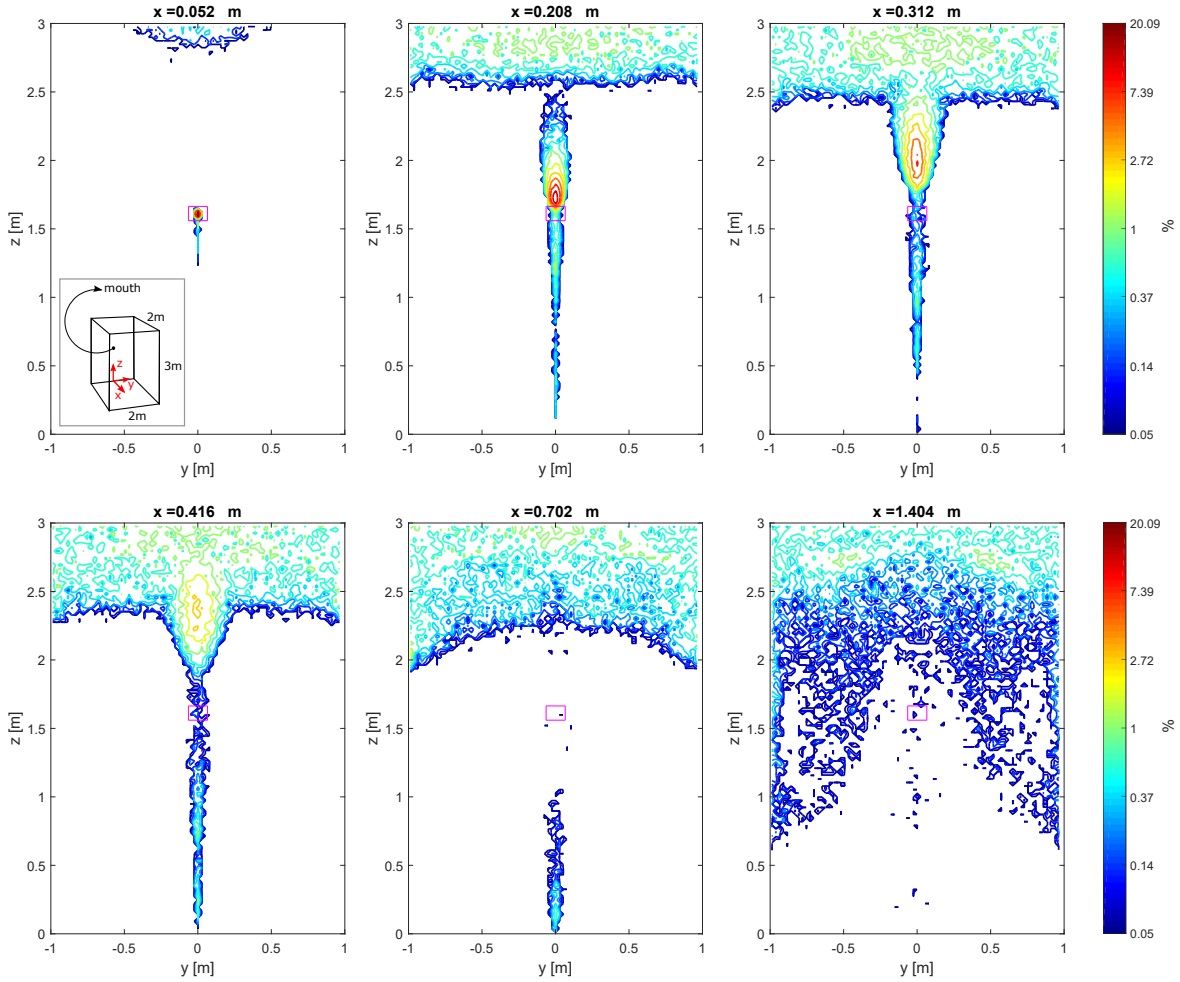

Figure 4.8: Normalized droplet concentration fields within transversal sections at different downstream distances from the mouth obtained for case I; a logarithmic scale is used for colours. The pink square indicates the position of the mouth.

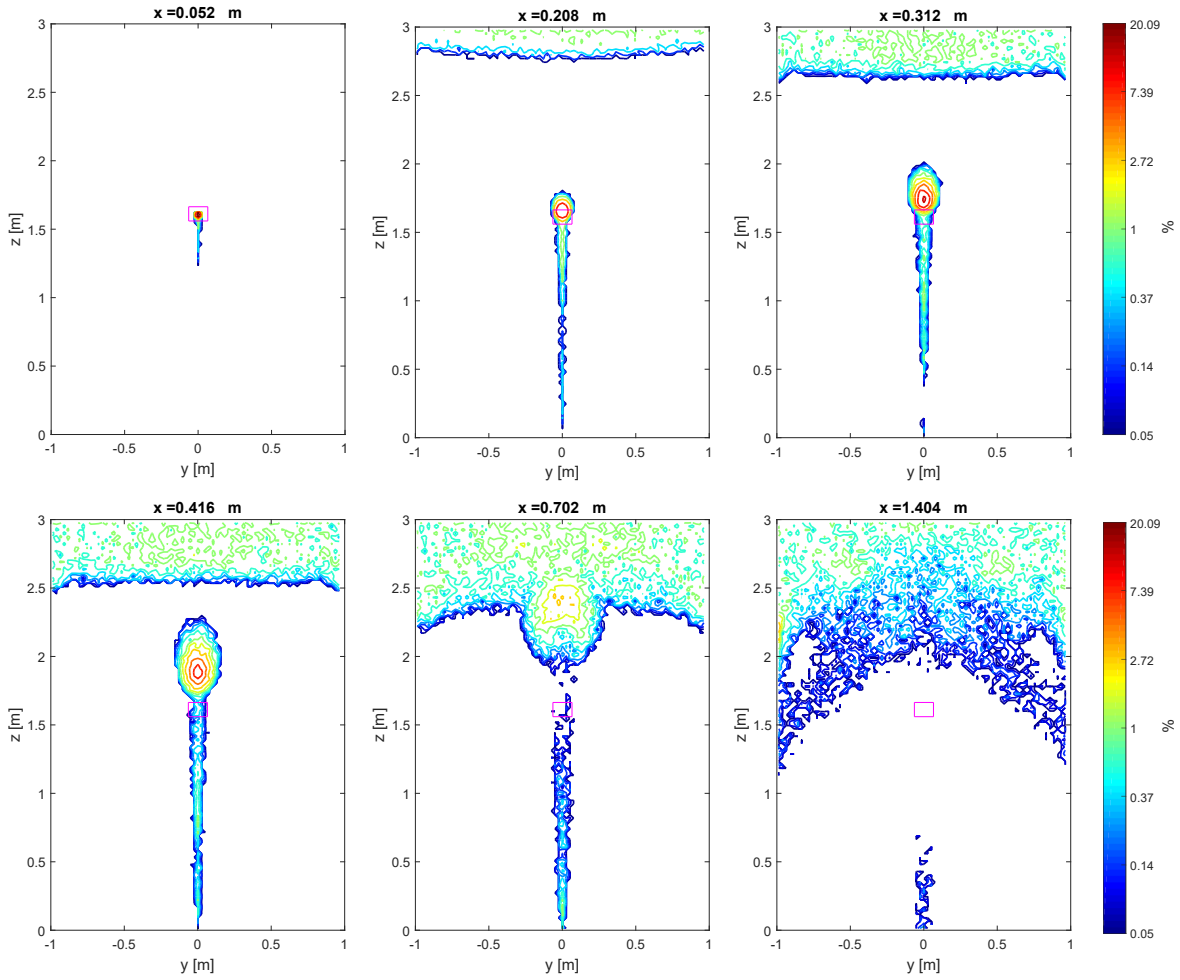

Figure 4.9: Normalized droplet concentration fields within transversal sections at different downstream distances from the mouth obtained for case II; a logarithmic scale is used for colours. The pink square indicates the position of the mouth.

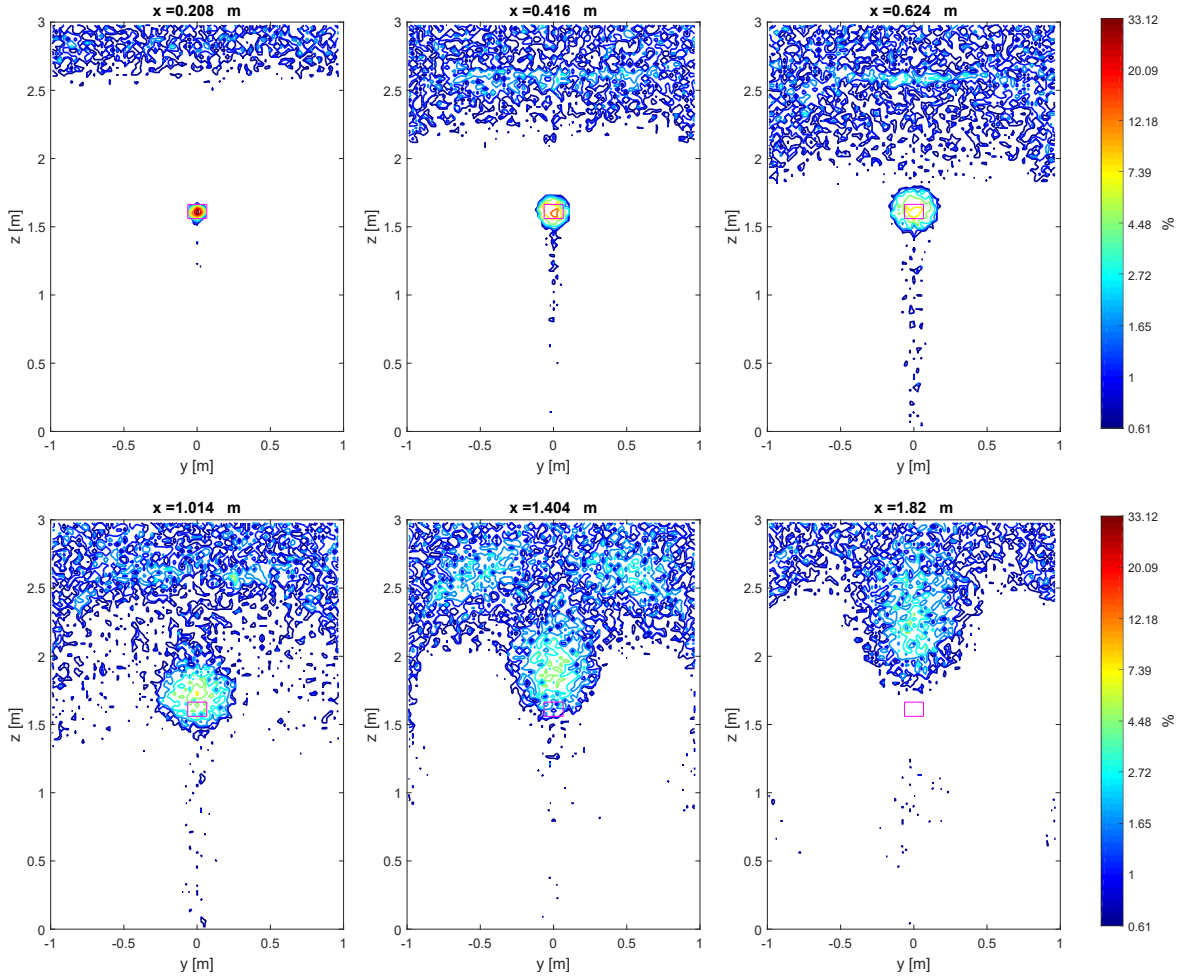

Figure 4.10: Normalized droplet concentration fields within transversal sections at different downstream distances from the mouth obtained for case III; a logarithmic scale is used for colours. The pink square indicates the position of the mouth.

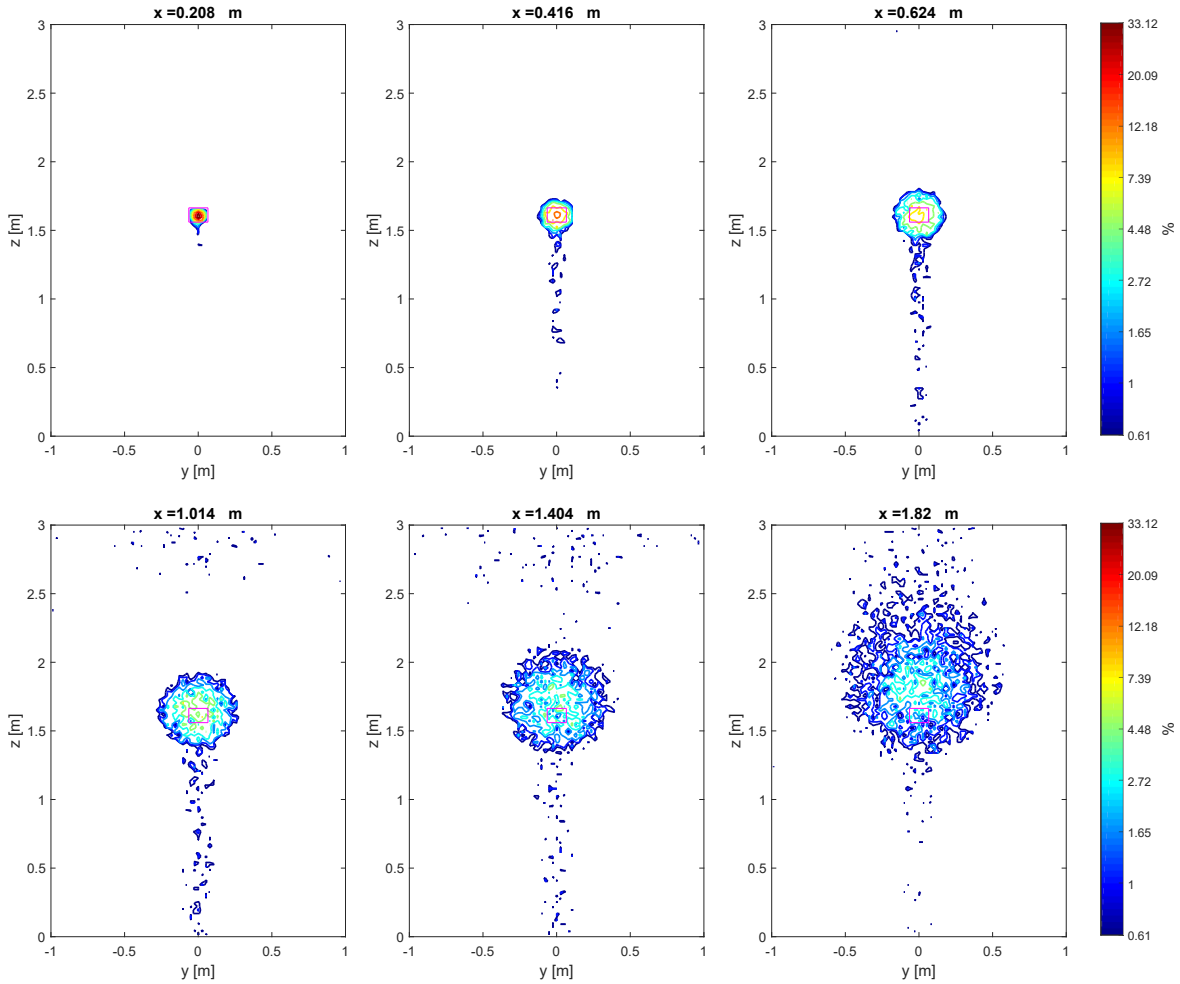

Figure 4.11: Normalized droplet concentration fields within transversal sections at different downstream distances from the mouth obtained for case IV; a logarithmic scale is used for colours. The pink square indicates the position of the mouth.

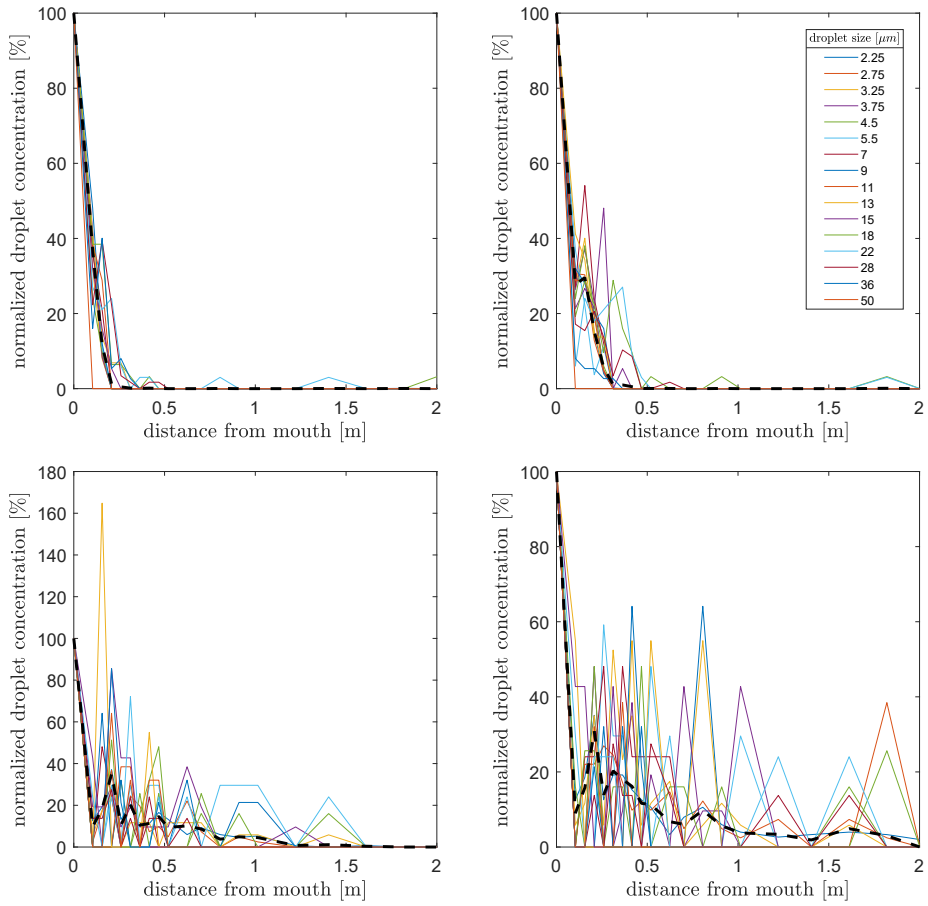

Figure 4.12: Variation of the normalized droplet number concentration at mouth height with distance from mouth; coloured solid lines refer to the different droplet size classes, while the dashed black line to the overall concentration.

equilibrium is very short also for the larger droplets. For example, for a 100 μm droplets with initial velocity far higher than the air – 10 m/s versus 0.5 m/s – the time needed is of about 0.3 s. Consequently, the difference in the traveled distance is very small too, viz., it is less than a millimetre for 1 μm droplets (irrespective of the initial velocity), of the order of millimetres for 10 μm droplets with high initial velocity and of the order of centimetres for 100 μm droplets. Since all the droplets considered here reach the equilibrium with the air before settling, the maximum difference in the traveled distance is reached before settling. For both 1 and 10 μm droplets the time needed to settle, i.e., to travel about 1.6 m along the vertical direction, is long and so the related distance traveled horizontally. Droplets of size 100 μm and zero initial velocity settle in about 3 s, travelling horizontally about 1.6 m from the emission point. The distance traveled by 100 μm droplets with higher initial velocity is not significantly longer – about 16 cm over 1.6 m for droplets with an initial velocity of 10 m/s.

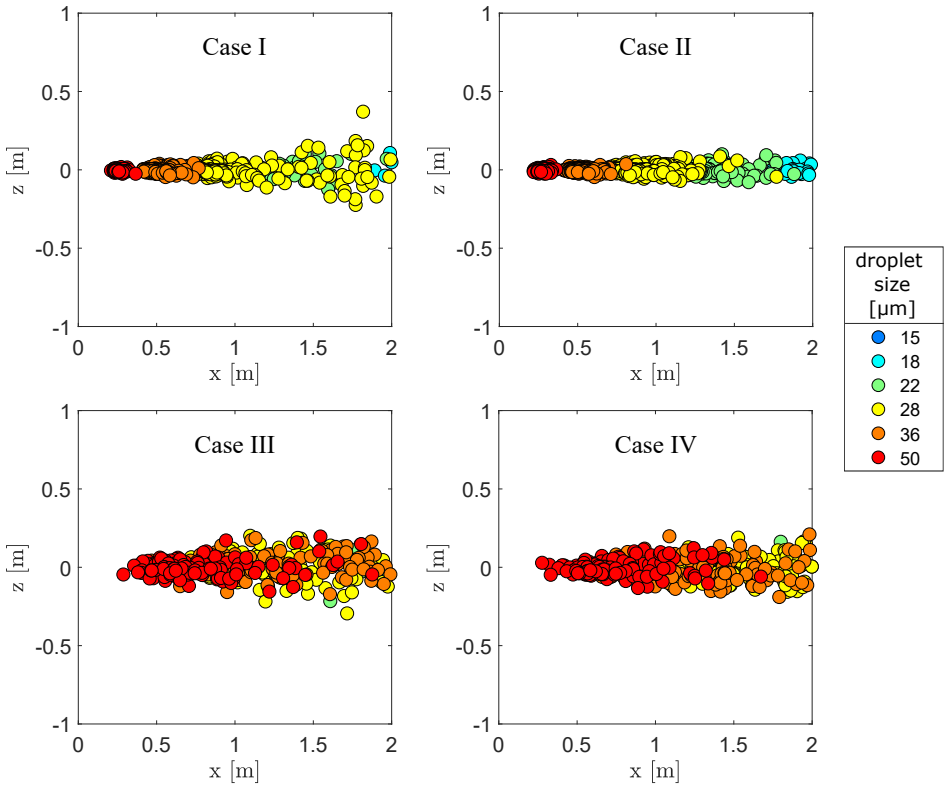

Figure 4.13: Position and size of the droplet settled in the simulations where a zero droplet velocity is set at the mouth; the same 4 airflow cases as in the previous sections are considered.

4.4 Conclusions

In this work, numerical simulations are carried out by means of the software ANSYS Fluent to study the dispersion of droplets ejected by humans while speaking within a semi-closed environment.

Droplet size and velocity distributions obtained experimentally from a laboratory cam-

Table 4.3: Mean and maximum and minimum (in brackets) distances travelled by the settled droplet in the simulations where a zero droplet velocity is set at the mouth.

	Case I	Case II	Case III	Case IV
size μm	x $[m/s]$	x $[m/s]$	x $[m/s]$	x $[m/s]$
18	1.959 (1.999 ÷ 1.891)	1.885 (1.989 ÷ 1.742)		
22	1.414 (1.969 ÷ 1.155)	1.376 (1.881 ÷ 1.146)	1.593 (1.807 ÷ 1.145)	1.726 (1.998 ÷ 1.409)
28	0.992 (1.993 ÷ 0.690)	0.879 (1.769 ÷ 0.676)	1.330 (1.875 ÷ 0.720)	1.455 (1.998 ÷ 0.832)
36	0.510 (0.768 ÷ 0.413)	0.517 (0.809 ÷ 0.413)	1.167 (1.992 ÷ 0.468)	1.192 (1.986 ÷ 0.546)
50	0.262 (0.366 ÷ 0.208)	0.267 (0.363 ÷ 0.219)	0.798 (1.876 ÷ 0.288)	0.773 (1.673 ÷ 0.276)

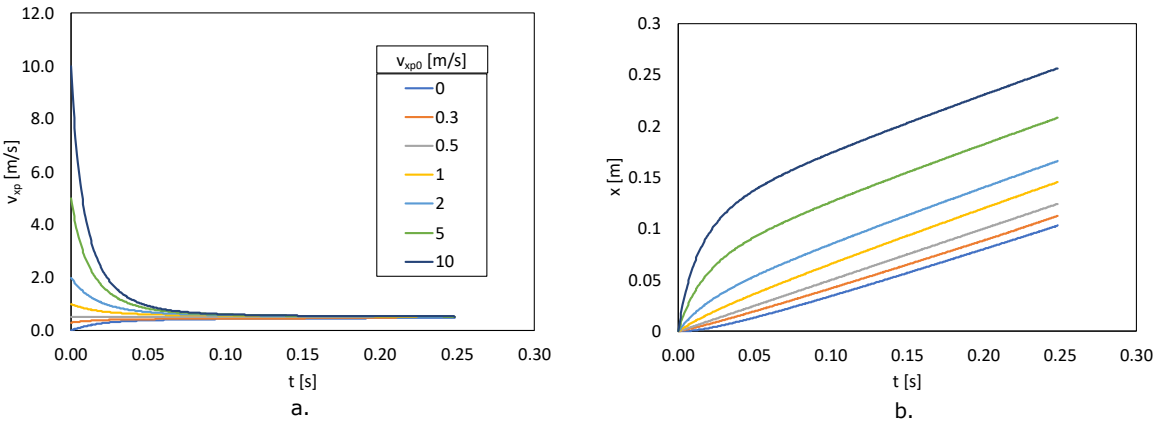

Figure 4.14: Horizontal velocity (a.) and position (b.) variation in time for 100 μm droplets with different initial velocity; the droplets move in a constant horizontal airflow of 0.5 m/s.

Table 4.4: Time taken by droplets of different size and initial velocity to reach the equilibrium with air (t_{EQ}) and difference in the horizontal distance travelled by initially faster droplets and droplets with zero initial velocity, for each droplet size.

	$d = 1\mu m$		$d = 10\mu m$		$d = 100\mu m$	
$v_{x,i}$ $[m/s]$	t_{EQ} $[s]$	$diffmax$ $[m]$	t_{EQ} $[s]$	$diffmax$ $[m]$	t_{EQ} $[s]$	$diffmax$ $[m]$
0	$9.00\ 10^{-6}$	0.00	$9.20\ 10^{-4}$	0.00	$2.51\ 10^{-1}$	0.00
0.3	$7.00\ 10^{-6}$	$7.66\ 10^{-7}$	$6.40\ 10^{-4}$	$9.07\ 10^{-5}$	$2.11\ 10^{-1}$	$9.56\ 10^{-3}$
0.5	0.00	$1.24\ 10^{-6}$	0.00	$1.44\ 10^{-4}$	0.00	$2.13\ 10^{-2}$
1	$9.00\ 10^{-6}$	$2.48\ 10^{-6}$	$9.20\ 10^{-4}$	$2.87\ 10^{-4}$	$2.51\ 10^{-1}$	$4.26\ 10^{-2}$
2	$1.20\ 10^{-5}$	$5.05\ 10^{-6}$	$1.25\ 10^{-3}$	$5.89\ 10^{-4}$	$2.78\ 10^{-1}$	$6.33\ 10^{-2}$
5	$1.50\ 10^{-5}$	$1.28\ 10^{-5}$	$1.52\ 10^{-3}$	$1.32\ 10^{-3}$	$2.95\ 10^{-1}$	$1.06\ 10^{-1}$
10	$1.70\ 10^{-5}$	$2.56\ 10^{-5}$	$1.68\ 10^{-3}$	$2.36\ 10^{-3}$	$3.02\ 10^{-1}$	$1.57\ 10^{-1}$

paign are used as input for the discrete phase. The innovative simultaneous measurement of droplet velocity and size have two advantages. First, it allows us to assign the actual initial droplet velocity instead of a zero velocity or that of the air emitted from the mouth. Secondly, it makes it possible to estimate a realistic droplet emission, expressed as number of droplets ejected per unit time.

Setting for the droplets the actual initial velocity resulted to do not have any significant effect. In fact, distances travelled by settled droplets do not differ between simulations where either a zero droplet initial velocity or the measured droplet velocity distributions are used as input. This result was expected given simple considerations about droplets in a wide range of sizes and velocities settling in a uniform horizontal airflow.

On the other hand, the simultaneous measurement of droplet size and velocity is useful to estimate the droplet emission from experimental data, thanks to which it is possible to infer a realistic droplet concentration within the simulation domain.

Input for the gaseous phase – air velocity and temperature – are taken from the literature. For the air ejection velocity the results in the literature are discordant. Therefore, two extreme cases are considered in the present work, i.e., 0.5 and 4 m/s. Besides, two different ambient temperature are taken into account, 293.15 K and 301.15 K, representing typical winter and summer conditions in indoor environments. The exhaled air temperature is fixed at 306.15 K in both the cases, in agreement with the literature.

The air jet emission velocity is of major importance as it determines how long the droplets remain within the air jet. The higher the initial velocity the longer the distance travelled by the air jet downstream of the mouth. The buoyancy effect – which increases with the temperature difference between ambient and exhaled air and decreases as the air jet emission velocity grows – plays also a key role. For the so-called direct (or short-range) airborne transmission, a greater buoyancy has a positive effect, as the buoyant air jet removes the droplets from the breathing zone, transporting them towards the ceiling. The effect of buoyancy on indirect (or long-range) airborne disease transmission depends on the geometrical configuration and ventilation condition considered, in particular, on the interaction between them and the jet. In the present simulations, less droplets accumulate into the domain in the two cases with weaker buoyancy effect, as the droplet-laden air jet is allowed to exit from the front face.

Considering a more realistic representation of an indoor environment with different kind of ventilation, such as mixing, downward and upward ventilation, can be a future development of the present work.

Another improvement of the work could be the assessment of the time variation of droplet dispersion within the domain. The steady simulations carried out in the present work are representative, indeed, of a long continuous speech occurring in a not-varying ventilation condition.

Furthermore, other respiratory activities could be assessed along with the evaporation effect in order to improve the results.

Chapter 5

Conclusions

The present thesis aimed to improve the knowledge of the emission of droplet-laden air clouds exhaled by humans during different respiratory activities. Although several simplified analytical models and Computational Fluid Dynamics simulations have been used in recent years to assess cloud dispersion and related infectious disease transmission risks, experimental data to be provided as input are still lacking or ambiguous.

The Interferometric Laser Imaging for Droplet Sizing (ILIDS) technique has been chosen as measurement technique since it makes it possible to detect simultaneously droplet size and velocity. Also, ILIDS overcomes some of the problems encountered in the literature. Notably, it allows data collection close to the mouth reducing the importance of evaporation and dilution processes, which could affect droplet size and number measurements. Besides, with ILIDS dusts naturally present in the air can be identified and excluded, making unnecessary the use of air filters. Lastly, ILIDS setup is rather simple and adaptable to an unconventional testing environment such as the one used here involving human beings. ILIDS setup consists of a laser sheet illuminating the exhaled droplets, an optical system and a camera for image recording. However, improvements of the standard ILIDS setup (and of the related image processing) were necessary to detect droplets down to 2 μm and to measure their all three velocity components. These improvements constitute the main results of Chapter 2, which are summarized below:

1. An optical system constituted by two aspherical lenses and a diaphragm to adjust the lens aperture made it possible to obtain a collection angle (angle formed by the effective lens aperture and the observed droplet) sufficiently wide to measure droplets down to 2 μm. Note that this is the lowest absolute limit for ILIDS technique. The measurement would not be possible by using common optical systems (such as commercial lens assembly and spherical lenses) due to spherical aberrations.

2. Ad-hoc image processing able to treat the other geometrical aberrations proper of aspherical lenses was developed. These deformations do not prevent the measurement but need to be considered. Namely, a deformation was applied to the images, which required a proper calibration.

3. Automatic selection criteria to distinguish between exhaled droplets and dusts were also set. However, this point requires further insights.

4. The relations allowing for droplet velocity measurement with the setup used were found. Particularly, the third velocity component perpendicular to the image plane was obtained, in addition to the two velocity components laying on the vertical plane corresponding with the laser sheet. This is a strong point of the work in that only two components are usually detected in techniques that employ a laser light sheet. The calibrations needed for velocity measurements were also performed.

5. The measurement volume was carefully quantified. Although it is needed to compare the quantity of droplets of different sizes, this kind of measurement is rarely carried out.

In Chapter 3 the two measurements campaigns carried out at the Laboratoire de Mécanique des Fluides et Acoustique of the École Centrale de Lyon in May 2021 and November-December 2021 are presented. The campaigns involved twenty-three volunteers. Precise protocols were defined to reproduce the respiratory activities of speaking, coughing and breathing. Besides, the effects of protection tissue and surgical masks were analyzed. Lastly, the variability among different tests of the same volunteer (intra-volunteer variability) is assessed.

The main results can be summarized as follows:

1. Droplets in the range 2-60 μm were detected for speaking and coughing activities, while the largest droplets in case of breathing were $\sim$ 8 μm. In all the respiratory activities the highest droplet concentrations belonged to the range $2 - 2.5$ μm. For the speaking activity the concentration decreases rapidly until a relative maximum is observed between $20 - 30$ μm. Droplet size distribution for coughing activity is more scattered than for speaking in the range $2 - 10$ μm. The absence of droplets larger than 60 μm needs to be further analysed as it could be due to solid inclusions in the larger droplets. Coughing data also require further inspection. Few images with very high droplet concentrations were observed in coughing. These images cannot be treated with the current image processing, so that further improvements must be tested.

2. The comparison of our results with those found in the literature is reasonably good for speaking and coughing activities in the range $2 - 10$ μm. For the other size-range it is hard to draw conclusions due to the large inconsistency of results found in the literature.

3. For the breathing our results differ from previous works. The difference is probably ascribable to the fact that the latter do not take into account evaporation and dilution effects.

4. By comparing the overall droplet concentration for the three respiratory activities, the highest value occurs for coughing, followed by speaking and breathing.

5. The coughing activity shows the highest stream-wise droplet velocity. Mean stream-wise droplet velocity were $\sim$ 2.5 m/s for coughing, against $\sim$ 0.3 m/s for speaking and

breathing. Maximum stream-wise velocities were $\sim$ 1.81, 10.5 and 0.4 m/s on average among the volunteers for speaking, coughing and breathing, respectively. The absolute maximum stream-wise velocities were 3.68, 28.1 and 0.7 m/s for the three activities. These values are in agreement with the literature, even though the latter are generally referred to air velocity rather than to droplet velocity.

6. The span-wise and vertical velocity components range between negative and positive values ($\sim$ 0 m/s on average).

7. Both for speaking and coughing droplet velocity increases with its size.

8. Droplet ejection is far from being unidirectional, in agreement with previous works.

9. A great variability among the volunteers is observed both for droplet velocity and size. The intra-variability is only slightly attenuated.

10. Protection masks are effective in reducing droplet velocity, in addition to the number of exhaled droplets.

In Chapter 4 the experimental data concerning droplet velocity and size were used as input in numerical simulations carried out by means of the software ANSYS FLUENT to study droplet dispersion within a semi-closed environment. A steady ejection of droplet and air from the mouth is considered, representing a person speaking for a sufficiently long time. Two extreme air ejection velocities (0.5 and 4 m/s) were considered, along with two ambient temperatures typical of summer and winter indoor temperatures (301.15 K and 293.15 K). Air is ejected from the mouth at 306.15 K, according to the literature. Analogous simulations were performed setting to zero the droplet velocity at the mouth. The latter are compared with the previous cases to evaluate the effect of the initial droplet velocity.

The main results are:

1. A stationary air jet forms downstream the mouth. The jet decelerates while moving forwards due to entrainment of ambient air. The air jet moves horizontally only for a short distance when buoyancy effects are higher (higher temperature difference between exhaled and ambient air and lower air ejection velocity).

2. The smallest droplets follow the airflow, reaching the ceiling in cases where strong buoyancy effects occur. Larger droplets fallout from the air jet and settle. The larger the droplet the shorter the distance before falling out the air jet.

3. The distances traveled by the droplets that settle within the simulation domain were quantified. Only droplets larger than $\sim$ 18 μm (at least a portion of them) settle within the domain, the others are still suspended in the air at 2 m from the emission. The mean traveled distance ranges between 0.25 and 1.9 m for droplets of size $\sim$ 50 and $\sim$ 18 μm, respectively, when an air ejection velocity of 0.5 m/s is set at the mouth. Differently, when air was exhaled at 4 m/s droplets of all sizes were transported further.

Notably, between 0.7 and 1.7 m for droplets of size $\sim$ 50 and $\sim$ 22 μm. $\sim$ 18 μm droplets did not settle at all within 2 m from the mouth in this case.

4. The reach probability of droplet of different sizes was calculated, which provides an idea of the number of droplets that are suspended in the air at a given distance from the mouth. Only droplets in the range $\sim 28 - 50$ μm were completely (or almost) removed from the air by settling when the air ejection velocity from the mouth was lower. On the contrary, when the air was ejected from the mouth at the higher speed, only the largest droplets settled completely within the domain.

5. The major role played by the air ejection velocity set at the mouth was clearly shown. On the other hand, the buoyancy effect is weaker in terms of distances traveled by the droplets before settling.

6. Droplet concentration fields within the domain at different streamwise distance from the mouth were calculated. In this case no distinction among droplet size was considered, even if differences in concentrations of droplet of different size were expected based on previous results. High droplet concentration zone close to the emission is observed (the closer the emission the higher the concentration). This zone is expected to be responsible for short-range airborne disease transmission.

7. A positive effect of buoyancy was highlighted analysing droplet concentration fields. Notably, the droplets are removed from the mouth height, where they can be inhaled by a susceptible individual, thanks to the effect of buoyancy which makes the smaller droplets move upwards with the air, while the larger droplets settle.

8. The interaction between the droplet-laden air jet and the walls of the semi-closed domain causes the accumulation of the droplets within the domain, especially close to the ceiling. Accumulation phenomena are less evident in cases with lower buoyancy as the jet is allowed to exit the domain almost undisturbed.

9. Comparing the simulations where droplets have zero initial velocity and the ones where the experimental velocity distribution is considered, no significant differences were noticed.

Possible developments of the work presented in Chapter 4 consist in considering more realistic indoor setting and droplet evaporation.

Appendix A

Metrology-calibrations

A.1 Calibration of image deformation

As mentioned in Chapter 2, two aspherical lenses in series are used in this work in order to obtain a sufficiently wide collection angle allowing us to detect droplets down to 2 µm. Aspherical lenses are designed so that spherical aberrations are minimized. However, this kind of lenses are affected by other kinds of aberrations, namely, coma aberrations. Coma aberrations causes the distortion of the shapes in the image and this distortion depends on the distance of the object from the optical axis. In our case, coma aberrations make the circular form, expected in correspondence of a particle, similar to an ellipse, increasingly eccentric as its distance from the optical axis increases (Figure 2.7a in Chapter 2).

The information that has to be drawn from these distorted images is position and dimension of the ellipse corresponding to a particle and the frequency of the fringes within the ellipse, which is related to the droplet size. Two possible ways have been considered to treat these images affected by coma aberrations, i.e., (i) to detect directly the position and dimension of the ellipses and (ii) to distort the images such that a circular form is obtained and then to detect position and dimension of the obtained circles. The first option has been discarded due to the difficulty in detecting ellipses of varying position, rotation, dimension and eccentricity. Thus, the second option has been adopted, which is easier as only two parameters must be determined in case of a circle, i.e., its position and radius.

The second option requires to define the deformation to be applied to the images. To do this, calibration images have been taken by using a 10 μm hole and displacing it within the laser light sheet at different distances from the optical axis. The little hole works as a point light source, giving an image similar to a particle (but without interference fringes). Calibration images used in the first measurement campaign are superposed and shown in Figure 2.7a in Chapter 2.

Different types of deformations have been applied to the calibration images until a satisfying result has been obtained. In general, given the features of coma aberrations, a deformation dependent on the distance from the optical centre is used (Equation A.1):

$$S = f(s) \tag{A.1}$$

where s and S are the distances of a point P from the optical centre in the original and deformed image, respectively, while f is the function describing the applied deformation. Therefore, the coordinates of a point P in the new reference system of the deformed image (Y,Z) are (Equations A.2 and A.3):

$$Y = \frac{f(s)}{s}\ (y - y_o)\ + y_o \tag{A.2}$$

$$Z = \frac{f(s)}{s}\ (z - z_o)\ + z_o \tag{A.3}$$

where y and z are the span-wise and vertical coordinates of P in the original image and y_o, z_o are the coordinates of the optical centre (unchanged between original and deformed images). Equations A.2 and A.3 are obtained by considering that:

$$(y - y_o) = s\ cos(\phi) \tag{A.4}$$

$$(z - z_o) = s\ sen(\phi) \tag{A.5}$$

and analogously:

$$(Y - y_o) = S\ cos(\phi) \tag{A.6}$$

$$(Z - z_o) = S\ sen(\phi) \tag{A.7}$$

where ϕ is the angle between the two position vectors s and S and the horizontal direction. Note that ϕ is unchanged between the original and deformed images. Then, from the previous equations A.4–A.7 the following relations are derived:

$$(Y - y_o) = S\ \frac{(y - y_o)}{s} = \frac{f(s)}{s}\ (y - y_o) \tag{A.8}$$

$$(Z - z_o) = S\ \frac{(z - z_o)}{s} = \frac{f(s)}{s}\ (z - z_o) \tag{A.9}$$

A representation of this kind of deformation is shown in Figure A.1.

Several forms of the function $f(s)$ have been tested and a 5^{th}-order polynomial has been chosen, as it provided satisfying results (Eq. A.10):

$$f(s) = s + c_2\ s^2 + c_3\ s^3 + c_4\ s^4 + c_5\ s^5 \tag{A.10}$$

Note that the coefficient of the zero-exponent term, c_0, is 0 as the coordinates of the

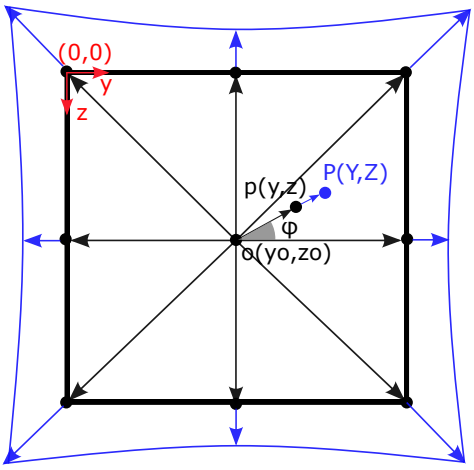

Figure A.1: Sketch of image deformation; the original image is in black, while the deformed image is in blue. The arrows are the distances of the point of interest (edge of the image and point P) from the optical centre.

optical centre (y_o, z_o) remain unchanged after the deformation. Besides, the first-exponent term coefficient c_1 is 1, as $S \to s$ if $s \to 0$.

The four coefficients c_2, c_3, c_4, c_5 have to be calibrated in order to obtain a deformed image where a circular form is observed in correspondence of a particle located wherever within the field of view. The optical centre coordinates need to be inferred by calibration too; the camera and the optical system have been aligned so that the optical centre almost coincides with the image centre, but the coordinates must be found with greater accuracy.

The calibration procedure is described briefly in what follows. First approximation values for c_2, c_3, c_4, c_5, y_o and z_o are fixed. The coordinates of the 4 points (p1(y_1,z_1), p2(y_2,z_2), p3(y_3,z_3), p4(y_4,z_4)) defining the two axes of the ellipse observable in each calibration image are taken and the related distances from the optical centre are calculated (s1, s2, s3, s4). Refer to Figure A.2 for a graphical explanation of the points and the related distances. Then, the deformed coordinated of the 4 points (P1(Y_1,Z_1), P2(Y_2,Z_2), P3(Y_3,Z_3), P4(Y_4,Z_4)) are obtained by applying Equations A.8 and A.9. With these coordinates the lengths of the two axis of the ellipse in the deformed image are calculated. Finally, the values of c_2, c_3, c_4, c_5, y_o and z_o giving the minimum square difference among all the axes in all the calibration images and their mean value (least squares procedure):

$$Min[\sum_i (a_i \ \frac{1}{2 \ N_{immcal}} \ \sum_i a_i)^2] \tag{A.11}$$

where i=1,. . . , 2 N_{immcal}, N_{immcal} is the number of calibration images (there are two axes for each image) and a_i is the i^{th} axis, which depends on c_2, c_3, c_4, c_5, y_o and z_o as follows:

$$a_i = \sqrt{\left\{[\frac{f(s2)}{s2}\ (y_2 - y_o) + y_o] - [\frac{f(s1)}{s1}\ (y_1 - y_o) + y_o]\right\}^2 + \left\{[\frac{f(s2)}{s2}\ (z_2 - z_o) + z_o] - [\frac{f(s1)}{s1}\ (z_1 - x_o) + z_o]\right\}^2} \tag{A.12}$$

The relation for the second axis is analogous, but p3(y_3,z_3) and p4(y_4,z_4) are used.

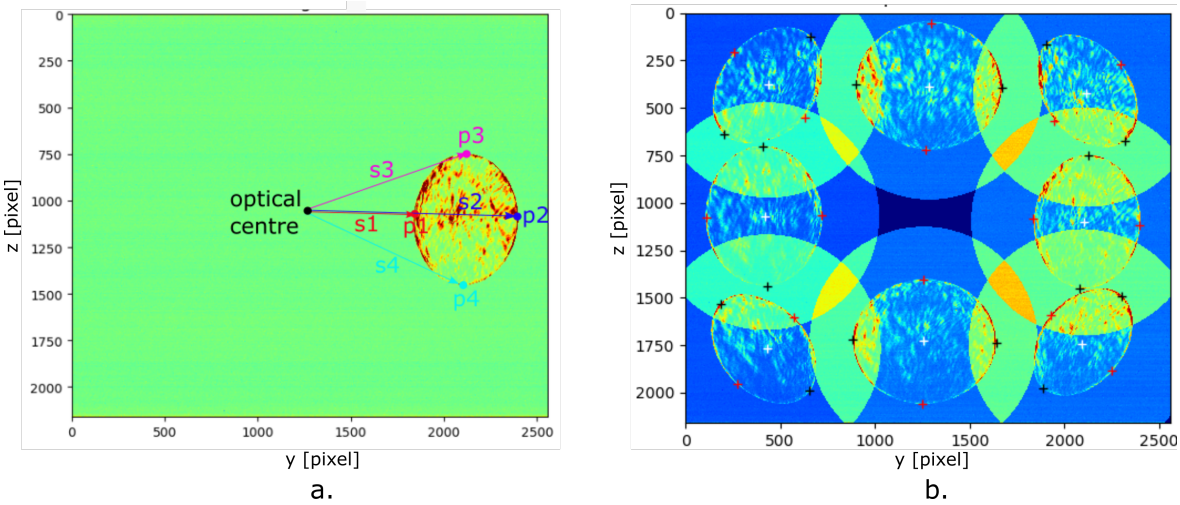

Figure A.2: a. Exemplification of points used for image deformation calibrations and b. superposition of the 8 deformation calibration images for the first measuring campaign. The points identifying the ellipse axes are in red and black.

The coefficients $c_2 \div c_5$ and the optical centre coordinates obtained for the two measurement campaigns are listed in Table A.1. Note that in the second campaign the camera has been rotated so that the y and z size of the image is reversed from to the first measurement campaign.

Table A.1: Deformation calibration coefficients obtained for the two measurement campaigns.

	Campaign 1	Campaign 2
c_2	9.4310^{-6}	1.1810^{-5}
c_3	1.9510^{-8}	1.2810^{-8}
c_4	7.6710^{-14}	5.9310^{-14}
c_5	7.4510^{-14}	5.7510^{-14}
yo	1218	1072
zo	1030	1305

A.2 Span-wise and vertical displacement calibration

As mentioned in in Chapter 2, the two parameters, γ_1 and γ_2, have to be calibrated with experimental data in order to account for the real characteristics of the optical system and

possible default of optical adjustment. This section describes in detail the calibration of γ_1, which linearly relates the displacements of the circles in the image plane and the real displacement of the droplets in the laser sheet.

A 10 μm hole located within the laser light thickness is used as a point light source, forming on the image elliptical shapes, like the ones that is produced by small particles. Images of the point light source are taken at different positions within the laser light sheet and are used for the calibration of span-wise and vertical displacements. Two calibrations have been carried out on 5th May 2021 and 4th November 2021 for the first and the second measurement campaign, respectively. Examples of calibration images are shown in Figure 2.7a in Chapter 2 for the first measurement campaign.

The position of the ellipse located at the centre of the image is taken as a reference and the distances of the other ellipses from the reference one is calculated (Δz_{out}). Analogously, the distance between the different positions of the point light source and its central position is calculated (Δz). Finally, the ratio between Δz_{out} and Δz - i.e. γ_1 - is obtained. In order to obtain the position of ellipse centres the deformation (previously calibrated) is applied to the calibration images in order to correct coma aberrations and obtain a circular form irrespective on the distance of the little hole from the optical axis. Then, the position of the circles (circle centres) corresponding to different positions of the point light source is measured on the images. Subsequently, the coordinates are anti-deformed and reported again in the original image coordinate system. This is necessary because the applied deformation is not physical, but it has just the goal of making possible the detection of the circles, as already discussed in the main text.

The values obtained for the ratio between Δz_{out} and Δz for the two measurement campaigns are shown in Figures A.3.

In both the cases the value of the ratio is 0.9 on average, which agrees with the value theoretically calculated by means of Equation 2.3 of Chapter 2 and considering and idealized optical system. Since this ratio slightly varies within the image, the value proper of a given position within the image is considered when the droplet displacement is measured.

A.3 Stream-wise displacement calibration

The size of the circle corresponding to a particle in the image (after deformation) depends only on the stream-wise (x) position of the particle within the thickness of the laser sheet (Equation 2.5 in Chapter 2). The coefficient γ_2 in the latter equation is calibrated by measuring the radius of circles produced on calibration images by a point light source at different position within the thickness of the laser sheet. The y-z position of the point light source does not change among the calibration images. As a point light source the same 10 μm hole used for the calibrations described above is used. Examples of calibration images are shown in Figures A.4 and A.5 for the first and the second measurement campaign. Note that the calibration images are deformed before measuring the circle radius. The measured circle radius is plotted

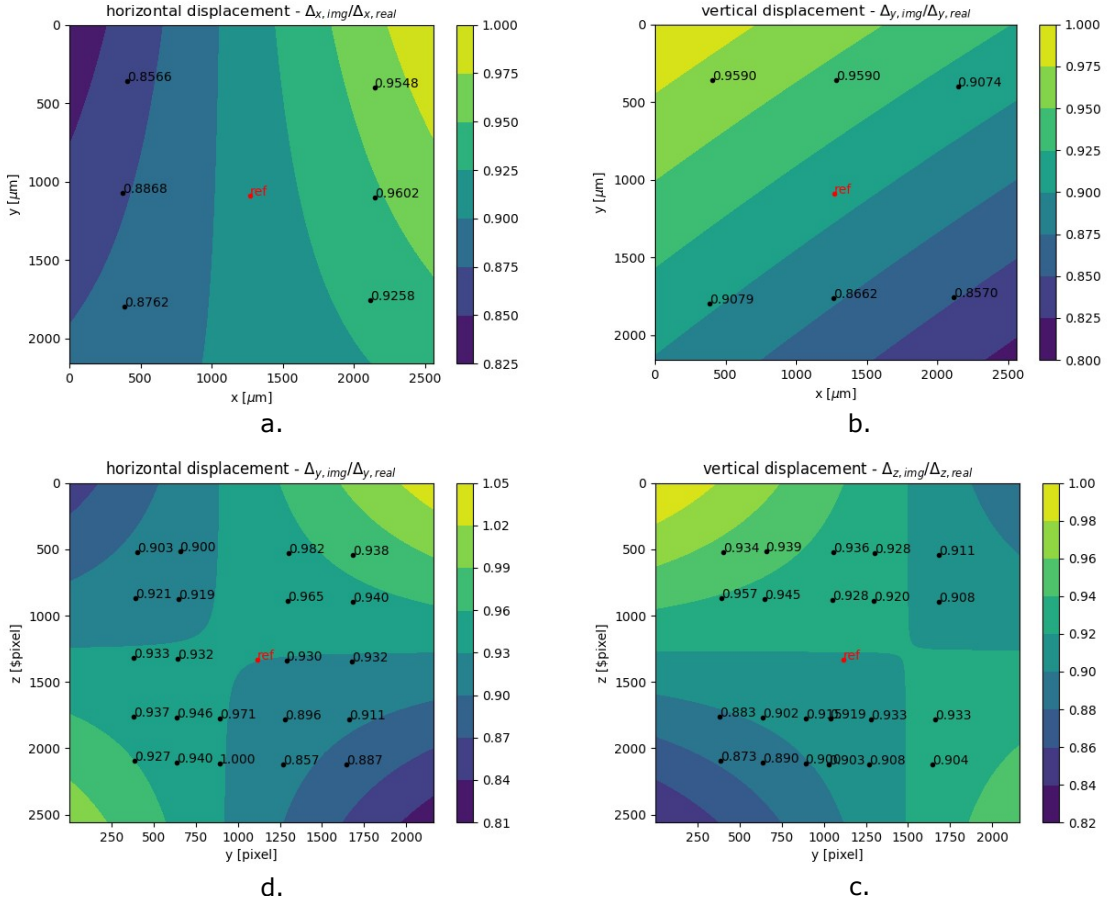

Figure A.3: Values of the ratio between displacement on the image and real scale displacement for the first campaign (a.horizontal and b. vertical) and second campaign (d. horizontal and b. vertical)

as a function of the measured stream-wise position in Figures A.4 and A.5. As expected, the two quantities are linearly proportional. The slope gives the value of γ_2, while the intercept corresponds to the radius at the maximum laser light intensity (at x=0mm). If x is converted in pixel – the size of the pixel is 6.5 10^{-3} mm/pixel –, for the first measurement campaign the value of 0.38 for γ_2 as reported in Chapter 2 is found.

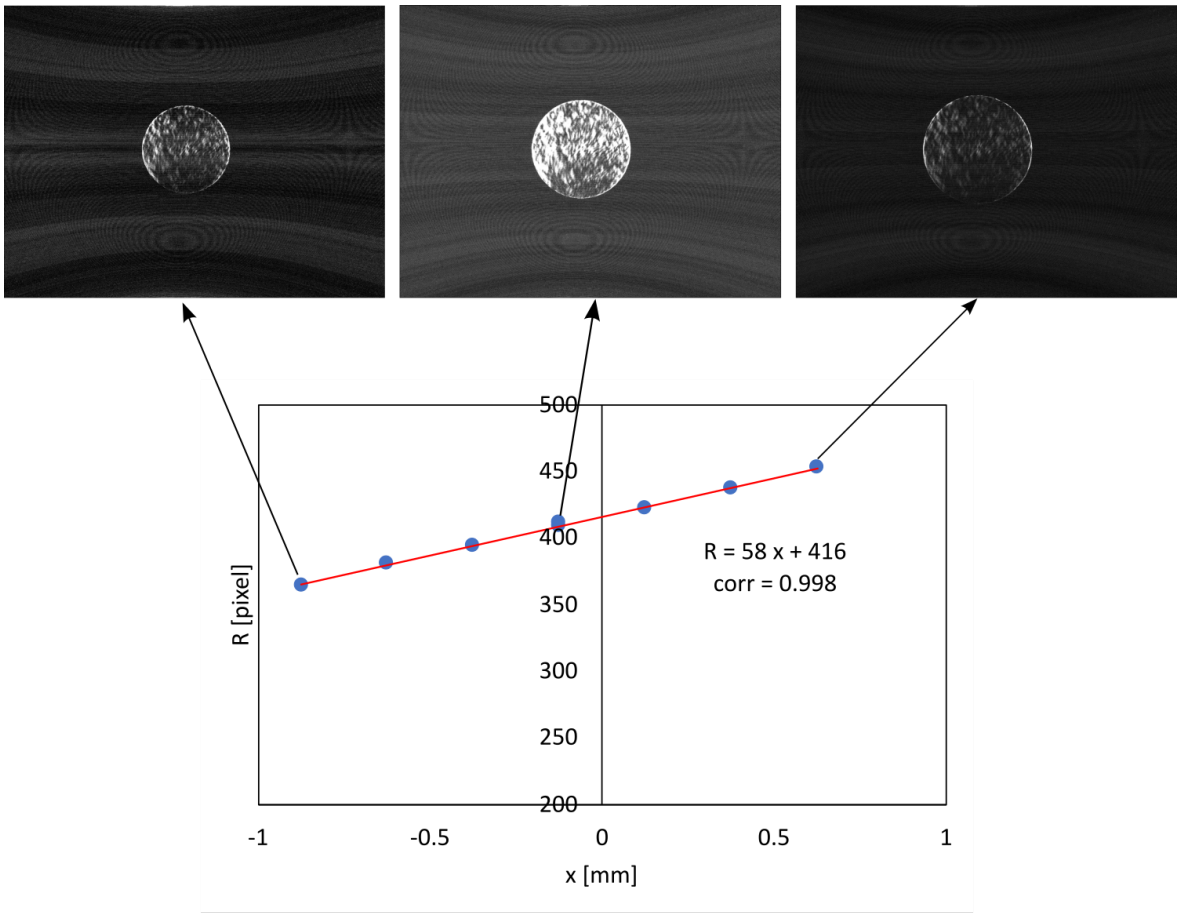

Figure A.4: Radius of the circles corresponding to a point light source at different stream-wise (x) positions within the thickness of the laser light sheet; three examples of images of the point light source are shown above the plot. These data refer to the first measurement campaign

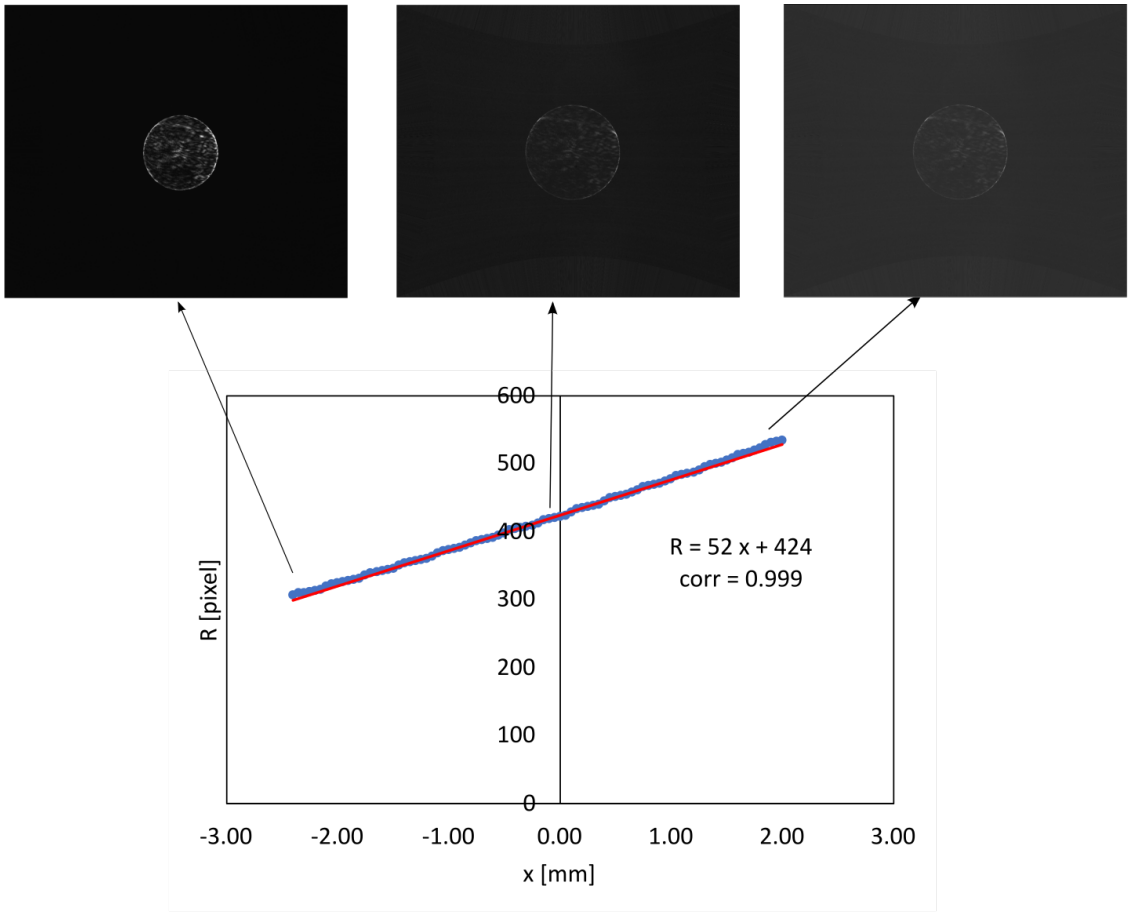

Figure A.5: As for Figure A.4, but for the second measurement campaign.

Appendix B

Metrology-image processing for droplet detection and sizing

As mentioned in Chapter 2, both liquid and solid particles present in the images are identified. Namely, the position and radius of the circles corresponding to the particles are detected (particle detection phase). Then, the frequency analysis of the image of each detected particle is carried out. In this phase, solid particles are recognized and discarded, while only the size of the liquid particles (droplets) is retained. The algorithm used in the scripts is shown in the following as a flowchart, where each loop is characterized by a color (black, blue and green). Red boxes indicate output data.

The run is launched for each test performed by each volunteer. The images belonging to the test are grouped and each group is assigned to a core for the analysis. One image at time is opened and processed by each core (black loop in Figures B.1 and B.2).

One deformed and cut image is opened (Figure B.3) and extended (Figure B.4), so that even circles that are included only partially within the image can be detected. Then a synthetic image of a ring of radius $rcirc$=350 pixel and thickness dr=10 pixel is built (Figure B.5). $rcirc$ is about the radius observed in the images on average, while dr is set so that a good correlation can be found between the synthetic ring and the circle edge even if the circle radius of the two is slightly different.

Then, the particle detection loop begins (in blue in Figure B.1). A maximum number of particles max_part = 5 and 30 is set for the speaking and the coughing tests, respectively. A Gaussian filter is applied to the image in order to smooth any fringes within the circles corresponding to the particles. The parameter of the Gaussian filter must be set so that the fringes in all the range of frequency are smoothed. Then, the gradient of the smoothed image is calculated (Figure B.6). In this latter image only the pixels corresponding to the edge of the circles should be different from zero. The convolution between the gradient image and the synthetic ring image (Figure B.5) is, then, calculated. A maximum of correlation should be observed in correspondence of first detected circle position. This provides, hence, a first estimation of the circle position (z0, y0) (Figure B.7). To speed up the procedure, the gradient

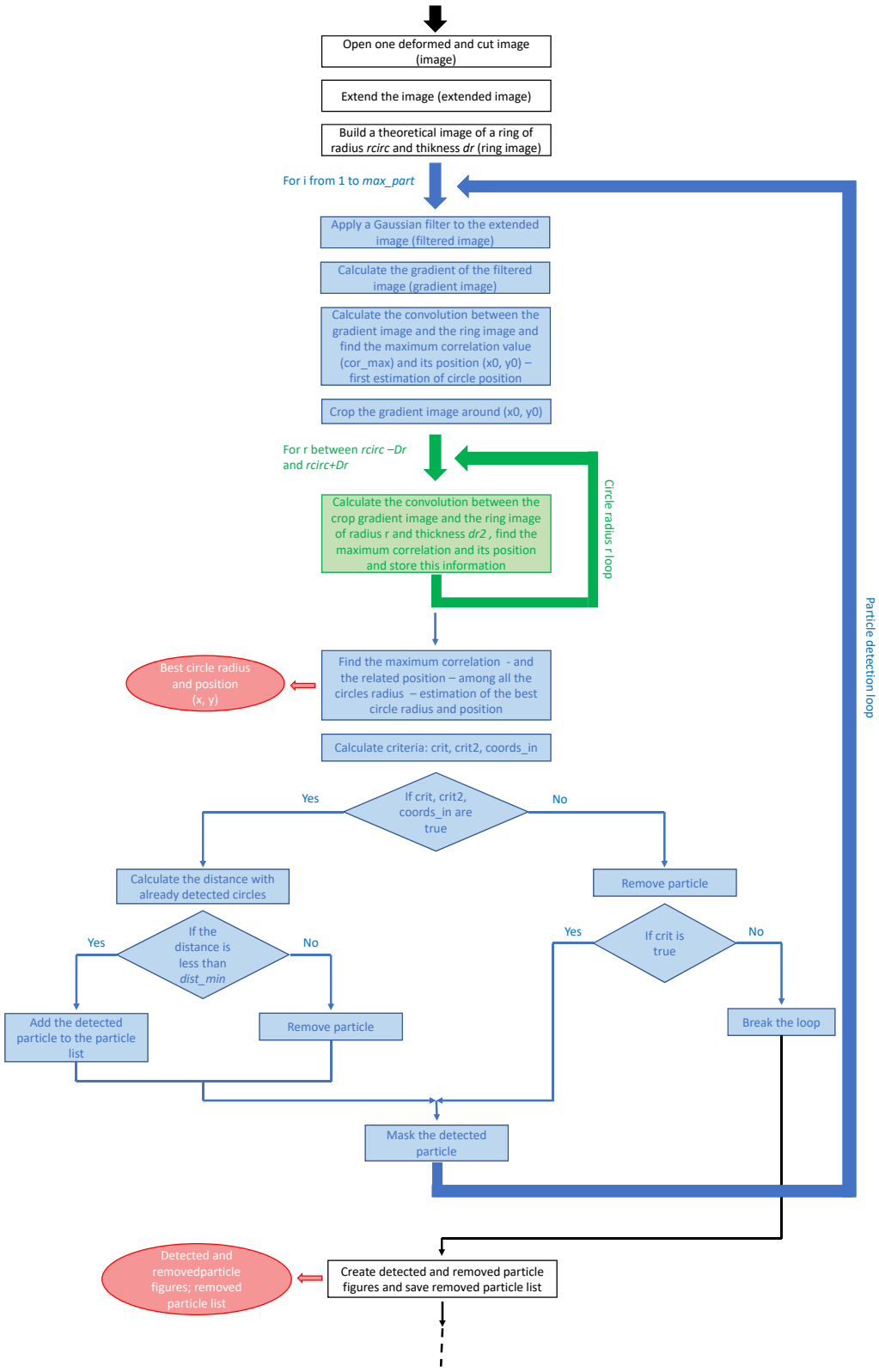

Figure B.1: Flowchart of particle detection loop.

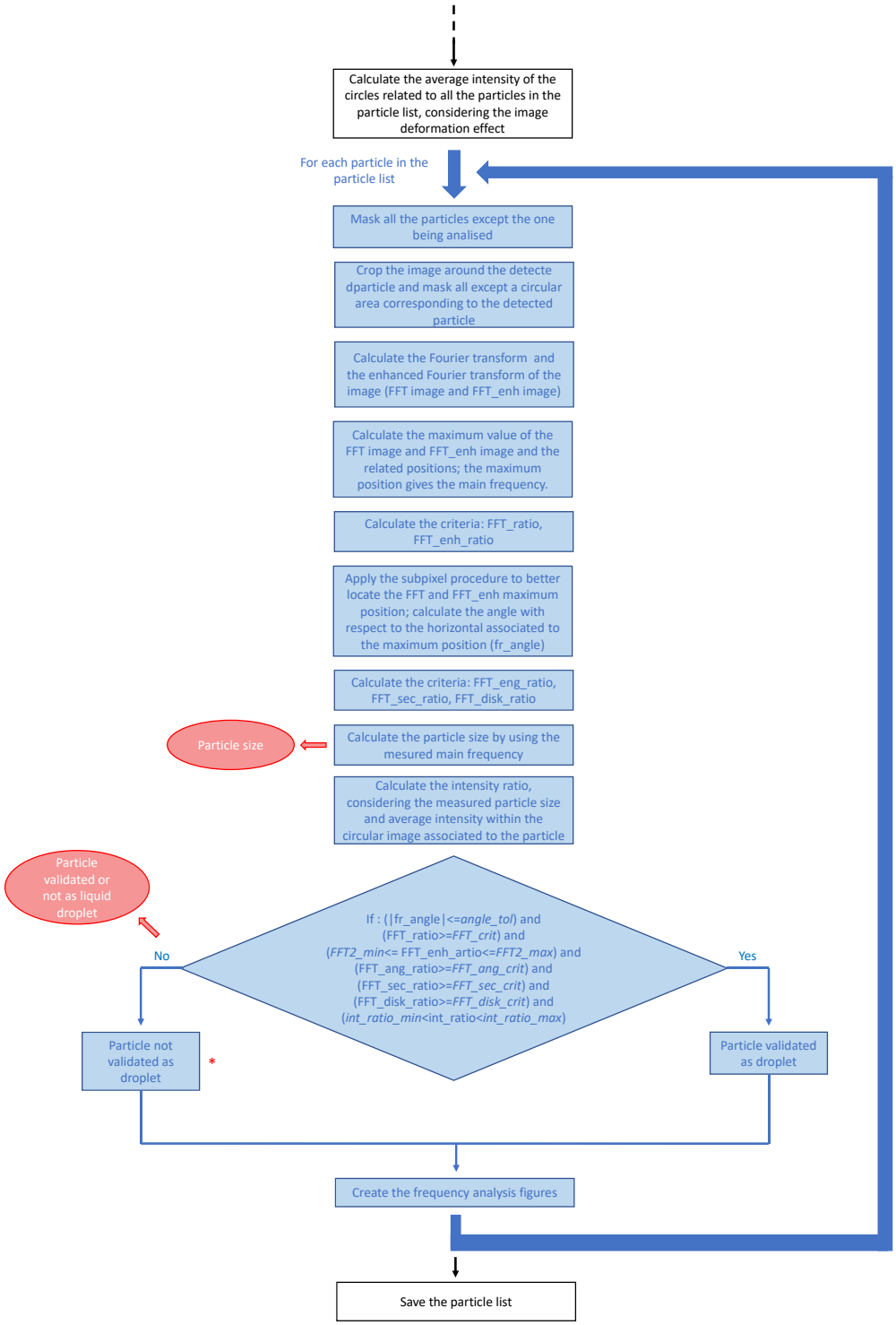

Figure B.2: Flowchart of frequency analysis loop.

image is cropped around (z0, y0), so that the refinement of circle position and the research of the best circle radius is carried out only on a portion of the image.

A cropped ring image is also built. The radius of the ring varies between ($rcirc + Dr$) and ($rcirc - Dr$), where Dr=200 pixel, with a step of 1 pixel. For each radius the convolution between the crop gradient image and the crop synthetic ring image is calculated and the position and value of maximum correlation is stored. It is worth noting that in this phase the thickness of the synthetic ring is $dr2$=4 pixel, which is smaller than the previously used dr in order to refine the circle radius detection. Once all the radii have been tested, the maximum of correlation among them is taken, providing the best circle radius and position (Figure B.8).

Since the algorithm would always find a maximum correlation, even without a real circle appearing in the image, the setup of some selection criteria is needed. The first criteria, $crit$, evaluates whether the maximum of correlation is significant or not. It is calculated by multiplying the maximum of correlation (max_corr) and the ratio between the perimeter of a circle of a given radius R and the perimeter of the circle section actually falling into the image (Eq. B.1):

$$crit = max\_corr \frac{per(R)}{partial\_per(R)} \tag{B.1}$$

The ratio is needed for particles whose circle does not fall completely into the image. In this case the correlation value is lower because it is calculated only on the portion of the circle falling into the image rather than on the complete circle. A limit of 2 is imposed for the ratio, as only circle at least halfway falling into the image are considered.

The second criteria is $crit2$, defined as the ratio between the standard deviation and the average of pixel values (i.e. intensity value) on the edge of the detected circle (Eq. B.2):

$$crit2 = \frac{std(circle\_edge)}{avg(circle\_edge)} \tag{B.2}$$

This criterion is useful to exclude cases where high correlations are found because of high light intensity points rather than circles (Figure B.10). The edge of a circle corresponding to a particle is quite uniform, giving low values of $crit2$. In contrast, when the high correlation is due to high intensity points, the value of $crit2$ is quite high.

The third criterion consists in taking into account only circles whose centre fall into the image ($coords\_in$) since the circle centre corresponds to the particle position. Taking circles whose centre is outside the image would mean considering particles outside the field of view.

Once the three criteria are calculated for the detected particle, a check on them is done. Thus, $crit$ must be greater than a limit value $crit\_lim$, $crit2$ must be less than a limit value $crit2\_lim$ and the circle centre coordinates must fall into the image.

If all the three criteria are respected another check is done. Namely, the distance between the particle and the other previously detected particles must be greater than a limit value $dist\_min$. This check is needed to avoid that multiple particles are detected at the same place (Figure B.11). Indeed, the already detected particles are covered by a mask, which could give

high correlation with the synthetic ring image. If this last check is verified, the detected particle is validated and it is added to the particle list. If this last check is not satisfied, the particle is discarded and the detection particle loop goes on.

If one of the first three criteria is not respected, the particle is discarded. If the unsatisfied criterion is *crit*, i.e. if the maximum of correlation is lower than a critical value *crit_lim*, the particle detection loop is broken (before reaching *max_part*). Otherwise, the loop goes on. In fact, when the maximum correlation value is too low, the droplet is not bright enough to be detected, i.e. either it is very small or it is very big but it is not located into the laser light sheet and it is illuminated only indirectly. As shown above, another reason to have a low maximum correlation value is that the droplet is outside the field of view.

When either *max_part* is reached or the loop is broken due to the criterion *crit*, all the possible particles in the image have been detected and the frequency analysis can be performed for each of them.

Before starting the frequency analysis, the discarded particles are saved in an output file, so that a check is possible a posteriori. Also, the average intensity (pixel value) of each circle corresponding to a particle in the particle list (taken particles) is calculated. In the calculation the effect of the previous image deformation is considered. Namely, a mask is applied to the deformed image before calculating the average intensity, so that the total intensity within a circle (sum of pixel values) is equal to the total intensity within the elliptical shape corresponding to the droplet before deformation.

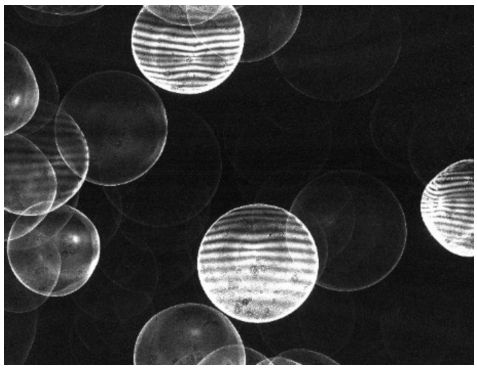

Figure B.3: Example of deformed and cut image.

Then, the frequency analysis loop starts (Figure B.2)and the images in the particle list (taken particles) are analysed one by one, considering the original deformed and cut images. All the other particles, except the one that is analysed are masked. In this way if the circles corresponding to the particles are partially superposed, only the non-superposed part of the circle – and, hence, of the scattering pattern – is analysed, avoiding mistakes due to frequency superposition.

Then, the image is cropped around the particle being analysed. Only the circular area corresponding to the particle is analysed, while the rest of the cropped image is masked. A value equal to the average within the circle is assigned to the masked part of the image. The circular area on which the frequency analysis is carried out is slightly smaller than the circle

Figure B.4: Example of extended image.

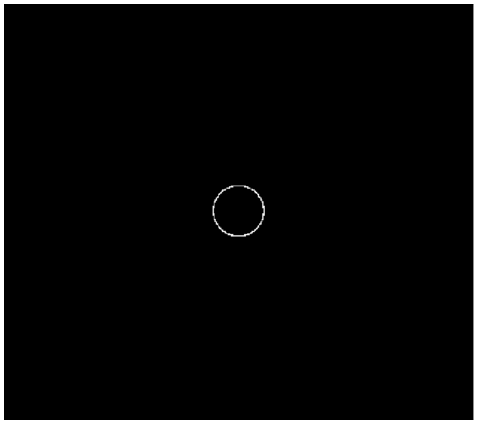

Figure B.5: Example of synthetic ring image.

Figure B.6: Example gradient image.

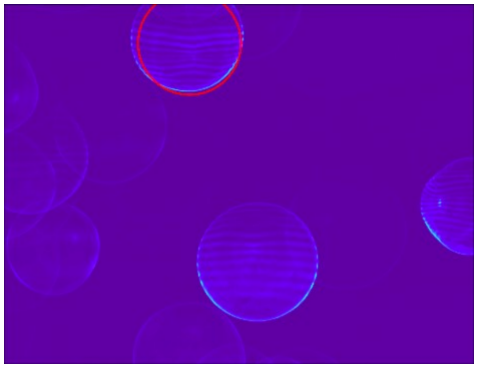

Figure B.7: Example of first detection image.

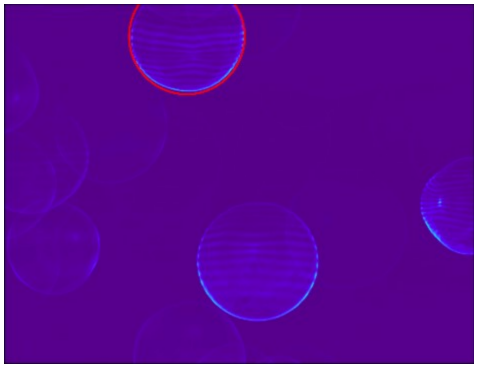

Figure B.8: Example of best detection image.

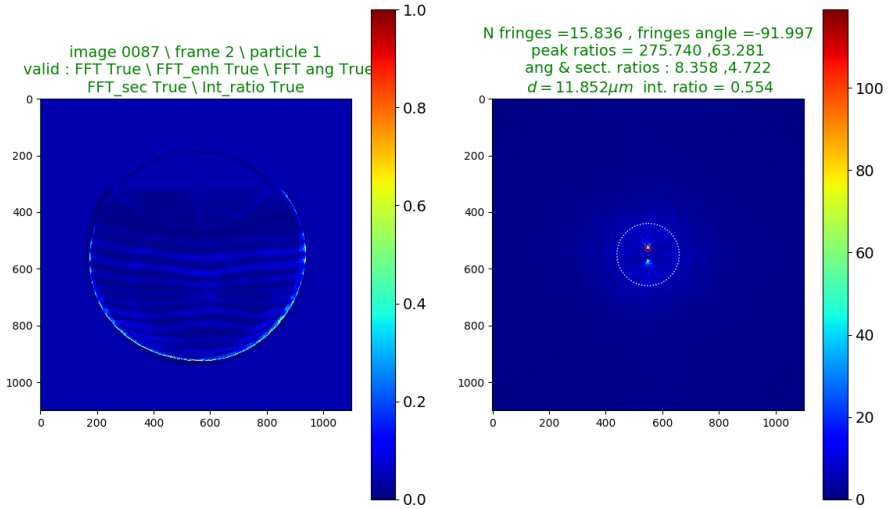

Figure B.9: Example of frequency analysis. (left panel) Cropped image used for frequency analysis. Only the circle corresponding to the detected droplet is not masked, while the rest of the cropped image is masked using the average pixel value within the image; note that the area on which the frequency analysis is done is actually slightly smaller than the circle corresponding to the detected droplet and it is indicated by the dashed back line. (right panel) Fourier transform of the image depicted in a. (FFT_image). Note that the frequency amplitude peak occurring at frequencies around zero is masked; the dashed withe line identifies the zone where the frequency amplitude is enhanced, as explained in the text. In right panel, the frequency amplitude peak related to the horizontal interference fringes visible in figure a. is evident; note that the FFT_image is centrally symmetric.

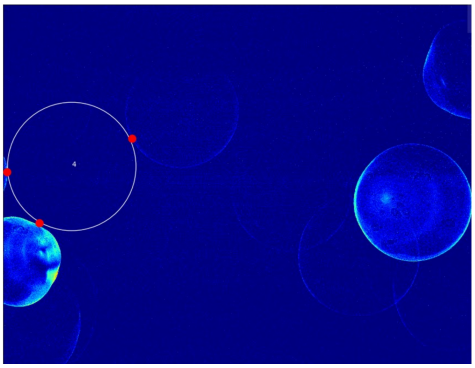

Figure B.10: Situation avoided by means of *crit*2. A false particle is detected (withe circle) due to 3 high intensity points (red dots).

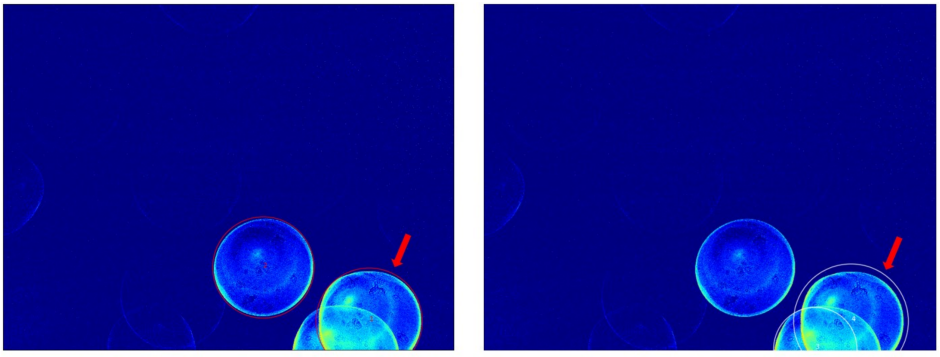

Figure B.11: Example of droplet detected in correspondence of previously detected particles. In a. the lower right particle detected is a real particle, while in b. the particle identified by the larger withe circle is false, it is detected due to the high correlation between the mask covering the previously detected droplet and the ring image.

corresponding to the particle to exclude the edge of the circle, which is slightly brighter than its inner part and that could interfere with the frequency analysis. An example of image on which the frequency analysis is performed is depicted in Figure B.9a.

The Fourier transform of the cropped and masked image is calculated (FFT_image). In the FFT_image the values of the pixel corresponds to the amplitudes, while the coordinates are related to the respective frequency. An enhanced form of the Fourier transform image is built (FFT_enh_image) by multiplying the amplitudes by their related frequency, so that higher frequency amplitudes are enhanced. The enhancement is stopped at a frequency of max_enh (= 0.1), otherwise high frequency noise would be too high. This is useful for two reasons. Firstly, the scattering pattern of large liquid particles is characterized by two frequencies, a lower and a higher one; the frequency of interest, which is related to droplet size, is the higher. Secondly, generally very low frequency amplitudes prevail, even if they are not of interest for our study – the interest is focused here on frequencies higher than the one corresponding to about two fringes within a circle. Furthermore, frequencies around zero are completely masked in both the FFT_image and FFT_enh_image. An example of FFT_image is depicted in Figure B.9b.

Then, the maximum amplitude of FFT_enh_image and its position is found. Then, the amplitude value of the FFT_image at the position (frequency) of the maximum of the FFT_enh_image is taken.

With the aim to exclude cases where the maximum of FFT_enh_image corresponds to noise, and not to a frequency characterizing a liquid droplet, two selection criteria are defined (Eq. B.3, B.4) :

$$FFT\_ratio = \frac{max(FFT\_image)}{avg(FFT\_image)} \tag{B.3}$$

$$FFT\_enh\_ratio = \frac{max(FFT\_enh\_image)}{avg(FFT\_enh\_image)} \tag{B.4}$$

These two criteria evaluate if the maximum is significant with respect to the mean value of FFT_image and FFT_enh_image; in fact, if the maximum is due to noise, it does not emerge significantly with respect to other values. Therefore, FFT_ratio and FFT_enh_ratio must be greater than FFT_crit and $FFT2\_min$, respectively. Only lately a maximum value of FFT_enh_ratio ($FFT2\_max$) has been imposed for the first measurement campaign.

A sub-pixel procedure is then used to locate with greater accuracy the FFT_image maximum value. The sub-pixel procedure consists in approximating the values of the 8 pixels around the maximum and the maximum itself with a Gaussian and, then, taking the position of the Gaussian maximum. With the new, more precise, position (fx, fy), the frequency is calculated ($freq = (fx^2 + fy^2)^{-1/2}$) and also the related angle ($fr\_angle = tan(fy/fx)$).

Three additional criteria are set in order to select the droplets, i.e. FFT_ang_ratio, FFT_sec_ratio and FFT_disk_ratio. The first criterion is used to exclude images showing a prevailing frequency, but not an unidirectional prevailing frequency. The second criterion is

useful to exclude images where there are more superposed frequency in one direction. The aim of the latter criterion – which has been only lately added for first campaign data treatment - is to exclude images with more superposed frequency which do not have a precise direction; the concept is similar to FFT_ratio and FFT_enh_ratio, but in this case the analysis is carried out only in a portion of the image defined by a disk with radius equal to freq. All these criteria must be greater than the relative limit value, FFT_ang_crit, FFT_sec_crit and FFT_disk_crit, respectively. The definition of the three criteria is the following (Eq. B.5, B.6 and B.7):

$$FFT\_ang\_ratio = \frac{max(FFT\_image)}{avg(FFT\_ring\_image)} \tag{B.5}$$

$$FFT\_sec\_ratio = \frac{max(FFT\_image)}{avg(FFT\_sec\_image)} \tag{B.6}$$

$$FFT\_disk\_ratio = \frac{max(FFT\_image)}{avg(FFT\_disk\_image)} \tag{B.7}$$

where FFT_ring_image, FFT_sec_image and FFT_disk_image are a portion of FFT_image, namely, a ring, a sector and a disk with radius equal to freq, respectively.

Note that the selection based on FFT_ratio, FFT_enh_ratio, FFT_ang_crit, FFT_sec_crit and FFT_disk_crit is not done yet at this point of the algorithm, but it will be done later.

Using the position of the FFT_image maximum, i.e. $freq$, just detected and the previously measured circle radius, the particle size is calculated, according to Eq. 2.2 in Chapter 2.

An additional criterion, int_ratio, is used which accounts for the intensity of light scattered by the detected particle. In fact, once the particle size is known, it is possible to calculate theoretically the scattered light intensity with the following relation (Eq. B.8):

$$I_{theor} = I_{laser}(x)\ d^2 \tag{B.8}$$

where $I_{laser}(x)$ is the laser light sheet intensity at a given x position within its thickness, while d is the particle size. Note that only the shape of the laser light intensity profile ($I_{laser,norm}$) is known from the taken measurements, as the relation between the intensity observed on the image ($I_{teor,imm}$), i.e. the pixel value, and the real intensity is unknown. However, the two quantities are proportional, so that it is possible to write (Eq. B.9):

$$I_{theor,imm} = c\ I_{laser,norm}(x)\ d^2 \tag{B.9}$$

The intensity measured in the image ($I_{meas,imm}$) for the detected particle should be, then, equal to the theoretical expected value $I_{teor,imm}$. $I_{meas,imm}$ is obtained by multiplying the average value within the circle corresponding to the droplet (calculated in the particle detection loop) and the circle area ($2\ \pi\ R^2$, where R is the best radius). Therefore, the following ratio

(int_ratio) should be almost constant ($min\_int\_ratio < int\_ratio < max\_int\_ratio$):

$$int\_ratio = \frac{I_{laser,norm}(x)\ d^2}{I_{meas,imm}} \tag{B.10}$$

At this point the detected particle is either validated as liquid droplet with its respective size or excluded as an error or as a solid droplet (particulate matter naturally present in the air) on the basis of FFT_ratio, FFT_enh_ratio, FFT_ang_ratio, FFT_sec_ratio, FFT_disk_ratio and int_ratio. Besides, also the fr_angle is evaluated as the frequency of the interference fringes characterizing liquid droplets is unidirectional. Therefore, fr_angle should be around the expected direction, with a tolerance of about $\pm 10°$. For campaign 1 the expected fringes direction is about 90°, while in campaign 2 the camera was rotated so that the expected angle is about $\pm 0°$. Some examples of not validated particles are shown in Figures B.12, B.13, B.14 and B.15.

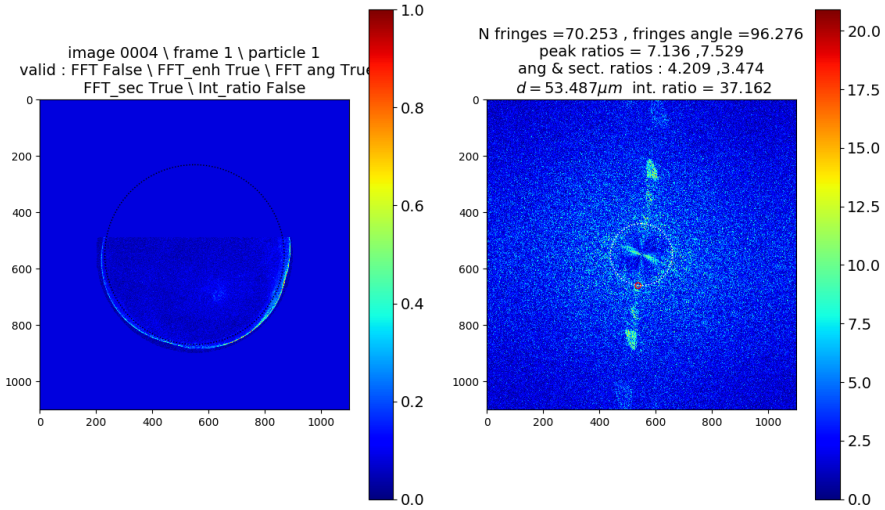

Figure B.12: Example of not validated particle; the value of FFT_ratio criterion exceeds the limit.

Only for the first measurement campaign (May 2021), an additional check is done on droplet for which all the criteria are respected except for int_ratio. In fact, in the first campaign a background frequency proper of the sensor of the camera used could interfere with the measurements. This background frequency is a high frequency in a defined range, which could be detected instead of the actual droplet frequency, giving very large droplet sizes. Therefore, if the detected maximum frequency fall in the background frequency range, then the FFT_image is masked in correspondence of the background frequency range and a new frequency analysis is performed. In the second campaign this problem is avoided by rotating the camera so that the background frequency has a direction almost perpendicular to the one of liquid droplets.

Finally, FFT_image is saved along with the particle list, updated with the new information.

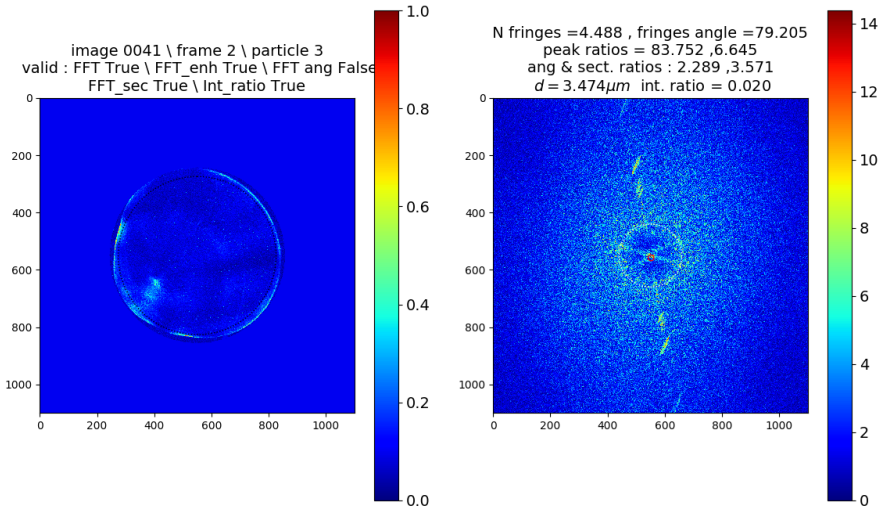

Figure B.13: Example of not validated particle; the value of FFT_ang_ratio criterion exceeds the limit.

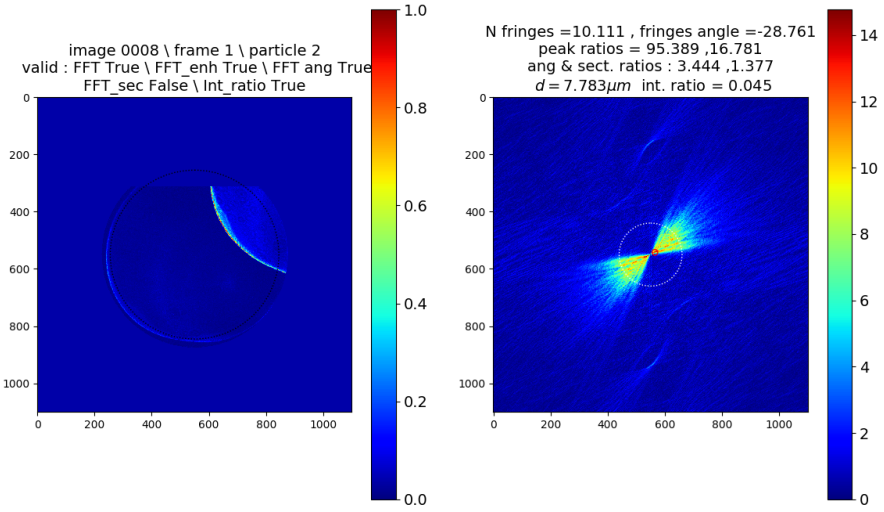

Figure B.14: Example of not validated particle; the value of FFT_sec_ratio criterion exceeds the limit.

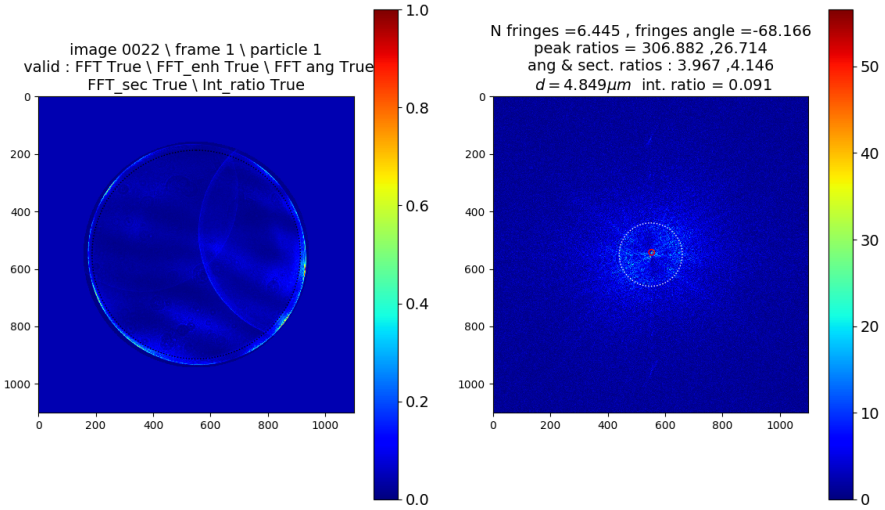

Figure B.15: Example of not validated particle; the value of fringes angle exceeds the limit.

Appendix C

Fits of speaking and coughing size distributions

Figures C.1 and C.2 depict the speaking and coughing size distributions fitted by means of a sum of two log-normal distributions (a. panels) and a Pareto distribution (b. panels). The former is more frequently used in the literature (see e.g. Johnson et al. (2011) and Morawska et al. (2009)), while the latter is suggested in the work by Balachandar et al. (2020).

The sum of log-normal distributions is useful as it gets the multi-modal nature of the droplet size distributions, which can be related to different droplet production mechanisms within the respiratory apparatus, as speculated by Johnson et al. (2011) and Morawska et al. (2009). In the present thesis two modes are identified. Therefore, the measured size distribution is split in two parts and each of them is interpolated and fitted with a log-normal distribution of the form Eq. C.1:

$$\frac{dC_n}{d\mathrm{d}} = \frac{c_1}{\mathrm{d}}\ e^{-\frac{(ln(\mathrm{d})-c_2)^2}{2c_3^2}} \tag{C.1}$$

The function resulting from the sum of the two log-normal distributions is the following Eq. C.2:

$$\frac{dC_n}{d\mathrm{d}} = \sum_i \left(\frac{c_{1i}}{\mathrm{d}}\ e^{-\frac{(ln(\mathrm{d})-c_{2i})^2}{2c_{3i}^2}} \right) \tag{C.2}$$

where c_{1i}, c_{2i} and c_{3i} are the parameters to be estimated, d is the droplet size and C_n is the droplet number concentration. Note that the parameters b_i and c_i are the expected value and the standard deviation of $ln(\mathrm{d})$. The sizes $\mathrm{d} = 10\ \mu m$ and $\mathrm{d} = 12\ \mu m$ are considered as cut-off for speaking and coughing, respectively.

Both for speaking and coughing the fit is quite good for sizes $\mathrm{d} < 4\ \mu m$ and for $\mathrm{d} > 10\ \mu m$, while it is weaker for $4\ \mu m < \mathrm{d} < 10\ \mu m$. Overall, the mean absolute relative difference between the experimental and the modelled data is ~ 26 % for coughing and ~ 35 % for speaking.

The Pareto distribution can not get the presence of several modes, but it is easier to use as

it is applied to the whole data set. It fits the coughing data reasonably well (absolute relative difference of ~ 43 %), but it seems to be less suited for speaking. The Pareto distribution has the form of Eq. C.3:

$$\frac{dC_n}{d\mathrm{d}} = \frac{c_1}{\mathrm{d}^{c_2}} \tag{C.3}$$

where $c1_i$ and $c2_i$ are the parameters to be estimated.

The parameters obtained by the fitting procedures are resumed in Tables C.1 and C.2.

Table C.1: Parameters of the two distributions (sum of log-normal and Pareto) obtained by the fitting procedure for speaking.

	log-normal d < 10 μm	log-normal d > 10 μm	Pareto
c_1	0.924	0.00410	2.11
c_2	0.187	3.25	0.570
c_3	0.361	0.629	-

Table C.2: Parameters of the two distributions (sum of log-normal and Pareto) obtained by the fitting procedure for coughing.

	log-normal d < 12 μm	log-normal d > 12 μm	Pareto
c_1	0.406	0.00229	2.95
c_2	0.301	2.91	0.0752
c_3	0.484	0.449	-

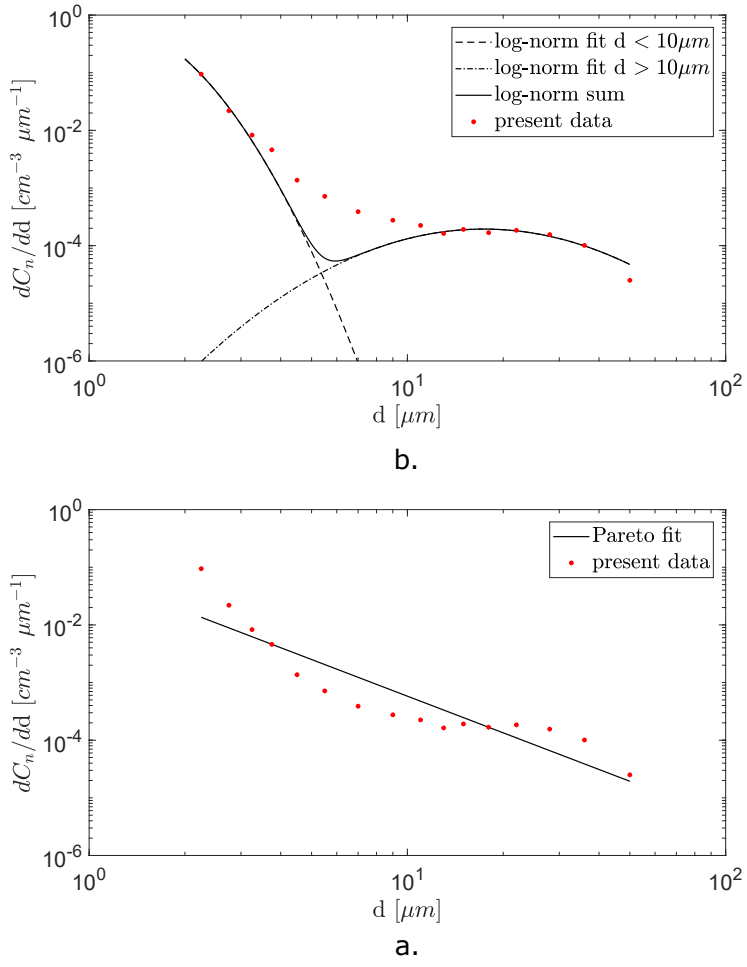

Figure C.1: Droplet size distribution measured for speaking activity fitted by means of a sum of log-normal distributions (a.) and a Pareto distribution (b.).

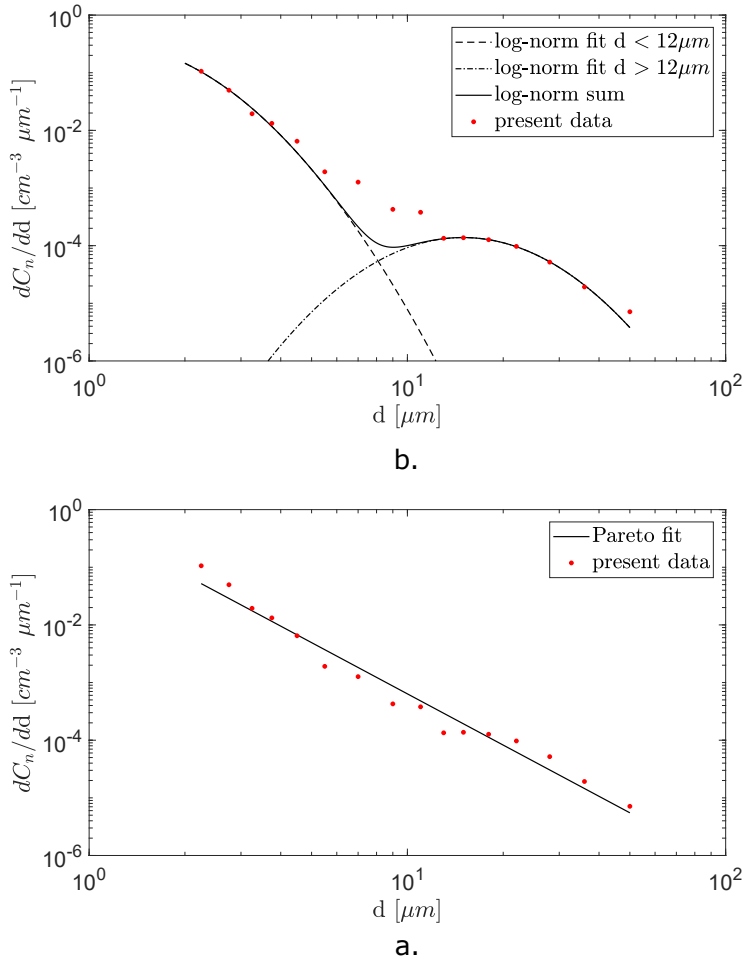

Figure C.2: Droplet size distribution measured for coughing activity fitted by means of a sum of log-normal distributions (a.) and a Pareto distribution (b.).

Bibliography

Ministero della salute. https://www.salute.gov.it/portale/nuovocoronavirus/ dettaglioFaqNuovoCoronavirus.jsp?lingua=italianoid=2573.

World health organization. https://www.who.int/news-room/questions-and-answers/item/coronavirus-diseasecovid-19-how-is-it-transmitted.

M Abkarian, S Mendez, N Xue, F Yang, and HA Stone. Speech can produce jet-like transport relevant to asymptomatic spreading of virus. *Proceedings of the National Academy of Sciences*, 117(41):25237–25245, 2020. doi: https://www.pnas.org/doi/abs/10.1073/pnas.2012156117.

AC Almstrand, B Bake, E Ljungström, P Larsson, A Bredberg, E Mirgorodskaya, and AC Olin. Effect of airway opening on production of exhaled particles. *Journal of Applied Physiology*, 108(3):584–588, 2010. doi: https://doi.org/10.1152/japplphysiol.00873.2009.

2013 ANSYS. *ANSYS Fluent theory guide - Release 15.0.* ANSYS, Canonsburg, PA, 2013.

S Asadi, AS Wexler, CD Cappa, S Barreda, NM Bouvier, and WD Ristenpart. Aerosol emission and superemission during human speech increase with voice loudness. *Scientific Reports*, 9(1):2348, 2019. doi: https://doi.org/10.1038/s41598-019-38808-z.

S Asadi, N Bouvier, AS Wexler, and WD Ristenpart. The coronavirus pandemic and aerosols: Does covid-19 transmit via expiratory particles? *Aerosol Science and Technology*, 54(6): 635–638, 2020. doi: https://doi.org/10.1080/02786826.2020.1749229.

P Bahl, CM de Silva, AA Chughtai, CR MacIntyre, and C Doolan. An experimental framework to capture the flow dynamics of droplets expelled by a sneeze. *Experiments in Fluids*, 61: 176, 2020. doi: https://doi.org/10.1007/s00348-020-03008-3.

P Bahl, CM de Silva, CR MacIntyre, S Bhattacharjee, AA Chughtai, and C Doolan. Flow dynamics of droplets expelled during sneezing. *Physics of Fluids*, 33(11):111901, 2021. doi: 10.1063/5.0067609.

S Balachandar, S Zaleski, A Soldati, G Ahmadi, and L Bourouiba. Host-to-host airborne transmission as a multiphase flow problem for science-based social distance guidelines. *International Journal of Multiphase Flow*, 132:103439, 2020. doi: https://www.sciencedirect.com/science/article/pii/S0301932220305498.

L Bourouiba. Turbulent Gas Clouds and Respiratory Pathogen Emissions: Potential Implications for Reducing Transmission of COVID-19. *JAMA*, 323(18):1837–1838, 05 2020. doi: https://doi.org/10.1001/jama.2020.4756.

L Bourouiba. The fluid dynamics of disease transmission. *Annual Review of Fluid Mechanics*, 53(1):473–508, 2021. doi: 10.1146/annurev-fluid-060220-113712.

L Bourouiba, E Dehandschoewercker, and JWM Bush. Violent expiratory events: on coughing and sneezing. *Journal of Fluid Mechanics*, 745:537–563, 2014. doi: 10.1017/jfm.2014.88.

M Brunel, H Shen, S Coëtmellec, G Gréhan, and T Delobel. Determination of the size of irregular particles using interferometric out-of-focus imaging. *International Journal of Optics*, 2014:1–8, 2014. doi: https://doi.org/10.1155/2014/143904.

FE Buckland and DAJ Tyrrell. Experiments on the spread of colds: 1. laboratory studies on the dispersal of nasal secretion. *Journal of Hygiene*, 62(3):365–377, 1964. doi: 10.1017/S0022172400040080.

G Buonanno, L Stabile, and L Morawska. Estimation of airborne viral emission: Quanta emission rate of sars-cov-2 for infection risk assessment. *Environment International*, 141:105794, 2020. doi: https://doi.org/10.1016/j.envint.2020.105794.

HB Burridge, S Fan, RL Jones, CJ Noakes, and PF Linden. Predictive and retrospective modelling of airborne infection risk using monitored carbon dioxide. *Indoor and Built Environment*, 31(5):1363–1380, 2022. doi: https://doi.org/10.1177/1420326X211043564.

G Busco, SR Yang, J Seo, and YA Hassan. Sneezing and asymptomatic virus transmission. *Physics of Fluids*, 32(7):073309, 2020. doi: https://doi.org/10.1063/5.0019090.

CYH Chao, MP Wan, L Morawska, GR Johnson, ZD Ristovski, M Hargreaves, K Mengersen, S Corbett, Y Li, X Xie, and D Katoshevski. Characterization of expiration air jets and droplet size distributions immediately at the mouth opening. *Journal of Aerosol Science*, 40(2):122–133, 2009. doi: https://doi.org/10.1016/j.jaerosci.2008.10.003.

S Chaudhuri, S Basu, P Kabi, VR Unni, and A Saha. Modeling the role of respiratory droplets in covid-19 type pandemics. *Physics of Fluids*, 32(6):063309, 2020. doi: 10.1063/5.0015984.

SA Chillón, U Fernandez-Gamiz, E Zulueta, A Ugarte-Anero, and O Urbina-Garcia. Numerical modeling of a sneeze, a cough and a continuum speech inside a hospital lift. *Environmental Health Insights*, 9(2):e13370, 2023. doi: https://doi.org/10.1016/j.heliyon.2023.e13370.

T Dbouk and D Drikakis. On coughing and airborne droplet transmission to humans. *Physics of Fluids*, 32(5):053310, 2020a. doi: 10.1063/5.0011960.

T Dbouk and D Drikakis. Weather impact on airborne coronavirus survival. *Physics of Fluids*, 32(9):093312, 2020b. doi: 10.1063/5.0024272.

D De Padova and M Mossa. Multi-phase simulation of infected respiratory cloud transmission in air. *AIP Advances*, 11(3):035035, 2021. doi: 10.1063/5.0047692.

CM de Silva, P Bahl, C Doolan, and CR MacIntyre. Bespoke flow experiments to capture the dynamics of coughs and sneezes. *Measurement Science and Technology*, 32(12):125302, 2021. doi: 10.1088/1361-6501/ac2010.

S Dehaeck and J van Beeck. Multifrequency interferometric particle imaging for gas bubble sizing. *Experiments in Fluids*, 45:823–831, 2008. doi: https://doi.org/10.1007/s00348-008-0502-8.

JP Duguid. The size and the duration of air-carriage of respiratory droplets and droplet-nuclei. *Journal of Hygene*, 44(6):471–479, 1946. doi: https://doi.org/10.1017/s0022172400019288.

D Edwards, J Man, P Brand, J Katstra, K Sommerer, H Stone, E Nardell, and G Scheuch. Inhaling to mitigate exhaled bioaersols. *Proceedings of the National Academy of Sciences of the United States of America*, 101:17383–8, 2005. doi: 10.1073/pnas.0408159101.

P Fabian, J Mcdevitt, W DeHaan, R Fung, B Cowling, KH Chan, G Leung, and D Milton. Influenza virus in human exhaled breath: An observational study. *PloS one*, 3:e2691, 2008. doi: 10.1371/journal.pone.0002691.

M Fang, A Lau, C Chan, CT Hung, and TW Lee. Aerodynamic properties of biohazardous aerosols in hospitals. 14:26–28, 02 2008.

PJ Gerone, RB Couch, GV Keefer, G Douglas, EB Derrenbacher, and V Knight. Assessment of experimental and natural viral aerosols. *Bacteriological Reviews*, 30(3):576–588, 1966. doi: https://journals.asm.org/doi/abs/10.1128/br.30.3.576-588.1966.

AR Glover, SM Skippon, and RD Boyle. Interferometric laser imaging for droplet sizing: a method for droplet-size measurement in sparse spray systems. *Applied Optics*, 34(36):8409–8421, 1995. doi: 10.1364/AO.34.008409.

J Gralton, E Tovey, M L McLaws, and W D Rawlinson. The role of particle size in aerosolised pathogen transmission: a review. *Journal of infection*, 62(1):1–13, 2011. doi: https://doi.org/10.1016/j.jinf.2010.11.010.

L Grandoni, A Pini, A Pelliccioni, L Méès, Leuzzi G, and P Monti. Numerical dispersion modelling of the droplets expired by humans., 2022. 21st International Conference on Harmonisation within Atmospheric Dispersion Modelling for Regulatory Purposes, HARMO 2022.

L Grandoni, L Méès, N Grosjean, G Leuzzi, P Monti, A Pelliccioni, and P Salizzoni. Interferometric laser imaging for respiratory droplets sizing. *Experiments in Fluids*, 64(80), 2023. doi: https://doi.org/10.1007/s00348-023-03610-1.

J K Gupta, C.-H Lin, and Q Chen. Flow dynamics and characterization of a cough. *Indoor Air*, 19(6):517–25, 2009. doi: 10.1111/j.1600-0668.2009.00619.x.

Jitendra K Gupta, Chao-Hsin Lin, and Qingyan Chen. Characterizing exhaled airflow from breathing and talking. *Indoor Air*, 20(1):31–39, 2010. doi: 10.1111/j.1600-0668.2009.00623.x.

ZY Han, WG Weng, and QY Huang. Characterizations of particle size distribution of the droplets exhaled by sneeze. *Journal of the Royal Society Interface*, 10:20130560.20130560, 2013. doi: http://doi.org/10.1098/rsif.2013.0560.

K Haslbeck, K Schwarz, JM Hohlfeld, JR Seume, and W Koch. Submicron droplet formation in the human lung. *Journal of Aerosol Science*, 41(5):429–438, 2010. ISSN 0021-8502. doi: https://doi.org/10.1016/j.jaerosci.2010.02.010.

G Hersen, S Moularat, E Robine, E Géhin, S Corbet, A Vabret, and F Freymuth. Impact of health on particle size of exhaled respiratory aerosols: Case-control study. *Clean Soil Air Water*, 36(7):572–577, 2008. doi: https://doi.org/10.1002/clen.200700189.

WC Hinds. *Aerosol Technology: Properties, Behavior, and Measurement of Airborne Particles, 2nd Edition*. J. Wiley sons, New York, 1999.

H Holmgren, E Ljungström, AC Almstrand, B Bake, and AC Olin. Size distribution of exhaled particles in the range from 0.01 to 2.0 μm. *Journal of Aerosol Science*, 41(5):439–446, 2010. doi: 10.1016/j.jaerosci.2010.02.011.

GR Hunt and NB Kaye. Pollutant flushing with natural displacement ventilation. *Building and Environment*, 41(9):1190–1197, 2006. doi: https://www.sciencedirect.com/science/article/pii/S0360132305001587.

GR Johnson, L Morawska, RD Ristovski, M Hargreaves, K Mengersen, CYH Chao, MP Wan, Y Li, X Xie, D Katoshevski, and S Corbett. Modality of human expired aerosol size distributions. *Journal of Aerosol Science*, 42(12):839–851, 2011. doi: https://doi.org/10.1016/j.jaerosci.2011.07.009.

T Kawaguchi, Y Akasaka, and M Maeda. Size measurements of droplets and bubbles by advanced interferometric laser imaging technique. *Meas Sci Technol*, 13:308, 2002. doi: 10.1088/0957-0233/13/3/312.

SB Kwon, J Park, J Jang, Y Cho, DS Park, C Kim, GN Bae, and A Jang. Study on the initial velocity distribution of exhaled air from coughing and speaking. *Chemosphere*, 87(11):1260–1264, 2012. doi: https://doi.org/10.1016/j.chemosphere.2012.01.032.

D Lewis. Is the coronavirus airborne? experts can't agree. *Nature*, 580:175, 2020. doi: doi:https://doi.org/10.1038/d41586-020-00974-w.

M Li, KL Chong, CS Ng, P Bahl, CM de Silva, R Verzicco, C Doolan, CR MacIntyre, and D Lohse. Towards realistic simulations of human cough: Effect of droplet emission duration and spread angle. *Interantional Journal of Multiphase Flow*, 147:103883, 2022. doi: https://doi.org/10.1016/j.ijmultiphaseflow.2021.103883.

Y Li, H Qian, J Hang, X Chen, P Cheng, H Ling, S Wang, P Liang, J Li, S Xiao, J Wei, L Liu, BJ Cowling, and M Kang. Probable airborne transmission of sars-cov-2 in a poorly ventilated restaurant. *Building and Environment*, 196:107788, 2021. ISSN 0360-1323. doi: https://doi.org/10.1016/j.buildenv.2021.107788.

F Liu, H Qian, Z Luo, S Wang, and X Zheng. A laboratory study of the expiratory airflow and particle dispersion in the stratified indoor environment. *Building and Environment*, 180:106988, 2020. doi: https://doi.org/10.1016/j.buildenv.2020.106988.

L Liu, J Wei, Y Li, and A Ooi. Evaporation and dispersion of respiratory droplets from coughing. *Indoor air*, 27(1):179–190, 2017. doi: https://doi.org/10.1111/ina.12297.

RG Loudon and RM Roberts. Droplet expulsion from the respiratory tract. *American Review of Respiratory Disease*, 95(3):435–42, 1967.

M Maeda, T Kawaguchi, and K Hishida. Interferometric laser imaging for droplet sizing: a method for droplet-size measurement in sparse spray systems. *Meas Sci Technol*, 11: L13–L18, 2000. doi: https://doi.org/10.1088/0957-0233/11/12/101.

RP Mahajan, P Singh, GE Murty, and AR Aitkenhead. Relationship between expired lung volume, peak flow rate and peak velocity time during a voluntary cough manoeuvre. *British Journal of Anaesthesia*, 72(3):298–301, 1994. doi: https://doi.org/10.1093/bja/72.3.298.

L Mees, D Lebrun, D Fréchou, and R Boucheron. Interferometric laser imaging technique applied to nuclei size measurements in cavitation tunnel, 2011. Paper presented at the 2nd International Conference on Advanced Model Measurement Technology for EU Maritime Industry (AMT'11), Apr 2011, Newcastel upon Tyne, United Kingdom.

R Mittal, R Ni, and JH Seo. The flow physics of covid-19. *Journal of Fluid Mechanics*, 894: F2, 2020. doi: 10.1017/jfm.2020.330.

L Morawska and J Cao. Airborne transmission of sars-cov-2: The world should face the reality. *Environment International*, 139:105730, 2020. doi: https://doi.org/10.1016/j.envint.2020.105730.

L Morawska, GR Johnson, ZD Ristovski, M Hargreaves, K Mengersen, S Corbett, CYH Chao, Y Li, and D Katoshevski. Size distribution and sites of origin of droplets expelled from the human respiratory tract during expiratory activities. *Journal of Aerosol Science*, 40(3): 256–269, 2009. doi: https://doi.org/10.1016/j.jaerosci.2008.11.002.

SR Nishandar, Y He, M Princevac, and RD Edwards. Fate of Exhaled Droplets From Breathing and Coughing in Supermarket Checkouts and Passenger Cars. *Environmental Health Insights*, 17(1), 2023. doi: https://doi.org/10.1177/11786302221148274.

H Nishimura, S Sakata, and A Kaga. A new methodology for studying dynamics of aerosol particles in sneeze and cough using a digital high-vision, high-speed video system and vector analyses. *PLoS One*, 8(11):e80244, 2013. doi: https://doi.org/10.1371/journal.pone.0080244.

M Pan, JA Lednicky, and CY Wu. Collection, particle sizing and detection of airborne viruses. *Journal of applied microbiology*, 127(6):1596–1611, 2019. doi: https://doi.org/10.1111/jam.14278.

Y Pan, D Zhang, P Yang, L Poon, and Q Wang. Viral load of sars-cov-2 in clinical samples. *Lancet Infect Dis*, 20:1473–3099, 2020. doi: https://doi.org/10.1016/S1473-3099(20)30113-4.

R Papineni and FS Rosenthal. The size distribution of droplets in the exhaled breath of healthy human subjects. *J Aerosol Med*, 10(2):105–16, 1997. doi: https://doi.org/10.1089/jam.1997.10.105.

A Pelliccioni, P Monti, G Cattani, F Boccuni, M Cacciani, S Canepari, P Capone, M Catrambone, M Cusano, MC D'Ovidio, A De Santis, A Di Bernardino, A Di Menno di Bucchianico, S Di Renzi, R Ferrante, A Gaeta, R Gaddi, M Gherardi, M Giusto, A Gordiani, L Grandoni, G Leone, G Leuzzi, N L'Episcopo, F Marcovecchio, A Pini, T Sargolini, F Tombolini, L Tofful, and C Perrino. Integrated evaluation of indoor particulate exposure: The viepi project. *Sustainability*, 12(22), 2020.

E Porcheron, P Lemaitre, J Van Beeck, R Vetrano, M Brunel, G Grehan, and L Guiraud. Development of a spectrometer for airborne measurement of droplet sizes in clouds. *Journal of European Optical Society Rapid publ,*, 10(0), 2015. doi: http://dx.doi.org/10.2971/jeos.2015.15030.

H Qian, L Miao, Tand Liu, X Zheng, D Luo, and Y Li. Indoor transmission of sars-cov-2. *Indoor Air*, 31(3):639–645, 2021. doi: 10.1111/ina.12766.Epub2020Nov20.PMID:33131151.

R Ragucci, A Cavaliere, and P Massoli. Drop sizing by laser light scattring exploiting intensity angular oscillation in the mie regime. *Particle Particle Systems Characterization*, 7(1-4):221–225, 1990. doi: https://doi.org/10.1002/ppsc.19900070136.

E Renzi and A Clarke. Life of a droplet: Buoyant vortex dynamics drives the fate of microparticle expiratory ejecta. *Physics of Fluids*, 32(12):123301, 2020. doi: https://doi.org/10.1063/5.0032591.

H Rezaee and A Kebriaee. Droplet sizing of electrospray based on interferometric laser imaging, 2019. Paper presented at ILASS–Europe 2019, 29th Conference on Liquid Atomization and Spray Systems, 2-4 September 2019, Paris, France.

ME Rosti, S Olivieri, M Cavaiola, A Seminara, and A Mazzino. Fluid dynamics of covid-19 airborne infection suggests urgent data for a scientific design of social distancing. *Scientific Reports*, 10:22426, 2020. doi: 10.1038/s41598-020-80078-7.

ME Rosti, M Cavaiola, S Olivieri, A Seminara, and A Mazzino. Turbulence role in the fate of virus-containing droplets in violent expiratory events. *Physical Review Research*, 3:013091, 2021. doi: https://link.aps.org/doi/10.1103/PhysRevResearch.3.013091.

S Sahu, Y Hardalupas, and AMKP Taylor. Droplet–turbulence interaction in a confined polydispersed spray: effect of turbulence on droplet dispersion. *Journal of Fluid Mechanics*, 794:267–309, 2016. doi: 10.1017/jfm.2016.169.

B E Scharfman, A H Techet, J W M Bush, and L Bourouiba. Visualization of sneeze ejecta: steps of fluid fragmentation leading to respiratory droplets. *Experiments in Fluids*, 57:24, 2016. doi: https://doi.org/10.1007/s00348-015-2078-4.

G Seminara, B Carli, G Forni, S Fuzzi, A Mazzino, and A Rinaldo. Biological fluid dynamics of airborne covid-19 infection. *Rend Fis Acc Lincei*, 31(3):505–537, 2020. doi: https://doi.org/10.1007/s12210-020-00938-2.

P Singh, R P Mahajan, G E Murty, and A R Aitkenhead. Relationship of peak flow rate and peak velocity time during voluntary coughing. *British Journal of Anaesthesia*, 74(6): 714–716, 1995. doi: https://doi.org/10.1093/bja/74.6.714.

R Singhal, S Ravichandran, R Govindarajan, and SS Diwan. Virus transmission by aerosol transport during short conversations. *Flow*, 2:E13, 2022. doi: https://doi.org/10.1017/flo.2022.7.

J W Tang, A D Nicolle, C A Klettner, J Pantelic, L Wang, A B Suhaimi, A Y L Tan, G W X Ong, R Su, C Sekhar, D D W Cheong, and K W Tham. Airflow dynamics of human jets: Sneezing and breathing - potential sources of infectious aerosols. *PLoS ONE*, 8(4):e59970, 2013. doi: https://doi.org/10.1371/journal.pone.0059970.

M VanSciver, S Miller, and J Hertzberg. Particle image velocimetry of human cough. *Aerosol Science and Technology*, 45(3):415–422, 2011. doi: https://doi.org/10.1080/02786826.2010.542785.

B Wang, H Wu, and XF Wan. Transport and fate of human expiratory droplets-a modeling approach. *Physics of Fluids*, 32(8):083307, 2020a. doi: https://doi.org/10.1063/5.0021280.

H Wang, Z Li, X Zhang, L Zhu, Y Liu, and S Wang. The motion of respiratory droplets produced by coughing. *Physics of Fluids*, 32(12):125102, 2020b. doi: 10.1063/5.0033849.

J Wang, M Alipour, G Soligo, A Roccon, M De Paoli, F Picano, and A Soldati. Short-range exposure to airborne virus transmission and current guidelines. *Proceedings of the National Academy of Sciences of the United States of America*, 118(37):e2105279118, 2021. doi: https://doi.org/10.1073/pnas.2105279118.

J Wang, F Dalla Barba, A Roccon, G Sardina, A Soldati, and F Picano. Modelling the direct virus exposure risk associated with respiratory events. *Journal of The Royal Society Interface*, 19(186):20210819, 2022. doi: https://royalsocietypublishing.org/doi/abs/10.1098/rsif.2021.0819.

J Wei and Y Li. Enhanced spread of expiratory droplets by turbulence in a cough jet. *Building and Environment*, 93:86–96, 2015. doi: https://doi.org/10.1016/j.buildenv.2015.06.018.

J Wei and Y Li. Human cough as a two-stage jet and its role in particle transport. *PLoS One*, 12(1):e0169235, 2017. doi: 10.1371/journal.pone.0169235.

W F Wells. ON AIR-BORNE INFECTION*: STUDY II. DROPLETS AND DROPLET NUCLEI. *American Journal of Epidemiology*, 20(3):611–618, 11 1934. doi: https://doi.org/10.1093/oxfordjournals.aje.a118097.

X Xie, Y Li, AT Chwang, PL Ho, and WH Seto. How far droplets can move in indoor environments–revisiting the wells evaporation-falling curve. *Indoor Air*, 17(3):211–225, 2007. doi: https://doi.org/10.1111/j.1600-0668.2007.00469.x.

X Xie, Y Li, H Sun, and L Liu. Exhaled droplets due to talking and coughing. *Journal of The Royal Society Interface*, 6(suppl_6):S703–S714, 2009. doi: https://royalsocietypublishing.org/doi/abs/10.1098/rsif.2009.0388.focus.

F Yang, AA Pahlavan, S Mendez, M Abkarian, and HA Stone. Towards improved social distancing guidelines: Space and time dependence of virus transmission from speech-driven aerosol transport between two individuals. *Physical Review Fluids*, 5:122501, 2020. doi: 10.1103/PhysRevFluids.5.122501.

S Yang, GWM. Lee, CM Chen, CC Wu, and KP Yu. The size and concentration of droplets generated by coughing in human subjects. *Journal of Aerosol Medicine*, 20(4):484–494, 2007. doi: https://doi.org/10.1089/jam.2007.0610.

E Yilmaz, T Suzuki, K Ito, G J Gotama, W Anggono, and M Ichiyanagi. Analysis of the spray characteristics of water and water/glycerin mixtures using an interferometric laser imaging for droplet sizing technique. *International Journal of Technology*, 12(1):101–112, 2021. doi: https://doi.org/10.14716/ijtech.v12i1.4188.

G Zayas, MCJ Chiang, EYL Wong, F MacDonald, CF Lange, A Senthilselvan, and M King. Cough aerosol in healthy participants: fundamental knowledge to optimize droplet-spread infectious respiratory disease management. *BMC Pulmonary Medicine*, 12:11 – 11, 2012.

S Zhu, S Kato, and JH Yang. Study on transport characteristics of saliva droplets produced by coughing in a calm indoor environment. *Building and Environment*, 41(12):1691–1702, 2006. doi: https://doi.org/10.1016/j.buildenv.2005.06.024.

Acknowledgements

I thank professors Paolo Monti and Pietro Salizzoni for giving me the opportunity to do the PhD in co-supervision between Italy and France, for following my work and for helping me when needed. I thank the Istituto Nazionale per l'Assicuraione contro gli Infortuni sul Lavoro (INAIL) and the Bourse Eiffel program for funding my PhD. In particular, I thank Armando Pelliccioni for his supervision and for the enthusiasm he puts in his work. I especially thank Loïc Méès, with whom I have worked almost every day for a year and without whose help I would not have been able to carry out the work. I thank Nathalie Grosjean, who helped me with the experimental tools, and Laurent Pouilloux, the technical manager of the computing centre of the École Centrale de Lyon. I thank Agnese Pini for her help with the numerical simulations and as a colleague and a friend.

I really thank all the brave volunteers who participated to the experiments.

I thank all the colleagues, who became friends, from the Sapienza University of Rome and from the École Centrale de Lyon. I'm happy to have shared with you (a lot of) time, anxieties and enthusiasm in the last three years.

I thank my family, Bianca, Enrico and Edoardo, for always trusting and encouraging me, especially when I don't do it on my own. I promised that the Master's (and the related stress) would have been the last thesis, but I didn't respect the promise. This is the last one, I swear!

I thank all the more and less old friends who keep on being close to me despite the physical distances (different countries, lock-downs, breakups, a thousand commitments...). I especially thank Cristiano, Gabriele, Natalia, Silvia, Stefania and Valeria.

I also thank the friends from dance classes, with whom I always have a carefree fun.

Lastly, I thank Stefano, for his calm and sincere support. I repeat the concept also for you: that's the last thesis, I swear!

I am glad I had the chance to do the rather difficult but very exciting experience of the PhD.

Livia Grandoni, Rome, April 2023